

Plasmonic Metasurfaces for Enhanced Third Harmonic
Generation

by

Mohammadreza Sanadgol Nezami

B. Sc. in Electrical Engineering, University of Sistan and Baluchestan, 2000

M. Sc. in Electrical Engineering, Iran University of Science and Technology, 2006

A Dissertation Submitted in Partial Fulfillment
of the Requirements for the Degree of

DOCTOR OF PHILOSOPHY

in the Department of Electrical and Computer Engineering

© Mohammadreza Sanadgol Nezami, 2016
University of Victoria

All rights reserved. This report may not be reproduced in whole or in part, by photocopy
or other means, without the permission of the author.

Supervisory Committee

Plasmonic Metasurfaces for Enhanced Third Harmonic Generation

by

Mohammadreza Sanadgol Nezami

Supervisory Committee

Dr. Reuven Gordon, (Department of Electrical and Computer Engineering)

Supervisor

Dr. Harry Kwok, (Department of Electrical and Computer Engineering)

Departmental Member

Dr. Byoung-Chul Choi, (Department of Physics and Astronomy)

Outside Member

Abstract

Supervisory Committee

Dr. Reuven Gordon, (Department of Electrical and Computer Engineering)

Supervisor

Dr. Harry Kwok, (Department of Electrical and Computer Engineering)

Departmental Member

Dr. Byoung-Chul Choi, (Department of Physics and Astronomy)

Outside Member

This research was mainly focused on the design and optimization of aperture-based structures to achieve the greatest third harmonic conversion efficiency. It was discovered that by tuning the localized surface plasmon resonance to the fundamental beam wavelength, and by tuning the propagating surface plasmons resonance to the Bragg resonance of the aperture arrays, both the directivity and conversion efficiency of the third harmonic signal were enhanced. The influence of the gap plasmon resonance on the third harmonic conversion efficiency of the aperture arrays was also investigated. The resulted third harmonic generation (THG) from an array of annular ring apertures as a closed loop structure were compared to arrays of H-shaped, double nanohole and rectangular apertures as open-loop structures. The H-shaped structure had the greatest conversion efficiency at approximately 0.5 %. Moreover, it was discovered that the maximum THG did not result from the smallest gap; instead, the gap sizes where the scattering and absorption cross sections were equal, led to the greatest THG. The finite difference time domain (FDTD) simulations based on the nonlinear scattering theory were also performed. The simulation results were in good agreement with the experimental data. Moreover, a modified quantum-corrected model was developed to

study the electron tunneling effect as a limiting factor of the THG from plasmonic structures in the sub-nanometer regime.

Table of Contents

Supervisory Committee	ii
Abstract	iii
Table of Contents	v
List of Tables.....	vii
List of Figures	viii
Acknowledgment.....	xiv
Dedication	xv
Glossary	xvi
Chapter 1 : Introduction.....	1
1.1 Motivation	1
1.2 Research Objectives.....	1
1.2.1 The Influence of Localized and Propagating Surface Plasmon Resonance on THG of Nanostructures	1
1.2.2 The Effect of Quantum Electron Tunneling on THG	2
1.2.3 Gap Plasmons Effect on THG Efficiency of Nanostructures	2
1.3 Overview of Thesis	3
Chapter 2 : Background and Previous Works.....	4
2.1 Third Harmonic Generation	5
2.2 Plasmonics.....	6
2.2.1 Surface Plasmon Polaritons	6
2.2.2 Localized Surface Plasmons	9
2.3 Extraordinary Optical Transmission	19
2.4 Quantum Corrected Model.....	21
2.4.1 Quantum Electron Tunneling Through a Finite Rectangular Potential Barrier [54].....	21
2.4.2 Characterization of Computational Models on the Onset of Electron Tunneling	24
2.5 Nonlinear Scattering Theory	29
2.6 Summary	29
Chapter 3 : Experimental Methods.....	31
3.1 Introduction	31
3.2 Fabrication Methods	31
3.2.1 Focused Ion Beam Milling	31
3.2.2 Electron Beam Lithography.....	32
3.2.3 Fabrication of Nanogaps by Atomic Layer Deposition and Lithography	34
3.2.4 Template Stripping	35
3.3 Characterization Methods	38
3.3.1 Scanning Electron Microscopy	38
3.3.2 Specifications of the Hitachi S-4800 FESEM [60].....	41
3.4 Summary	42
Chapter 4 : Experiments on Nonlinear Optics	43
4.1 Introduction	43

4.2 Experimental Setups in Reflection Geometry	43
4.3 Experimental Setups in Transmission Geometry	46
4.4 Summary	49
Chapter 5 : Theoretical Models in Nonlinear Optics.....	50
5.1 Introduction	50
5.2 Harmonic Oscillator Model.....	50
5.3 Nonlinear Scattering Theory	52
5.4 Investigating the Effect of Localized Surface Plasmons (LSPs) and Propagating Surface Plasmon Polaritons (SPPs) on THG of the Aperture Arrays.....	57
5.4.1 Fabrication and THG Measurement.....	58
5.4.2 Discussion.....	62
5.2 Summary	64
Chapter 6 : Quantum Corrected Model and THG	66
6.1 Introduction	66
6.2 THG on the Onset of Electron Tunneling	66
6.3 Summary	71
Chapter 7 : Gap Plasmon Enhanced THG In Aperture-based Metasurfaces	72
7.1 Introduction	72
7.2 Film-coupled Nanosphere Structure [98].....	72
7.3 THG in Bowtie Nanoantenna Structure [64].....	74
7.3 Radiation Engineering for Maximum Field Enhancement [99]	77
7.4 Effect of Matched Scattering and Absorption Rate on THG From a Single Slit ...	80
7.5 Effect of Gap Plasmons on Aperture-based THG	81
7.5.1 Nonlinear Measurements and Discussion	83
7.5.2 Methods	86
7.5.2.1 FDTD Simulation.....	86
7.5.2.2 Fabrication Methods.....	87
7.6. Summary	87
Chapter 8 : Conclusion and Future Work	88
8.1 Introduction	88
8.2 Metasurfaces for Nonlinear Wave Front Phase Control	89
8.3 TH Focusing Lens.....	93
8.4 TH Wave Plates	94
Appendix A: Focused Ion Beam Milling Parameters.....	96
Appendix B: Lumerical FDTD Simulation Parameters.....	97
Appendix C: Template Stripping For Sub-10 nm Gap Aperture Arrays.....	98
C.1 Silicon Templates SEM Characterization.....	98
C.1.1 Normal images	98
C.1.2 Tilted Images for Depth Estimation	100
C.2 Template Stripped Structure SEM Images	101
Appendix D: THG Enhancement by Nano-apertures.....	104
D.1 Introduction	104
D.2 The Single Aperture THG	105
Publications and Contributions:	108
References.....	109

List of Tables

Table 3.1 Specification of the Hitachi FB2100 FIB [60]	32
Table 3.2 The influence of different parameters on EBL process. Reprinted with permission from Ref. [56].....	34
Table 6.1 Calculated plasma frequencies and resulted integrated values inside the gap for five different SAM layer spacers.....	68
Table 7.1 Comparison of the experimental and simulation results for different aperture array structures	86
Table A-1 Milling Parameters for Fabrication of Single Apertures.....	96
Table A-2 Milling Parameters for Fabrication of Aperture Arrays.....	96
Table B-1 FDTD simulation parameters for a 60 nm nanosphere on the gold surface.....	97
Table B-2 FDTD simulation parameters for aperture arrays	97

List of Figures

Figure 2.1 a) the third harmonic generation process b) photon description of the THG. Reprinted with permission from Ref. [43].	6
Figure 2.2 Prism coupling using attenuated total internal reflection in a) Otto configuration b) Kretschmann configuration	7
Figure 2.3 Surface plasmon polaritons a) propagating waves bounded to the metal-dielectric interface b) Evanescent waves into the metal and dielectric material perpendicular to the interface c) Typical dispersion curve. Reprinted with permission from Ref. [47].	8
Figure 2.4 Propagation length of the SPPs for Aluminum and Silver. Reprinted with permission from Ref. [47].	9
Figure 2.5 a) Localized surface plasmons b) comparison of the typical dispersion curve of LSPs with SPPs. Reprinted with permission from Ref. [48].	10
Figure 2.6 A homogeneous metal sphere exposed to electric field E_0 . Reprinted with permission from Ref. [49].	10
Figure 2.7 Schematic of the rectangular waveguide: The effective dielectric constant of the lowest TE mode is derived by considering the TM mode of the slab. Reprinted with permission from Ref. [50].	12
Figure 2.8 Geometry of a three-layer system. Reprinted with permission from Ref. [49]	13
Figure 2.9 The attenuation resulted from material losses and the cut-off attenuation for a rectangular aperture of 105 nm by 270 nm. Reprinted with permission from Ref. [50].	17
Figure 2.10 The spatial electric field distribution in a rectangular aperture in the gold film: The electric field component of the incident field is perpendicular to the longer side. Reprinted with permission from Ref. [51].	18
Figure 2.11 The schematic diagram of the phase-matching of light to SPPs by using a grating. Reprinted with permission from [49].	20
Figure 2.12 Illustration of a finite rectangular potential barrier.	21
Figure 2.13 Transmission coefficient as a function of energy. Reprinted with permission from Ref. [54].	24
Figure 2.14 The description of the nanoparticle dimer behavior using different theoretical treatments: a) CEM: The conductivity between the nanoparticles is zero, and therefore the electron tunneling probability is zero, and no electron can transfer between the particles ($T=0$). b) QM: The electron tunneling probability is greater than zero ($T>0$) and the electron density distribution of the electrons, Ψ^2 , cannot be changed abruptly. c) QCM: The material in the junction is modeled by a virtual dielectric medium that is represented by $\epsilon(l(x,y), \omega)$. Reprinted with permission from Ref. [90].	25
Figure 2.15 Illustration of the parameters involved in the QCM: a) a simple flat plasmonic configuration b) The inhomogeneous local dielectric constant distribution in the QCM of the metallic dimer. c) Normalized electron tunneling transmission d) Electron collision frequency in the gap region as a function of the gap size. The blue curves show the results for gold jellium and the red curves are related to Na jellium. Reprinted with permission from Ref. [90].	27

Figure 2.16 Simulation results of near-field energy for large plasmonic dimers for different separations using CEM (a, b) and QCM(c, d). Reprinted with permission from Ref. [90].....	28
Figure 2.17 Simulation results of the near-field energy confined in the gap of the bowtie antenna (d) for different separations using CEM (a) and QCM(b). Reprinted with permission from Ref. [90].....	29
Figure 3.1 a) Schematic diagram of the FIB machine [55] b) Hitachi FB2100 FIB at the University of Victoria [60]. Reprinted with permission from corresponding References.	31
Figure 3.2 Schematic diagram of the process of EBL. Reprinted with permission from Ref. [56].....	33
Figure 3.3 a) Schematic diagram of the electron exposure system b) A commercial EBL system. Reprinted with permission from Ref. [56]	33
Figure 3.4 a) Schematic diagram of the tape-peeling nanogap fabrication. b) Glancing-angle ion polishing process. c) SEM image of the patterned gold pillars array on a sapphire wafer, a very thin layer of Al ₂ O ₃ is deposited on the surface of the sample by using ALD. d) SEM image of the sample after deposition of the second layer of gold. e) SEM image of the sample after glancing –angle ion polishing. The scale bars in e-d are 150 nm. Reprinted with permission from Ref. [57]	35
Figure 3.5 Schematic diagram of the template stripping process: A gold thin film is evaporated on a flat template. A mechanical support is glued to the surface of the gold and then cleaved at the weakest adhesion point. The outcome of the process is a flat gold surface which its roughness is comparable to the template surface. Reprinted with permission from Ref. [58].....	36
Figure 3.6 Schematic diagram of the template stripping process flow a) the structure is milled on the silicon templates. b) The desired thickness of gold is deposited on the surface of the silicon template. (The deposited gold thickness must be less than the depth of the milled structure to avoid connection of the gold on the surface to the gold that fills the structure). A glass slide is attached to the surface of the sample by using UV epoxy c) UV exposure d) the DNH structures transferred to the glass slide after stripping. The silicon masters are reusable. Reprinted with permission from Ref. [85].....	37
Figure 3.7 a) Fabricated silicon template master. b) Template-stripped DNH with a gap of ~7 nm using the template shown in (a) c) Template-stripped DNH with a gap of ~12 nm. d) Template-stripped DNH with a gap of ~17 nm. Reprinted with permission from Ref. [85].....	38
Figure 3.8 The resolving power of the human eye, optical microscope and electron microscope [59].....	39
Figure 3.9 Illustration of the signals produced from the sample as a result of exposure to a focused electron beam [59].	40
Figure 3.10 Schematic diagram of SEM configuration [59].....	41
Figure 4.1 Schematic diagram of an experimental setup for SHG measurement. Reprinted with permission from Ref. [61]	44
Figure 4.2 a) THG spectra for single ITO nanoparticle b) THG spectra for ITO assembled nanoantenna c) THG power dependence. Reprinted with permission from Ref. [61]	45
Figure 4.3 a) Schematic diagram of the experimental setup where LPF is a low pass filter, HWP is a half wave plate, P is a polarizer, MR is a mirror, FR is a flipper mirror, BPF is	

a bandpass filter b) The THG spectra of the nanosphere assembled thin film structure c) Observed THG on the CCD camera [95].....	46
Figure 4.4 a,b,c) SEM images of the nanoantennas d) SHG as a function of the nanogap size e) The schematic diagram of the experimental setup in transmission geometry. Reprinted with permission from Ref. [23].....	47
Figure 4.5 a) The schematic of the optical setup used for investigation of the effects of b) angle of incidence, c) lattice arrangement and d) the hole size on the THG. Reprinted with permission from Ref. [33].....	48
Figure 4.6 The schematic of the optical setup used in the references [19,20] to investigate aperture-based THG in transmission geometry. Reprinted with permission from Ref. [19].....	49
Figure 5.1 a) Schematic illustration of the plasmonic nanostructure under THG measurement b) Tilted SEM image of the fabricated structures. Reprinted with permission from Ref. [63].....	51
Figure 5.2 Illustration of calculated TH efficiency on the linear extinction spectra using harmonic oscillator model and corresponding measured spectra for different lengths of nanoantenna. Reprinted with permission from Ref. [63].....	52
Figure 5.3 a) Illustration of parameter space: the length of the U-shaped structure arms are changed throughout the array b) Schematic of SHG and THG from the U-shaped structure: these nonlinear responses are a function of length and morphology of the structures. c) an SEM image of fabricated U-shape structures. Reprinted with permission from Ref. [67].....	53
Figure 5.4 Illustration of the calculated SHG using two different methods: Miller's theory and nonlinear scattering theory as compared to the measured values. Reprinted with permission from Ref. [67].....	54
Figure 5.5 Illustration of the nonlinear scattering theory: The source at the detector position radiates a field at the harmonic wavelength toward the structure. The emitted harmonic signal from the nonlinear system can be estimated by Eq. 5.10. Reprinted with permission from Ref. [67].....	55
Figure 5.6 a) Schematic of third harmonic generation from a rectangular aperture array b) Simulated configuration for incident fundamental and third harmonic waves (using time-reversal for the harmonic beam.	56
Figure 5.7 a) Calculated THG in natural logarithm scale using the nonlinear scattering theory of Eq. 2.24 for LSP resonance at 523 nm and SPP resonance at 1570 nm. b) Same as (a) for LSP and SPP resonance at 523 nm. c) Same as (a) for LSP and SPP resonance at 1570 nm. d) same as (a) for LSP resonance at 1570 nm and SPP resonance at 523 nm.	58
Figure 5.8 Scanning electron microscopy images of the fabricated structures on a 100 nm thick gold film for: (a) LSP resonance at 523 nm and SPP resonance at 1570 nm ($l=41$ nm, $P_y=1578$ nm). (b) LSP resonance at 523 nm and SPP resonance at 523 nm ($l=70$ nm, $P_y=400$ nm). (c) LSP resonance at 1570 nm and SPP resonance at 1570 nm ($l=310$ nm, $P_y=1546$ nm). (d) LSP resonance at 1570 nm and SPP resonance at 523 nm ($l=343$ nm, $P_y=528$ nm). Where l is the length of the rectangular aperture and P_y is the periodicity of the array in the y -direction. The width of the aperture (w) and the periodicity of the array in the x -direction (P_x) were fixed values of 30 nm and 1400 nm.....	59

Figure 5.9 a) Schematic of the experimental setup used to measure THG of the fabricated array of rectangles where LPF is low pass filter, BS is a beam splitter, HWP is half wave plate, FM is flip mirror, C is collimator and OF is an optical fiber. The inset shows the sample with the electric field polarization of the incident beam. b) Power dependence of measured THG (solid blue curve) on the input power in logarithm scale. The dashed red curve shows a fit with slope 3. c) Measured THG for the array designed for LSP resonance at 1570 nm and SPP resonance at 523 nm that yields the maximum conversion efficiency for a different length of the aperture and fixed $P_y = 518$ nm. d) Third harmonic green spot imaged on the CCD camera. e) The measured power spectrum of the pulsed laser source.....	60
Figure 5.10 Normalized third harmonic generation versus array parameters for different LSP and SPP resonance scenarios. Theoretical results from simulations are also shown.	61
Figure 6.1 Spatial distribution of electric field intensity at the metal surface in the xy plane for five different spacer sizes at wavelength 1570 nm. QCM has been used to achieve top row results whereas CEM results have been depicted in the bottom row.....	69
Figure 6.2 Spatial distribution of electric field intensity at the metal surface in the xz plane for five different spacer sizes at wavelength 1570 nm. QCM has been used to achieve top row results whereas CEM results have been depicted in the bottom row.....	69
Figure 6.3 THG intensity simulation results versus film-NP distance for QCM and CEM approaches. There is extraordinary suppression in field intensity as the gap size goes beyond 0.57 nm which is in extremely good agreement with our experimental results. ..	70
Figure 6.4 Local field intensity at the maximum point inside the gap under the nanoparticle using QCM (solid line) and CEM (dashed line) for different SAM layer types.....	70
Figure 7.1 Illustration of the geometry of the film-coupled nanoparticle a) sample b) the cross section view of a single film-coupled nanoparticle. Reprinted with permission from Ref. [96]	72
Figure 7.2 a) The position of peak scattering intensity versus gap size b) The field enhancement ratio as a function of gap size. Reprinted with permission from Ref. [96]	73
Figure 7.3 a) Plasmonic dimer within the framework of plasmon hybridization b) Measured extinction spectra as a function of gap size c) Tilted SEM image of the bowtie nanoantenna array. Reprinted with permission from Ref. [64].....	74
Figure 7.4 Comparison of the calculated and measured linear (left column) and nonlinear (right column) optical response of the bowtie nanoantenna for single and gap sizes: $g=60$, $g=30$ and $g=20$ nm. Reprinted with permission from Ref. [64].....	75
Figure 7.5 Measured spectrally integrated TH signal versus simulated TH signal based on single nonlinear oscillator model for the gap antennas (red) the glass covered bowtie (blue) and the bowties (black). Reprinted with permission from Ref. [64].....	76
Figure 7.6 Schematic diagram of a nanoantenna within the framework of coupled mode theory b) Simulation of the radiation pattern of the dipole nanoantenna on a quartz substrate. Reprinted with permission from Ref. [98]	78
Figure 7.7 a) The schematic diagram of a dipole nanoantenna with a small gap b) the electric magnitude distribution c) Quality factor plots as a function of the spacer thickness d) Field intensity enhancement as a function of space thickness: the maximum enhancement happens where the quality factor of absorption and radiation coincide. Reprinted with permission from Ref. [98].....	79

Figure 7.8 a) Absorption (blue curve) and scattering (red curve) cross section spectra for different gap sizes, w , of the slit configuration depicted in the inset. The polarization of the incident light is parallel to the width, w , of the slit. The thickness of the gold film is 100 nm. b) Resonant THG prediction based on nonlinear scattering theory (red) and corresponding absorption and scattering (black) for different gap sizes, w , of the slit. Note that the optimal THG occurs when the absorption and scattering cross sections are equal.....	81
Figure 7.9 Calculated normalized THG versus inner ring diameter in annular ring structures using Eq. 3.1 for different gap sizes: a) 6 nm b) 8 nm c) 10 nm d) 12 nm e) 14 nm f) 16 nm.....	83
Figure 7.10 (a) THG incident power dependence is shown on a logarithmic scale with a slope of 3.07. (b) Measured THG signal from the spectrometer. (c) Linear transmission spectra of the annular ring structures for different gap sizes and fixed ring diameter of 90 nm.....	83
Figure 7.11 Measured THG signals versus inner ring diameter in the annular ring structures for different gap sizes: (a) 6 nm (b) 8 nm (c) 10 nm (d) 12 nm (e) 14 nm (f) 16 nm.....	84
Figure 7.12 a) Measured THG spectra for different aperture geometries and periodicities; array 1: array of rectangular aperture, $w=20$ nm, $l=343$ nm, $P_x=518$ nm; array 2: DNH, $g=60$ nm, $P_x=518$ nm; array 3: rectangle, $w=40$ nm, $l=343$ nm, $P_x=518$ nm; array 4: DNH, $g=60$ nm, $P_x=410$ nm, array 5: H-shaped, $g=40$ nm, $P_x=410$ nm; array 6: H-shaped, $g=40$ nm, $P_x=530$ nm where w is the width of rectangular aperture, l is the length of rectangular aperture, g is the gap size of the DNH and H-shaped aperture, and P_x is the periodicity of the array in the direction of the fundamental wave polarization b) SEM image of the optimum H-shaped array structure for THG c) SEM image of the optimum DNH array structure for THG.....	85
Figure 8.1 Examples of damaged structures a) disconnected structures b) connected structures.....	89
Figure 8.2 The schematic diagram of a linear plasmonic lens with cross-shaped apertures. Reprinted with permission from Ref. [103].....	90
Figure 8.3 The transmission efficiency and the corresponding phase of the transmitted light as a function of arm length. Reprinted with permission from Ref. [103].....	90
Figure 8.4 a) The calculated phase associated with apertures in a 2D array along x-axis b) The calculated arm length associated with apertures in a 2D array along the x-axis. Reprinted with permission from Ref. [103].....	91
Figure 8.5 Intensity profile of the transmitted light in z direction a) apertures with fixed arm lengths (250 nm) b) designed lens with $f_D=15$ μm c) designed lens with $f_D=25$ μm d-h) 2D intensity profile at $z=0, 14, 21,$ and 28 μm . Reprinted with permission from Ref. [103].....	92
Figure 8.6 A) Schematic diagram of metasurface with a) a uniform unit cell b) phase gradient unit cell. Corresponding observed transmitted light observed on the CCD camera c) uniform unit cell d) phase gradient unit cell. Reprinted with permission from Ref. [104].....	93
Figure 8.7 a) phase of the transmitted light through a metasurface with rectangular aperture b) corresponding transmission as a function of the aperture length.....	94

Figure 8.8 SEM images of the fabricated metasurface wave plates to control TH beam polarization.....	94
Figure D.1 The SEM images of the fabricated structures in the gold and aluminum thin films. Aluminum shows better performance regarding THG at 1.57 μm . Reprinted with permission from Ref. [19].....	104
Figure D.2 a) The SEM image of fabricated SHR in an aluminum thin film b) the spatial electric field distribution in the aperture at the fundamental wavelength of 1560 nm c) the captured third harmonic signal on the CCD d) The measured third harmonic signal on the spectrometer. The conversion efficiency is around 10^{-5} . Reprinted with permission from Ref. [20].	105
Figure D.3 a) THG spectra of a single double nanohole as a function of the hole radius and the spacing between two holes b) THG spectra of a single SHR as a function of the nanorod length and the diameter of the hole. The scaled version of the structures has been shown in the plots.....	106
Figure D.4 THG spectra of different template-stripped single DNH aperture with sub 20 nm gaps	107

Acknowledgments

First of all, I would like to express my gratitude to my supervisor, Dr. Reuven Gordon, for his mentorship and supports. His brilliant ideas, attitudes and leadership style were really motivating.

I also would like to thank my supervisory committee members, Dr. Harry Kwok and Dr. Byoung-Chul Choi, and the external examiner Dr. Xiaojin Jiao for their comments on my work that, indeed, helped me to improve the quality of this dissertation.

Over the course of my Ph.D., I always benefited from helpful consultation with my colleagues at the Nanoplasmonics Research Laboratory. I would like to thank all of them.

I would like to express my acknowledgment to Dr. Thomas E. Darcie, Dr. Thomas Tiedje and their group members, Afshin Jooshesh, Levi Smith, Dr. Vahid Bahrami-Yekta and Mahsa Mahtab for their cooperation

I am also grateful to Dr. Elaine Humphrey for her valuable advice and technical support at the Advanced Microscopy Facility (AMF).

Special thanks to Dr. Ahmad Shakibaeinia, Maryam Alizadeh and Dr. Ghazal Hajisalem that were really supportive whenever things did not go very well. Their advice during such hard time helped me to move forward.

Steven Jones kindly helped me to improve the quality of the text. I would like to thank him for his time.

Last but not least, I would like to express my gratitude to my family, for all their encouragements and supports. My parents' faith in my abilities was the key factor that brought me this far. I would like to thank my wife, Nooshin, for her love and supports. Special thanks to my daughter, Avin, who was patient whenever I had to say "No" to her play demands.

Dedication

This thesis is dedicated to my family: *my parents*, Abbasali, and Mahin, for all their kind supports; *my wife*, Nooshin, for her endless love and Avin, *my beloved daughter*

Glossary

List of symbols:

$\chi^{(3)}$	Third order susceptibility
P	Polarization
k_{SP}	Wave number of surface plasmons
ε_m	Frequency-dependent permittivity of metal
ε_d	Dielectric permittivity
γ_p	Collision frequency of electrons
ω_p	Metal surface electron plasma frequency
α	Polarizability
β_{TE}	Propagation constant of TE mode
β_{TM}	Propagation constant of TM mode
λ_c	Cut-off wavelength
E	Electric field vector
D	Displacement vector
H	Magnetic field vector
B	Magnetic flux density vector
J_{ext}	External current density vector
$\lambda_{cut-off}$	Cut-off wavelength of TE mode
T	Transmission efficiency
r	Hole radius
λ	Wavelength of incident light
λ_{max}	Peak location of transmitted light
a_0	Periodicity of subwavelength apertures
σ	Conductivity
ω_g	Plasma frequency of the gap region
m	Effective mass of electron
Ψ	Electron wave function
\hbar	Reduced Planck's constant
E_f	Fermi energy
φ_B	Barrier height
κ	Electron wave vector

Abbreviations:

EOT	Extraordinary Optical Transmission
SHG	Second Harmonic Generation
THG	Third Harmonic Generation
QCM	Quantum Corrected Model
DNH	Double Nano-Hole
SPP	Surface Plasmon Polariton
LSP	Localized Surface Plasmon
CEM	Classical Electromagnetic Model
FIB	Focused Ion Beam
EBL	Electron Beam Lithography
SEM	Scanning Electron Microscopy
ALD	Atomic Layer Deposition
CCD	Charge-Coupled Device
CMT	Coupled Mode Theory

Chapter 1 : Introduction

1.1 Motivation

Electromagnetic metasurfaces are artificial sheet materials that could be designed for desired electromagnetic properties. They could be structured or non-structured with subwavelength patterns in horizontal dimensions [1]. Metasurfaces can be utilized to enhance the nonlinear optical response of a metal thin film thereby further improving its functionality in applications such as wavelength conversion, optical switching, near-field imaging, subwavelength lithography and spectroscopy. Aperture-based metasurfaces are good candidates for this purpose due to their ability to remove heat from the surface and localize light within a subwavelength region. Since the discovery of the extraordinary optical transmission (EOT) through the circular nanohole arrays [2], aperture-based metasurfaces have been considered in nonlinear optical applications. Many researchers have been focusing on second and third harmonic generation (SHG and THG) from these structures [19-35].

1.2 Research Objectives

1.2.1 The Influence of Localized and Propagating Surface Plasmon Resonance on THG of Nanostructures

The objective of this research was to achieve the greatest possible third harmonic conversion efficiency resulting from enhancement by aperture-based metasurfaces. We took advantage of coupling localized and propagating surface plasmon resonances to the fundamental and third harmonic wavelength to enhance THG. This work also investigated the effect of gap plasmons on THG. A 0.5 % conversion efficiency was observed for an array of the H-shaped aperture which is the greatest efficiency value for the aperture-based structures. Nonlinear scattering theory was utilized to estimate the

THG of the aperture arrays. Our simulation results were in good agreement with the experimental results. Details are presented in Chapters 5 and 7.

1.2.2 The Effect of Quantum Electron Tunneling on THG

The quantum mechanical effects on the THG from plasmonic structures had not been investigated, to this end we explored the effect of quantum tunneling on THG. In this work, a modified quantum-corrected model (QCM) was used to predict the third order nonlinear optical response of a plasmonic structure with the gap sizes in the range of 0.51 nm to 1.55 nm. Our model was able to interpret the THG behavior of these structures on the onset of tunneling. Chapter 6 describes this model in detail, and further the results are discussed.

1.2.3 Gap Plasmons Effect on THG Efficiency of Nanostructures

In this project, the influence of gap size on THG was investigated. For this purpose, aperture arrays such as annular ring, H-shaped, double nanohole (DNH) and rectangular apertures were considered. Gap plasmon effects have been studied extensively in recent years [40,64,96,98]; however, there was a lack of knowledge regarding the effect of gap size in THG enhancement. For non-resonant structures, it had been found that as the gap size is decreased the THG is enhanced but in the resonant case and in particular in aperture-based transmission, the optical resistive loss in inside the apertures also plays a major role in THG enhancement. It had also been shown, recently, that the radiated power from a nanoantenna is maximized if the quality factor of absorption and scattering are equal [98]. In this project, we applied radiation engineering for enhanced aperture-based THG. These concepts are discussed in Chapter 7.

1.3 Overview of Thesis

In Chapter 2, some applications and past works in the field are presented. The fundamentals and the theory involved in the project are also discussed in Chapter 2. Chapter 3 is devoted to the experimental methods including fabrication and characterization methods related to the aperture-based metasurfaces. The experimental methods in THG measurement of the plasmonic metasurfaces are discussed in Chapter 4. Chapter 5 is devoted to the influence of localized and propagating surface plasmons in aperture-based THG. In Chapter 6, the influence of the quantum tunneling on THG in very small gap sized plasmonics structures is examined. The radiation engineering for enhanced THG is considered in Chapter 7. Chapter 8 presents the proposed future works.

Chapter 2 : Background and Previous Works

Extraordinary optical transmission through an array of subwavelength apertures [2] opened a new window in the field of photonic device research. Since then many efforts have been made to improve functionality of a thin flat layer by using metasurfaces [3-10] in the application such as optical switching [11,12], wavelength conversion [13], near-field imaging [14,15], subwavelength lithography [16] and spectroscopy [17]. Nonlinear metasurfaces are also of interest to many researchers around the world. While there are many works in the field of second harmonic generation from metasurfaces, there are quite a few works that study third harmonic generation from the aperture arrays. Nonlinear optical response of the materials is usually very weak, so many attempts have been made to improve the efficiency of the phenomena. Aperture based metasurfaces are considered as suitable structures due to their ability to remove heat from the surface and also to localize the electric field [18-20]. The aperture's localized surface plasmon (LSP) resonance can be manipulated by the aperture shape [20-25] and surrounding medium [26,27], which consequently leads to a higher conversion efficiency. Propagating surface plasmon polaritons (SPP) can be tuned to the Bragg resonance to improve the nonlinear optical response [28-35]. Larger intensities can be obtained with more intense pulse sources; however, material damage (for 100 nm gold on a fused silica substrate damage occurs at around $10 \text{ mW}/\mu\text{m}^2$ [36,37] and close to $1 \text{ mW}/\mu\text{m}^2$ for nanostructures with tiny gaps [38]). Saturation of the nonlinear response [39] is also a limiting factor.

The fundamental beam power can be enhanced locally at the metal surface by gap plasmons. It has been shown that the field intensity enhancement in the gap region is inversely proportional to the gap size [40]. This intensity enhancement facilitates a

nonlinear optical response of the metasurfaces [41,42]. Quantum tunneling, however, limits this enhancement at the subnanometer regime which is discussed in Chapter 6. There are four main reasons that we focus on the third harmonic. SHG is dipole forbidden in gold due to its centrosymmetry [43]. THG has a cubic dependence on the fundamental wavelength beam's power [43]; therefore, higher conversion efficiencies are achievable at increased power levels. Interband transition of the gold are close to the THG energy at the fundamental of 1500~1600 nm, so it is possible to use high-power fiber-based lasers for compact wavelength conversion [44]. Kerr-like switching is allowed in the susceptibility of gold, $\chi^{(3)}$, that might be of interest in future switching applications [45]. Moreover, the high sensitivity of THG to the near-field intensity makes it very efficient in near-field spectroscopy applications [46].

2.1 Third Harmonic Generation

Nonlinear optical properties of the material can be studied by using a very intense source of light. This source usually is a pulsed laser that delivers a high amount of energy in a small fraction of the time. Polarization, P , happens as a consequence of the laser exposure [43]:

$$P = \varepsilon_0 \left[\chi^{(1)} E + \chi^{(2)} E^2 + \chi^{(3)} E^3 + \dots \right] \equiv P^{(1)}(t) + P^{(2)}(t) + P^{(3)}(t) + \dots \quad (2.1)$$

Where ε_0 is the permittivity of the free space, $\chi^{(1)}$, $\chi^{(2)}$ and $\chi^{(3)}$ are first, second and third order susceptibility of the material, E is the incident electric field, $P^{(1)}(t)$, $P^{(2)}(t)$ and $P^{(3)}(t)$ are first (linear), second and third order (nonlinear) polarizations of the material. When the incident field is not strong enough, higher orders are typically negligible. Fig. 2.1.a shows the process of THG. Fig. 2.1.b is a photon description of the

THG process. As depicted in this figure, three photons at the fundamental frequency (ω) are destroyed to create one photon at three times (3ω) higher frequency.

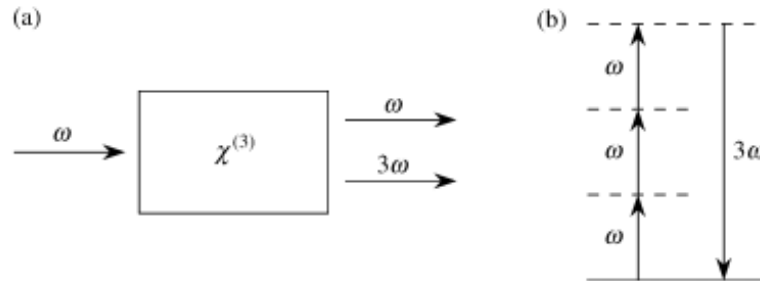


Figure 2.1 a) the third harmonic generation process b) photon description of the THG. Reprinted with permission from Ref. [43].

2.2 Plasmonics

2.2.1 Surface Plasmon Polaritons

Surface plasmon polaritons (SPPs) are collective oscillations of the electromagnetic waves and charged electron particles at a metal-dielectric interface. SPPs can be confined within regions much smaller than the wavelength of the incident light; this phenomenon makes it suitable for applications such as biomedical sensing, near-field imaging, and nonlinear optical spectroscopy. Due to the lower momentum of the incident photons than delocalized surface electrons, light cannot be coupled to the electron waves through the air. To increase the momentum of the photons, a prism or grating is used. Figure 2.2 shows the phase matching of the incident photons and SPPs by using attenuated total reflection in Otto and Kretschmann configurations. The reflected beam at the interface of the metal and the higher refractive index material (prism), ϵ , has an in-plane wave vector of $k_{||} = k\sqrt{\epsilon} \sin \theta$, where k is the free-space wave vector and θ is the angle of incidence. This wave vector is sufficient to excite the SPPs at the interface between the metal and

the lower index material. The grating method for the phase matching will be discussed later on section 2.3.

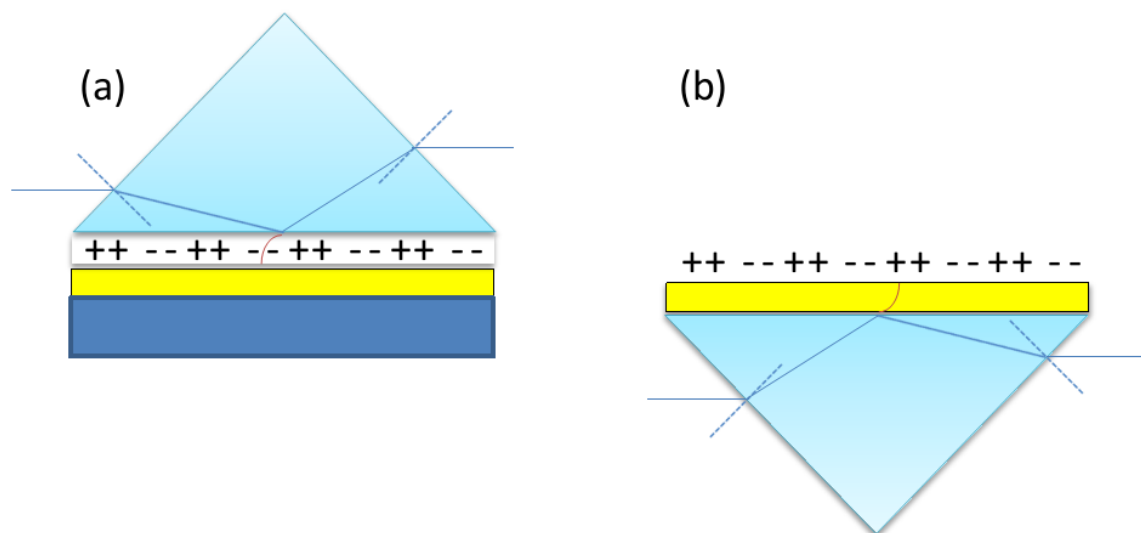


**Figure 2.2 Prism coupling using attenuated total internal reflection in a) Otto configuration
b) Kretschmann configuration**

Noble metals such as gold, silver and copper are good candidates for plasmonics applications. Interband transition of gold close to the third harmonic at a fundamental of 1400 to 1600 nm contributes in enhancing the third order nonlinear susceptibility of gold that further enhance the THG. Therefore, using a fundamental wavelength of 1550 nm, which extensively is used in telecommunications, can stimulate the interband transition of gold at the wavelengths close to the third harmonic wavelength around 520 nm. Once the free-space light is coupled to the surface charges, the surface plasmons propagate along the metal-dielectric interface and also evanescently decay perpendicular to the interface in both the metal and the dielectric regions [47]. Using the Drude model, the wave vector of SPPs can be estimated by:

$$k_{SP} = k_0 \sqrt{\frac{\epsilon_m \epsilon_d}{\epsilon_m + \epsilon_d}} \quad (2.2)$$

$$\epsilon_m(\omega) = \epsilon_\infty - \frac{\omega_p^2}{\omega(\omega + i\gamma_p)} \quad (2.3)$$

Where $k_0 = \frac{\omega}{c}$ is the free-space wave vector, ϵ_m is the frequency-dependent permittivity of the metal which is a complex number and ϵ_d is the dielectric permittivity. The first term in Eq. 2.3, ϵ_∞ , is the background dielectric constant due to the contribution of the bound valence electrons and the second terms is the contribution from the conduction electrons. ω_p is the metal surface electron plasma frequency and γ_p is the collision frequency of the electrons.

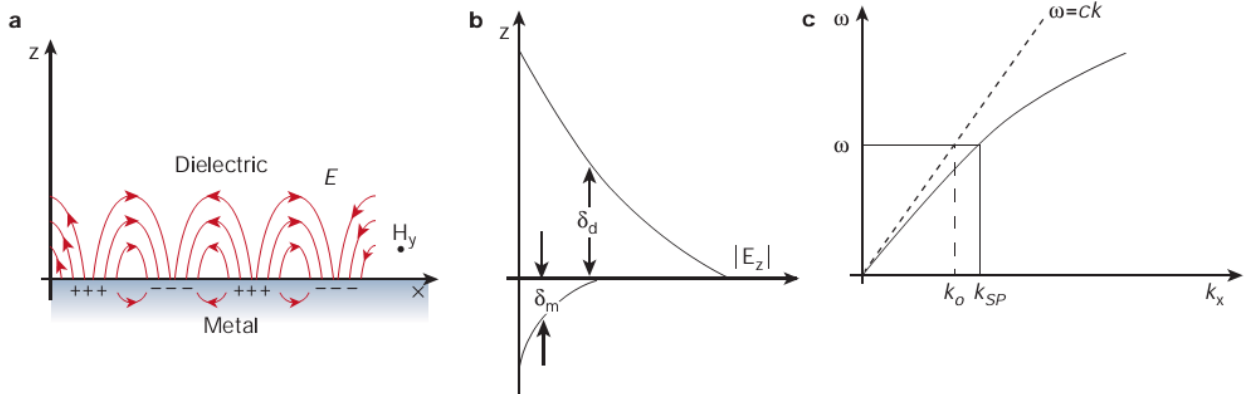


Figure 2.3 Surface plasmon polaritons a) propagating waves bounded to the metal-dielectric interface b) Evanescent waves into the metal and dielectric material perpendicular to the interface c) Typical dispersion curve. Reprinted with permission from Ref. [47]

Fig. 2.3.a shows the propagating surface plasmon waves along the metal-dielectric interface. Fig. 2.3.b shows the evanescent waves perpendicular to the metal-dielectric interface. These waves decay into the metal and dielectric media and Fig. 2.3.c shows the typical SPPs dispersion curve.

Solving Maxwell's equation at the metal-dielectric interface, we can derive the propagating electric field along the metal-dielectric interface and also evanescent wave perpendicular to the interface at the both sides of the metal. The length of propagation which is in the range of a few microns to 1 mm can be derived from [47]:

$$\delta_{SP} = \frac{1}{2k''_{SP}} = \frac{c}{\omega} \left(\frac{\epsilon'_m + \epsilon_d}{\epsilon'_m \epsilon_d} \right)^{\frac{3}{2}} \frac{(\epsilon'_m)^2}{\epsilon''_m} \quad (2.4)$$

$$k_{SP} = k'_{SP} + ik''_{SP} \quad (2.5)$$

$$\epsilon_m = \epsilon'_m + i\epsilon''_m \quad (2.6)$$

Fig. 2.4 compares the SP propagation length of aluminum and silver for the wavelength of 500 nm and 1.5 microns. Since aluminum is a fairly absorbing metal in the visible range of the spectrum, propagating SPs decay faster than in silver as the lowest lossy metal in the range.

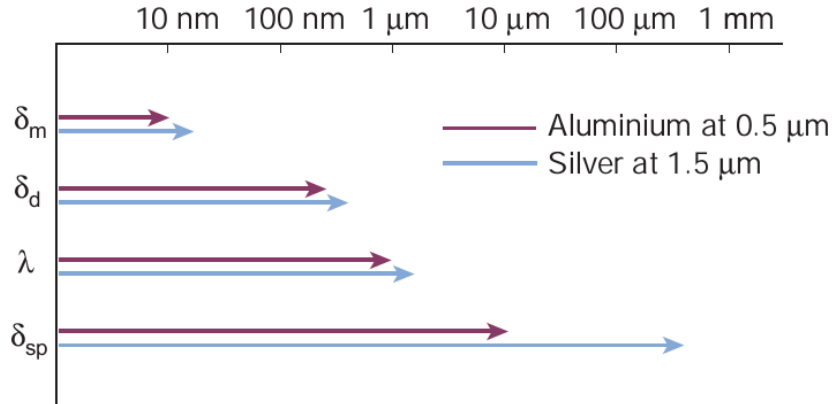


Figure 2.4 Propagation length of the SPPs for Aluminum and Silver. Reprinted with permission from Ref. [47]

2.2.2 Localized Surface Plasmons

Light can locally be coupled to the surface plasmons inside an aperture or around a defect on the surface of the metal or in a metallic nanoparticle. Unlike propagating SPs

that can travel along the metal-dielectric interface and exist for a wide range of the frequency spectrum, localized surface plasmons (LSPs) are confined in a subwavelength region and their resonance associated with the bound electron plasmas inside the aperture or nanoparticle. They are very sensitive to the shape and the refractive index of the surrounding media.

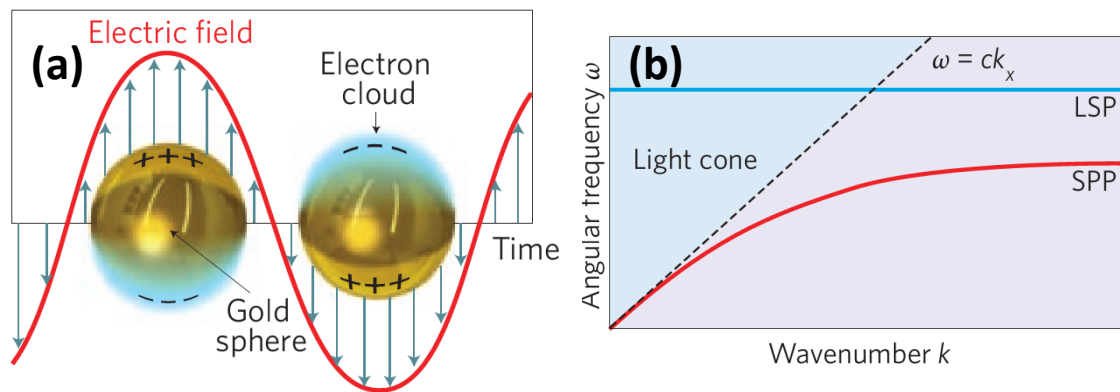


Figure 2.5 a) Localized surface plasmons b) comparison of the typical dispersion curve of LSPs with SPPs. Reprinted with permission from Ref. [48]

Fig. 2.5.a shows the LSPs associated with the electron plasmas in the nanoparticle. Fig. 2.5.b shows the typical dispersive curve of the propagating and localized surface plasmons.

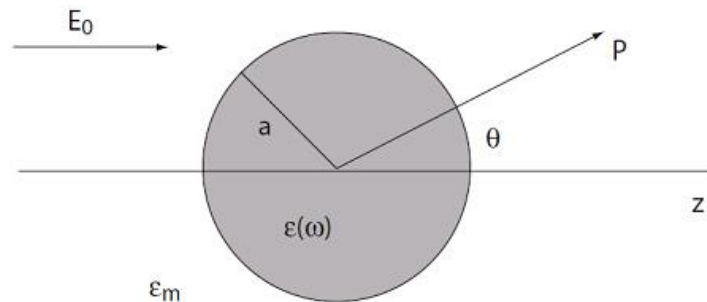


Figure 2.6 A homogeneous metal sphere exposed to electric field E_0 . Reprinted with permission from Ref. [49]

These are plotted in a lossless metal. As it can be seen the group velocity, $\frac{\delta\omega}{\delta k}$, of the propagating surface plasmons at extremely large propagation constants goes to zero. However, in real metals, due to the inherent loss contribution, the dispersion curve folds back and cross the light line. Therefore, the actual group velocity at an infinite propagation constant is not zero. Fig. 2.6 shows a homogeneous sphere that is exposed to electric field of \mathbf{E}_0 . The applied electric field induces a dipole moment inside the nanoparticle the can be represented by [49]:

$$\mathbf{p} = \varepsilon_0 \varepsilon_d \alpha \mathbf{E}_0 \quad (2.7)$$

Where α is the polarizability of the nanoparticle that can be derived from [49]:

$$\alpha = 4\pi a^3 \frac{\varepsilon_m - \varepsilon_d}{\varepsilon_m + 2\varepsilon_d} \quad (2.8)$$

Where a is the radius of the subwavelength nanoparticle sphere. From Eq. 2.8 it can be seen that the polarizability has a resonance condition of:

$$Re[(\varepsilon_m(\omega))] = -2\varepsilon_d \quad (2.9)$$

This equation is called the Fröhlich condition. The field inside, \mathbf{E}_{in} , and outside, \mathbf{E}_{out} , of the nanoparticle can be estimated by:

$$\left\{ \begin{array}{l} \mathbf{E}_{in} = \frac{3\varepsilon_d}{\varepsilon_m + 2\varepsilon_d} \mathbf{E}_0 \\ \mathbf{E}_{out} = E_0 + \frac{3n(\mathbf{n} \cdot \mathbf{p}) - \mathbf{p}}{4\pi\varepsilon_0\varepsilon_d} \frac{1}{r^3} \end{array} \right. \quad (2.10)$$

Where \mathbf{n} is the unit vector in the direction of the point of interest. Both internal and dipolar field are enhanced under Fröhlich condition.

Previously the theory of transmission of the light through a rectangular aperture has been developed. In the theory, the TE and TM rectangular aperture modes have been considered. Only zero-order TE mode is required to estimate the resonance wavelength of the aperture. This resonance is close to the cut-off wavelength of the aperture [50,51,73].

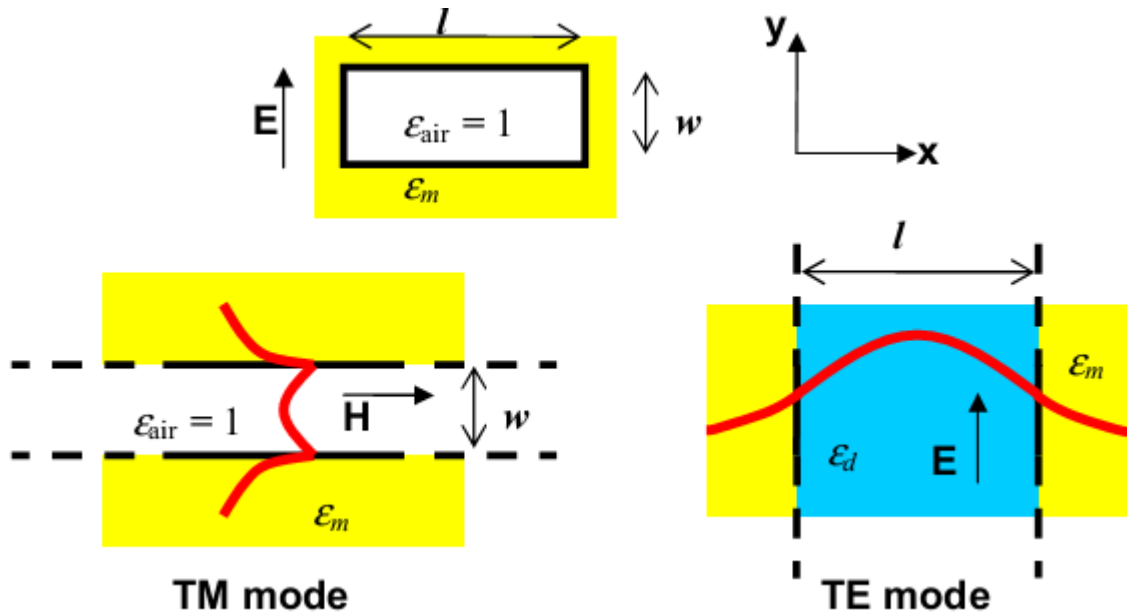


Figure 2.7 Schematic of the rectangular waveguide: The effective dielectric constant of the lowest TE mode is derived by considering the TM mode of the slab. Reprinted with permission from Ref. [50].

Fig. 2.7 shows a rectangular aperture which is illuminated by a normally incident plane wave. The propagation constant of the lowest order TE mode in a rectangular aperture perforated in the perfect electric conductor (PEC) is represented by [50]:

$$\beta_{TE} = \pi \sqrt{\left(\frac{2}{\lambda}\right)^2 - \left(\frac{1}{l}\right)^2} \quad (2.11)$$

Where l is the length of the rectangle. It can be seen that the cut-off wavelength of PEC is [50]:

$$\lambda_c = 2l \quad (2.12)$$

To estimate the cut-off wavelength of the rectangular aperture in a real metal, one can use the effective index method [50]. In this approach, the effective index of the structure for propagating TM mode of the aperture along the x direction is used to calculate the cut-off wavelength of the TE mode along the y direction. The in-plane component of the incident electric field is perpendicular to the long edge of the aperture. To obtain the characteristic equations for TE and TM modes, we can solve the problem for a multilayer metal-insulator-metal (MIM) structure that is very similar to the case of the rectangular aperture on a gold film. Fig.2.8 shows the geometry of three-layer MIM structure. A thin layer of dielectric I sandwiched between two layers of metals II and III.

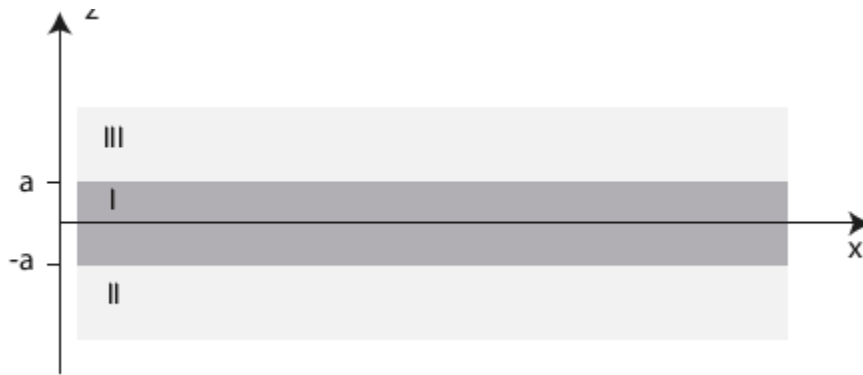


Figure 2.8 Geometry of a three-layer system. Reprinted with permission from Ref. [49]

Both interfaces in this configuration can sustain bound SSPs. In this approach, we are just interested in the lowest order bound modes. Assuming flat interfaces between metal and dielectric, simplify the problem. In this case, electromagnetic waves are essentially two-dimensional. Therefore, they propagate in the x and y directions. Applying Maxwell's equations to the interface, results in the electromagnetic wave equation:

$$\nabla \times \nabla \times \mathbf{E} = -\mu_0 \frac{\partial^2 \mathbf{D}}{\partial t^2} \quad (2.13)$$

Where \mathbf{E} is the electric field vector, \mathbf{D} is the displacement vector and μ_0 is the permeability of the free-space. It can be proved that:

$$\nabla \times \nabla \times \mathbf{E} \equiv \nabla(\nabla \cdot \mathbf{E}) - \nabla^2 \mathbf{E} \quad (2.14)$$

$$\nabla \cdot (\varepsilon \mathbf{E}) \equiv \mathbf{E} \cdot \nabla \varepsilon + \varepsilon \nabla \cdot \mathbf{E} \quad (2.15)$$

It is also known that under no external stimuli, the external charge density is zero ($\rho_{ext} = 0$) and, consequently, $\nabla \cdot \mathbf{D} = 0$. Therefore, the Eq. 2.13 can be rewritten as the Helmholtz equation:

$$\nabla^2 \mathbf{E} + k_0^2 \varepsilon \mathbf{E} = 0 \quad (2.16)$$

Where $k_0 = \frac{\omega}{c}$ is the wave vector of the propagating wave in the vacuum. The next step in this approach is defining the geometry of the structure. We assume that the electromagnetic wave propagates along the x-direction in the Cartesian coordinate system. From Maxwell's equations we know:

$$\nabla \times \mathbf{E} = -\frac{\partial \mathbf{B}}{\partial t} \quad (2.17)$$

$$\nabla \times \mathbf{H} = \mathbf{J}_{ext} + \frac{\partial \mathbf{D}}{\partial t} \quad (2.18)$$

Where \mathbf{B} is the magnetic flux density, \mathbf{H} is the magnetic field and \mathbf{J}_{ext} is external current density. Using Eqs. 2.17 and 2.18 and considering lowest order TM mode, where we have just H_y , E_x and E_z components, for $Z > a$ we derive:

$$H_y = A e^{i\beta_{TM}x} e^{-k_3z} \quad (2.19)$$

$$E_x = iA \frac{1}{\omega \varepsilon_0 \varepsilon_3} k_3 e^{i\beta_{TM}x} e^{-k_3z} \quad (2.20)$$

$$E_z = -A \frac{\beta_{TM}}{\omega \varepsilon_0 \varepsilon_3} e^{i\beta_{TM}x} e^{-k_3z} \quad (2.21)$$

For $Z < -a$ we can obtain the equations as:

$$H_y = B e^{i\beta_{TM}x} e^{k_2 z} \quad (2.22)$$

$$E_x = -iB \frac{1}{\omega \varepsilon_0 \varepsilon_2} k_2 e^{i\beta_{TM}x} e^{k_2 z} \quad (2.23)$$

$$E_z = -B \frac{\beta_{TM}}{\omega \varepsilon_0 \varepsilon_3} e^{i\beta_{TM}x} e^{k_2 z} \quad (2.24)$$

In the region $-a < z < a$ where k_1 , k_2 and k_3 denote the components of the wave vectors perpendicular to the interfaces, coupling of the bottom and top localized modes at the interfaces results in:

$$H_y = C e^{i\beta_{TM}x} e^{k_1 z} + D e^{i\beta_{TM}x} e^{-k_1 z} \quad (2.25)$$

$$E_x = -iC \frac{1}{\omega \varepsilon_0 \varepsilon_1} k_1 e^{i\beta_{TM}x} e^{k_1 z} + iD \frac{1}{\omega \varepsilon_0 \varepsilon_1} k_1 e^{i\beta_{TM}x} e^{-k_1 z} \quad (2.26)$$

$$E_z = C \frac{\beta_{TM}}{\omega \varepsilon_0 \varepsilon_3} e^{i\beta_{TM}x} e^{k_1 z} + D \frac{\beta_{TM}}{\omega \varepsilon_0 \varepsilon_3} e^{i\beta_{TM}x} e^{-k_1 z} \quad (2.27)$$

At $Z = a$ the continuity of H_y and E_x results in:

$$A e^{-k_3 a} = C e^{k_1 a} + D e^{-k_1 a} \quad (2.28)$$

$$\frac{A}{\varepsilon_3} k_3 e^{-k_3 a} = -\frac{C}{\varepsilon_1} k_1 e^{k_1 a} + \frac{D}{\varepsilon_1} k_1 e^{-k_1 a} \quad (2.29)$$

At $Z = -a$ we obtain:

$$B e^{-k_2 a} = C e^{-k_1 a} + D e^{k_1 a} \quad (2.30)$$

$$-\frac{B}{\varepsilon_3} k_3 e^{-k_3 a} = -\frac{C}{\varepsilon_1} k_1 e^{-k_1 a} + \frac{D}{\varepsilon_1} k_1 e^{k_1 a} \quad (2.31)$$

Since H_y has to fulfill the wave equation below for TM mode in the three regions:

$$\frac{\partial^2 H_y}{\partial z^2} + (k_0^2 \varepsilon - \beta^2) H_y = 0 \quad (2.32)$$

That yields:

$$k_i = \beta^2 - k_0^2 \varepsilon_i \quad \text{for } i = 1,2,3 \quad (2.33)$$

Solving these set of equation, yield [49]:

$$e^{-4k_1 a} = \frac{k_1/\varepsilon_1 + k_2/\varepsilon_2}{k_1/\varepsilon_1 - k_2/\varepsilon_2} \frac{k_1/\varepsilon_1 + k_3/\varepsilon_3}{k_1/\varepsilon_1 - k_3/\varepsilon_3} \quad (2.34)$$

Considering $\varepsilon_2 = \varepsilon_3$ and $k_2 = k_3$, we derive dispersion relation equations:

$$\tanh k_1 a = -\frac{k_2 \varepsilon_1}{k_1 \varepsilon_2} \quad (2.35)$$

$$\tanh k_1 a = -\frac{k_1 \varepsilon_2}{k_2 \varepsilon_1} \quad (2.36)$$

Where Eq. 2.35 is associated with long range surface plasmons and Eq. 2.36 represents the short range surface plasmons contribution. In the rectangular aperture structure, we can take $\varepsilon_2 = \varepsilon_m$ and $\varepsilon_1 = \varepsilon_{air}$. The TM mode between two parallel plates of a real metal propagating along the x direction can be derived from the TM mode characteristic equation [50]:

$$\tanh \left(\sqrt{\beta_{TM}^2 - k_0^2 \varepsilon_{air}} \frac{W}{2} \right) = \frac{-\varepsilon_{air} \sqrt{\beta_{TM}^2 - k_0^2 \varepsilon_m}}{\varepsilon_m \sqrt{\beta_{TM}^2 - k_0^2 \varepsilon_{air}}} \quad (2.37)$$

Where $W = 2a$ and β_{TM} is the propagation constant of the TM mode of the aperture along the x direction. The effective dielectric constant, ε_d , of the medium and can be derived from:

$$\varepsilon_d = \left(\frac{\beta_{TM}}{k_0} \right)^2 \quad (2.38)$$

The TE propagating mode is associated with the coupling of the SP waves on the opposite long edges of the aperture is represented by the TE mode characteristic equation that can be derived by using the same approach for the TM mode [50]:

$$\tan\left(\sqrt{k_0^2 \varepsilon_d - \beta_{TE}^2} \frac{l}{2}\right) = \frac{\sqrt{\beta_{TE}^2 - k_0^2 \varepsilon_m}}{\sqrt{k_0^2 \varepsilon_d - \beta_{TE}^2}} \quad (2.39)$$

Where β_{TE} is the propagation constant of the TE mode of the aperture along the y direction. Assuming $\beta_{TE} = 0$, the cut-off wavelength of a real metal can be obtained by [50]:

$$\lambda_{cut-off} = \frac{\pi l \sqrt{\varepsilon_d}}{\arctan \sqrt{-\varepsilon_m / \varepsilon_d}} \quad (2.40)$$

The calculated cut-off wavelength of the TE mode of the rectangular aperture resulted from this approach, occurs at the wavelengths longer than $2l$. It has also been shown that the material losses can be neglected in the wavelengths above the cut-off wavelength [50]. Fig. 2.9 shows the cut-off attenuation and the attenuation resulted from the material losses for a rectangular hole of 105 nm by 270 nm.

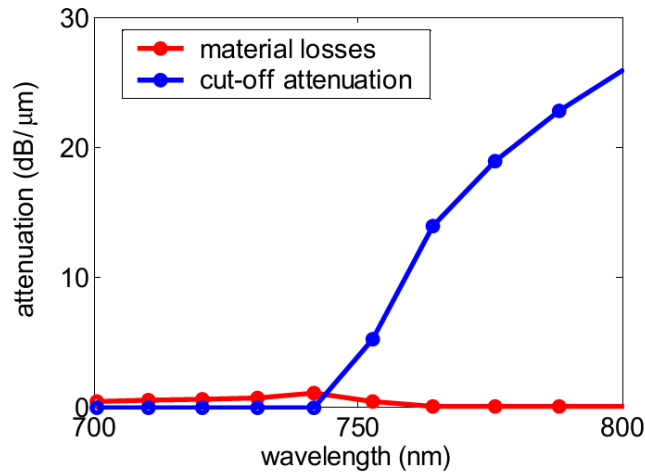


Figure 2.9 The attenuation resulted from material losses and the cut-off attenuation for a rectangular aperture of 105 nm by 270 nm. Reprinted with permission from Ref. [50].

For a rectangular aperture in metal, it has also been shown that the field enhancement inside the aperture is associated with the maximum transmission through the aperture. FDTD simulation shows that the field appears on the ridge of the aperture in the y

direction and has a dipolar nature. This proves the contribution of LSPs in the transmission resonance (Fig. 2.10).

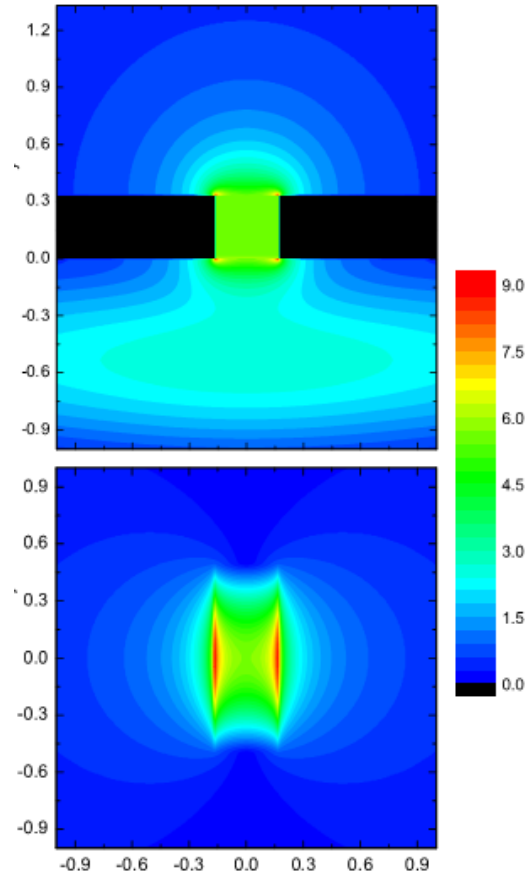


Figure 2.10 The spatial electric field distribution in a rectangular aperture in the gold film: The electric field component of the incident field is perpendicular to the longer side. Reprinted with permission from Ref. [51].

It has also been shown that a zeroth-order Fabry-Perot resonance close to the cut-off wavelength exists in the transmission even for a very thin layer of the metal. This is related to the presence of a negative phase shift associated with reflection [52].

In this project, we used FDTD simulation to adjust the LSP resonance of the rectangular aperture to the fundamental and third harmonic beam wavelength. Since the LSP resonance is associated with the field enhancement inside the aperture, a peak in the

transmission spectra is observable. This is the major peak in the transmission spectra of the single rectangular aperture. The details will be discussed in Chapter 5.

2.3 Extraordinary Optical Transmission

According to the classical electromagnetic theory, apertures that are smaller than half of the wavelength of the transmitted light do not support any propagating modes. However, if they are in a square array with a carefully engineered periodicity, they can go beyond this limitation. The transmission efficiency can also exceed Bethe's theory for a single hole [53]:

$$T \propto \left(\frac{r}{\lambda}\right)^4 \quad (2.41)$$

Where r is the hole radius. In a square array of subwavelength apertures with the periodicity of a_0 , the incident light is scattered/diffracted by the array. The produced evanescent wave that is resulted from propagating SPPs can tunnel through the apertures that further leads to a finite wave amplitude on the far end of the array. Here again the evanescent waves are scattered/diffracted. They can interfere at some points and consequently produce a light that can propagate away from the structure. The transmitted light can be more than twice as big of the incident light and is called extraordinary optical transmission (EOT). This means that propagating SPPs along both interfaces contribute in out coupling of the light. The in-plane wave vector of the incident light can be efficiently coupled to the SPPs along the metal/air interface. The peak location of the transmitted light, λ_{max} , can be approximately estimated by [47]:

$$\lambda_{max}\sqrt{i^2 + j^2} \cong a_0 \sqrt{\frac{\epsilon_m \epsilon_d}{\epsilon_m + \epsilon_d}} \quad (2.42)$$

Where i and j are scattering orders from the array, ε_m is the frequency-dependent permittivity of the metal and ε_d is the permittivity of the dielectric. This is called Bragg relation. By tuning the Bragg resonance of the array to the third harmonic wavelength, the THG signal can be propagated away from the sample. Fig. 2.11 shows the schematic diagram of the phase-matching of light to SPPs with a grating. As mentioned earlier, this is another way to increase the momentum of the incident photons. The in-plane wave vector of the incident light at an angle of θ on a grating with a periodicity of a in the direction of the polarization can be derived from:

$$k_{\parallel} = \beta = k \sin \theta \pm v \frac{2\pi}{a} \quad (2.43)$$

Where k is the free-space wave vector and v is an integer number.

We used this effect to efficiently out-couple the third harmonic signal toward the far field detector. Details will be discussed later in Chapter 5.

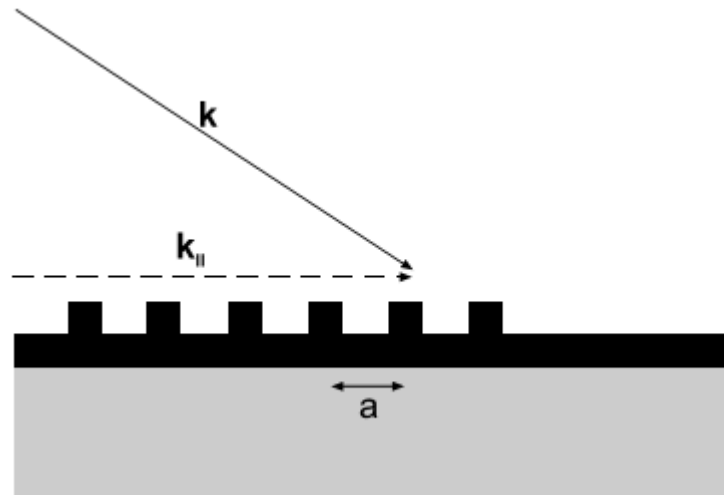


Figure 2.11 The schematic diagram of the phase-matching of light to SPPs by using a grating. Reprinted with permission from [49].

2.4 Quantum Corrected Model

In this section first the principle of the electron tunneling through a rectangular barrier is discussed. The efficiency of classical electromagnetic theory, quantum model, and quantum-corrected model in predicting the linear optical response of some plasmonics structures will be reviewed. The detail of utilizing QCM for predicting THG in very small gap regions will be discussed in detail in Chapter 6.

2.4.1 Quantum Electron Tunneling Through a Finite Rectangular Potential Barrier [54].

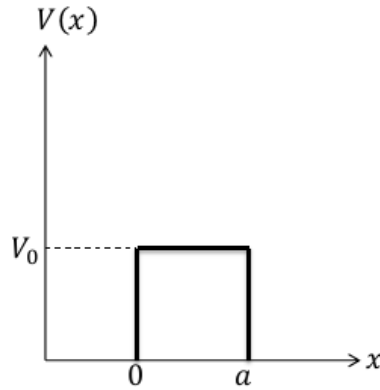


Figure 2.12 Illustration of a finite rectangular potential barrier

Here, the theory of electron tunneling through a finite rectangular barrier (Fig. 2.12) is discussed. The potential barrier is defined as:

$$V(x) = \begin{cases} V_0, & \text{for } 0 < x < a \\ 0, & \text{for } x < 0, x > a \end{cases} \quad (2.44)$$

Where V_0 is a positive constant. Time independent Schrödinger wave equation can be used to estimate the transmission and reflection probability of the electrons once they arrive to the potential barrier:

$$-\frac{\hbar^2}{2m} \nabla^2 \Psi + V\Psi = E\Psi \quad (2.45)$$

Where \hbar is the reduced Planck constant, m is the effective mass of the electron, Ψ is electron wave function, V is the potential and E is the energy. The wave equation can be modified for the one-dimensional case in the x direction:

$$-\frac{\hbar^2}{2m} \frac{d^2\Psi(x)}{dx^2} + V(x)\Psi(x) = E\Psi(x) \quad (2.46)$$

Considering the boundary conditions at $x = 0$ and $x = a$, the solution to the Schrödinger equation in each of three regions can be written as:

$$\Psi_L(x) = A_r e^{ik_0x} + A_l e^{-ik_0x} \quad x < 0 \quad (2.47)$$

$$\Psi_C(x) = B_r e^{ik_1x} + B_l e^{-ik_1x} \quad 0 < x < a \quad (2.48)$$

$$\Psi_R(x) = C_r e^{ik_0x} + C_l e^{-ik_0x} \quad x > a \quad (2.49)$$

where k_0 and k_1 are the wave numbers in the corresponding regions and can be obtained from:

$$k_0 = \sqrt{2mE/\hbar^2} \quad x < 0 \text{ or } x > a \quad (2.50)$$

$$k_1 = \sqrt{2m(E - V_0)/\hbar^2} \quad 0 < x < a \quad (2.51)$$

The indices r and l represents the direction of wave velocity vector and stands for right and left. L , C , and R denote the left, center and right region in the finite rectangular model. The coefficients A , B and C can be derived from boundary conditions considering the continuity of the wave function and its derivative:

$$\Psi_L(0) = \Psi_C(0) \quad (2.52)$$

$$\frac{d}{dx} \Psi_L(0) = \frac{d}{dx} \Psi_C(0) \quad (2.53)$$

$$\Psi_C(a) = \Psi_R(a) \quad (2.54)$$

$$\frac{d}{dx} \Psi_C(a) = \frac{d}{dx} \Psi_R(a) \quad (2.55)$$

Applying these boundary conditions to the wave functions in the regions results in:

$$A_r + A_l = B_r + B_l \quad (2.56)$$

$$ik_0(A_r - A_l) = ik_1(B_r - B_l) \quad (2.57)$$

$$B_r e^{iak_1} + B_l e^{-iak_1} = C_r e^{iak_0} + C_l e^{-iak_0} \quad (2.58)$$

$$ik_1(B_r e^{iak_1} - B_l e^{-iak_1}) = ik_0(C_r e^{iak_0} - C_l e^{-iak_0}) \quad (2.59)$$

A classical particle with energy $E > V_0$ can always surpass the barrier potential whereas a particle with energy $E < V_0$ is reflected. In the quantum case, however, the particle may be reflected or transmitted. At this point, one can suppose that there is an incident field from left to right in the left region incident on the barrier region in the center. It is assumed that there is no such a wave from right to left in the right region. So the coefficients can be represented by:

$$A_r = 1 \text{ (incoming particle)} \quad (2.60)$$

$$A_l = r \text{ (reflection)} \quad (2.61)$$

$$C_l = 0 \text{ (no incoming particle from the right in the right region)} \quad (2.62)$$

$$C_r = t \text{ (transmission)} \quad (2.63)$$

We can eliminate B_l and B_r from the equation. The transmission and reflection can be derived from:

$$t = \frac{4k_0 k_1 e^{-ia(k_0 - k_1)}}{(k_0 + k_1)^2 - e^{2iak_1}(k_0 - k_1)^2} \quad (2.64)$$

$$r = \frac{(k_0^2 - k_1^2) \sin(ak_1)}{2ik_0 k_1 \cos(ak_1) + (k_0^2 + k_1^2) \sin(ak_1)} \quad (2.65)$$

The problem can be solved for three different conditions: $E < V_0$, $E > V_0$ and $E = V_0$

$$T = |t|^2 = \frac{1}{1 + \frac{V_0^2 \sinh^2(k_1 a)}{4E(V_0 - E)}} \quad E < V_0 \quad (2.66)$$

$$T = |t|^2 = \frac{1}{1 + \frac{V_0^2 \sin^2(k_1 a)}{4E(E - V_0)}} \quad E > V_0 \quad (2.67)$$

If $E = V_0$ the solution to the electron wave function is not exponential anymore:

$$\Psi_C(x) = B_1 + B_2 x \quad 0 < x < a \quad (2.68)$$

Where B_1 and B_2 can be found by applying the boundary conditions at $x = 0$ and $x = a$. Fig. 2.13 shows transmission coefficient as a function of energy.

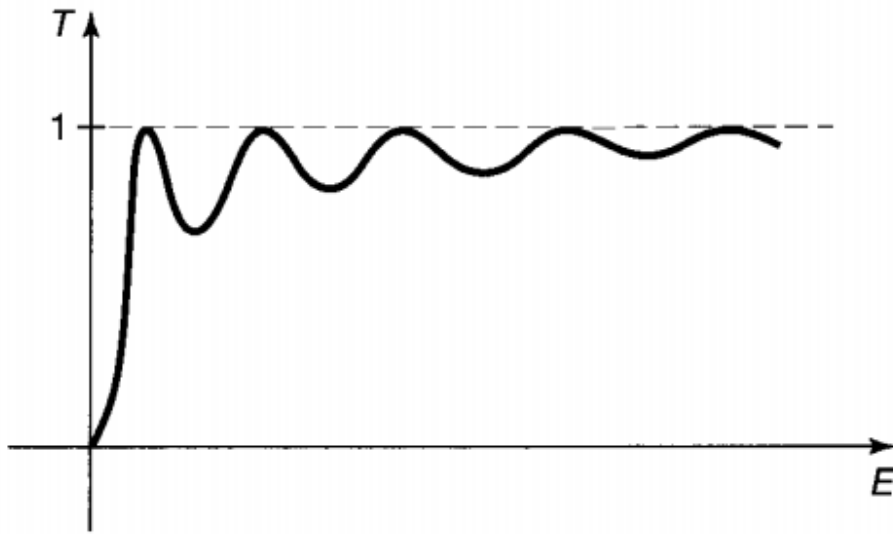


Figure 2.13 Transmission coefficient as a function of energy. Reprinted with permission from Ref. [54]

2.4.2 Characterization of Computational Models on the Onset of Electron Tunneling

The quantum-corrected model (QCM) has been developed to study the quantum tunneling effects in the plasmonics gap structures. Previously, this model, successfully, has been used to estimate the confined electric field in the gap between two metal spheres and also the tip of bowtie nanoantennas. On the onset of electron tunneling, the field

inside the gap region is quenched. However, this electric field suppression cannot be estimated by the classical electromagnetic models (CEM).

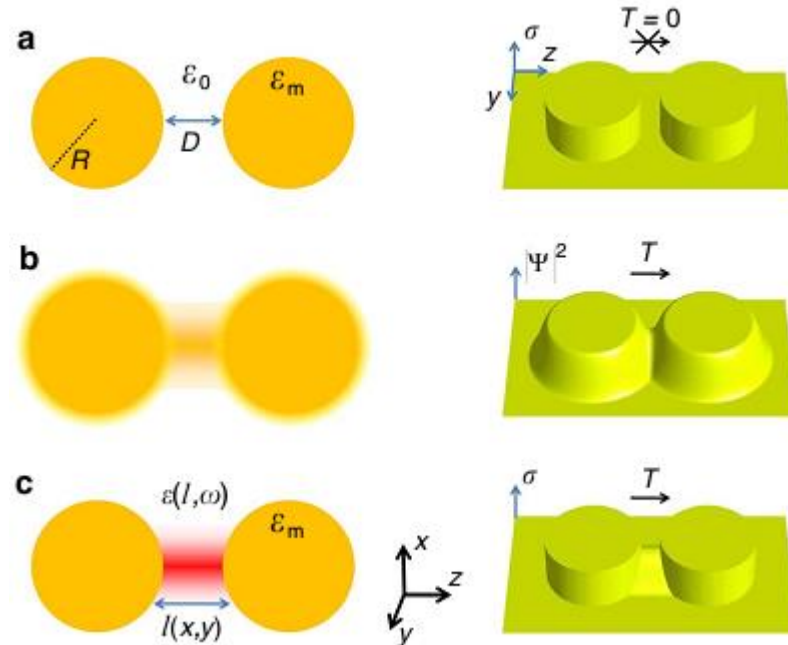


Figure 2.14 The description of the nanoparticle dimer behavior using different theoretical treatments: a) CEM: The conductivity between the nanoparticles is zero, and therefore the electron tunneling probability is zero, and no electron can transfer between the particles ($T=0$). b) QM: The electron tunneling probability is greater than zero ($T>0$) and the electron density distribution of the electrons, $|\Psi|^2$, cannot be changed abruptly. c) QCM: The material in the junction is modeled by a virtual dielectric medium that is represented by $\epsilon(l(x,y), \omega)$. Reprinted with permission from Ref. [90].

Fig. 2.14 shows the idea behind the QCM for the case of two metallic spheres of radius R and spacing of D . vacuum surrounds them with the permittivity of ϵ_0 . In CEM, for large gaps, the probability of the electron tunneling, T , is zero. However, in the fully quantum model (QM) the probability does not change abruptly. The density of the electrons between two metal spheres varies continuously and can be significant at the center of the gap. This is due the overlap of two evanescent waves of the conduction electrons evolved from the surface of the metal spheres in the gap region. The possibility

of electron tunneling between two spheres increases as the gap distance decreases. In the QCM approximation the gap between two nano-spheres can be modeled by a gap-size dependent fictitious material. The permittivity of the gap region as a function of gap size and the angular frequency of the confined electric field, $\varepsilon(l, \omega)$, can be derived from (in atomic units) [90]:

$$\sigma(l, \omega) = -i \frac{\omega}{4\pi} (\varepsilon(l, \omega) - 1) \quad (2.69)$$

Modifying Drude model Eq. 2.3 for the permittivity of the gap region between to metallic objects leads to:

$$\varepsilon(l, \omega) = \varepsilon_\infty - \frac{\omega_p^2}{\omega(\omega + i\gamma_p(l))} \quad (2.70)$$

The plasma frequency of the gap region, ω_g , and the screening contribution, ε_∞ , are assumed to be equal to the surrounding medium values ($\omega_g = \omega_p$; $\varepsilon_\infty = 1$). Moreover, the electron collision frequency of the gap region can be obtained by using the static conductivity $\sigma_0(l) = \sigma(l, \omega \rightarrow 0)$, the main result of the QCM is represented by:

$$\gamma(l) = \frac{\omega_g^2}{4\pi\sigma_0(l)} \quad (2.71)$$

The dc conductivity, $\sigma_0(l)$, at the junction under bias $U = lE$ can be represented by:

$$\sigma_0(l) = l \frac{dJ}{dU} = l \frac{2}{(2\pi)^2} \int_0^{\Omega_F} T(\Omega, l) d\Omega \quad (2.72)$$

Where $T(\Omega, l)$ is the electron tunneling probability as a function of the gap separation l and the energy Ω , Ω_F is the Fermi energy level. Electrons at this energy level will dominate the tunneling current through the potential barrier.

Here the collision frequency of the conducting electrons in the gap region is taken as a function of the gap size. The confined electric field in the gap between two gold nanospheres and a bowtie structure has been estimated by using this approach. The results show that the field at the onset of the tunneling has been quenched. This electric field suppression is not predictable by using the CEM. The plasma frequency of the gap region can also be expressed as a function of the gap separation(l) [90]:

$$\omega_g = \sqrt{T(l, \Omega_F)} \omega_p \quad (2.73)$$

Where $T(l, \Omega_F)$ is the energy Ω -dependent electron tunnelling probability at each lateral position within the gap with separation, l , and Ω_F is the Fermi energy.

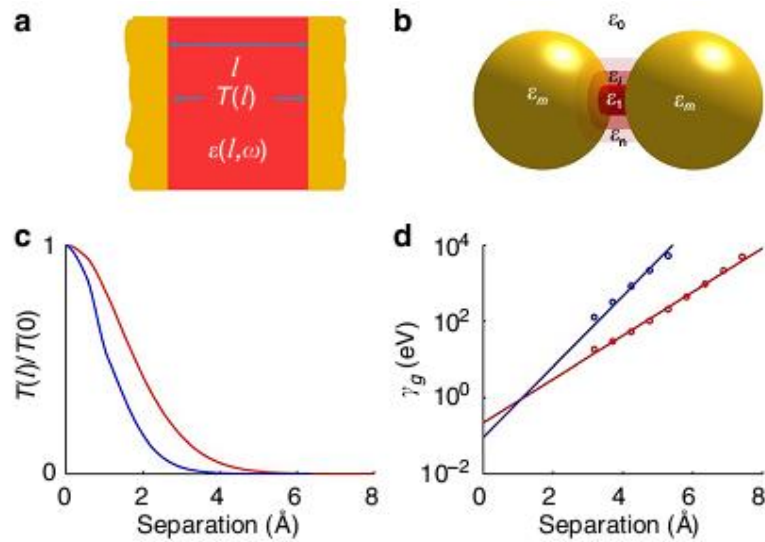


Figure 2.15 Illustration of the parameters involved in the QCM: a) a simple flat plasmonic configuration b) The inhomogeneous local dielectric constant distribution in the QCM of the metallic dimer. c) Normalized electron tunneling transmission d) Electron collision frequency in the gap region as a function of the gap size. The blue curves show the results for gold jellium and the red curves are related to Na jellium. Reprinted with permission from Ref. [90].

Fig. 2.15 shows the illustration of the parameters involved in the QCM. The robustness of the calculated field results in the gap region considering the fixed plasma frequency ($\omega_g = \omega_p$) or by using Eq. 2.73 has been also verified [90].

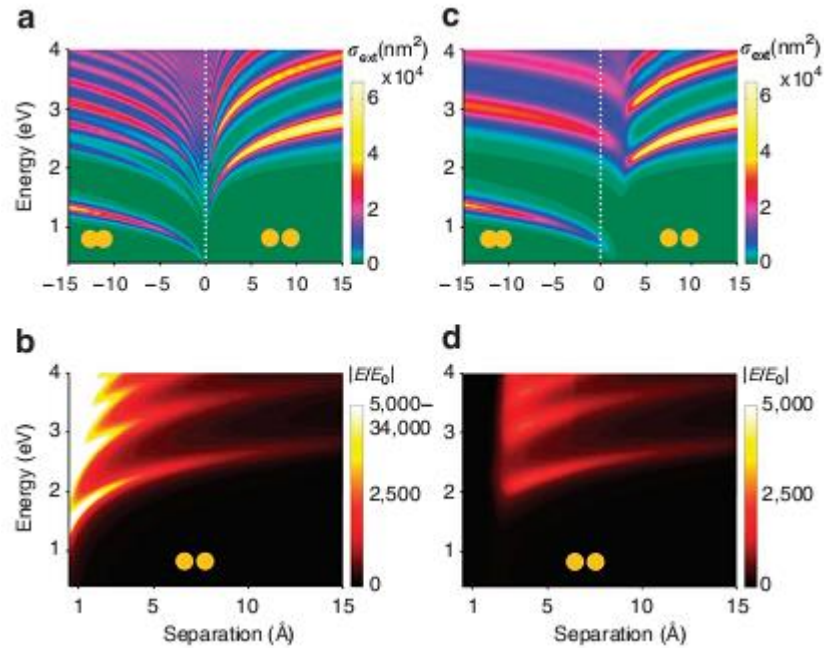


Figure 2.16 Simulation results of near-field energy for large plasmonic dimers for different separations using CEM (a, b) and QCM(c, d). Reprinted with permission from Ref. [90]

Figs. 2.16 and 2.17 show the near electric field enhancement in the gap between the plasmonic dimer and the bowtie antenna. The suppressed electric can obviously be seen in the QCM results on the very small separation regime whereas the CEM fails to predict it.

In our approach, we used equation 2.72 and took the collision frequency (scattering rate) of the gap region fixed and same as the metal. This is related to the very famous debate of Josephson and Bardeen in 1962 on the existence of a superconducting state in a very small gap region between metals [88]. We used the modified model to study the

THG on the onset of quantum tunneling in the sub-nanometer gap region. The details of this approach will be discussed in Chapter 6.

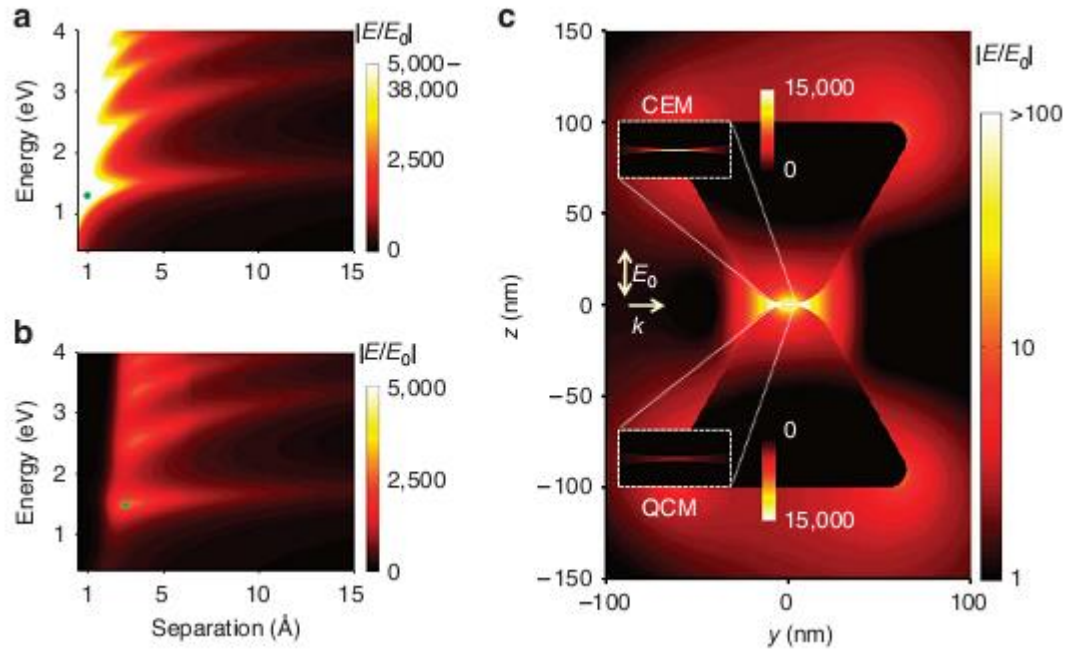


Figure 2.17 Simulation results of the near-field energy confined in the gap of the bowtie antenna (d) for different separations using CEM (a) and QCM(b). Reprinted with permission from Ref. [90].

2.5 Nonlinear Scattering Theory

Nonlinear scattering theory is a computational method for estimating the THG of the metasurfaces. It has been successfully used in predicting the SHG from an array of U-shaped structures [67]. Since the model has been extensively used in this project, it will be discussed in more detail in Chapter 5.

2.6 Summary

In this chapter, previous studies in the nonlinear optical response of aperture-based plasmonic structures were reviewed. The principles of harmonic generation and plasmonics were also discussed. Using effective index method, the theory behind the

transmission of light through a single rectangular aperture and its relation to the LSP resonance and cut-off wavelength were explained. The effect of the phase matching of incident light to SPPs by adjusting the periodicity of a grating and its influence on the extraordinary optical transmission were also described. The QCM model also was introduced, and its efficiency in predicting the linear optical response of metasurfaces was compared to other models such as CEM and QM.

Chapter 3 : Experimental Methods

3.1 Introduction

This chapter presents the methods used for device fabrication and characterization. This chapter includes a review of common fabrication methods such as focused ion beam (FIB) and electron beam lithography (EBL). Later on, more complex fabrication methods such as atomic layer lithography, and template stripping that lead to sub-10 nm structures is discussed. Finally, the scanning electron microscopy (SEM) as an efficient tool for device characterization is presented.

3.2 Fabrication Methods

3.2.1 Focused Ion Beam Milling

The basic FIB system consists of a vacuum system and chamber, liquid metal ion source, sample stage, detectors and a computer to run and control the system. The configuration and the principles of operation of the FIB are very similar to the SEM, except rather than a beam of electrons, FIB systems use a highly focused beam of ions. The principles of operation of the SEM is discussed later in this chapter.

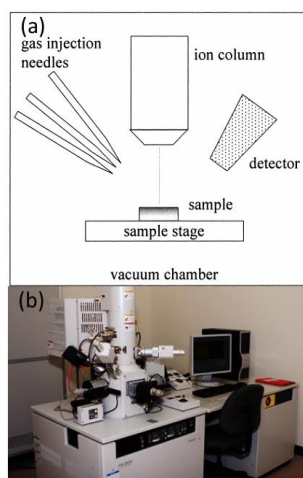


Figure 3.1 a) Schematic diagram of the FIB machine [55] b) Hitachi FB2100 FIB at the University of Victoria [60]. Reprinted with permission from corresponding References.

Fig. 3.1.a shows the schematic diagram of the FIB device. Fig. 3.1.b shows the Hitachi FB2100 FIB at the University of Victoria. The specification of this device is summarized in Table 3.1.

Table 3.1 Specification of the Hitachi FB2100 FIB [60]

Resolution	6 nm or better at 40 kV
Ion Source	Liquid gallium metal ion source
Accelerating Voltage	10 to 40 kV
Maximum Current	40 nA at 40 kV
Stages	Actuated TEM and SEM holder stages
Probe	Actuated pick/place probe
Deposition System	Tungsten deposition system
Specimen Diameter	100 mm

3.2.2 Electron Beam Lithography

Electron beam lithography is one of the most important methods in nanofabrication. A thin film of resist uniformly covers the surface of the sample. Normally, a spin coater is used for this purpose. The thickness of the resist layer can be controlled by the number of revolutions. Other parameters such as viscosity and concentration of the resist should also be considered. A highly focused electron beam exposure is used to modify the solubility of a resist on the sample under fabrication. The process is followed by a subsequent development step for etching. Fig. 3.2 shows the process of EBL.

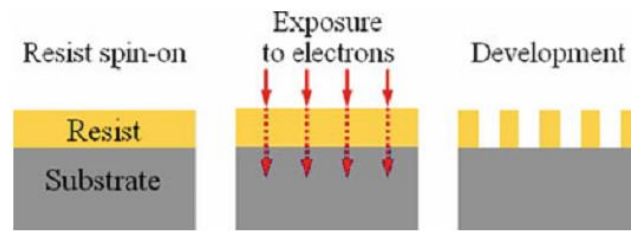


Figure 3.2 Schematic diagram of the process of EBL. Reprinted with permission from Ref. [56]

Fig. 3.3.a shows the schematic diagram of the electron exposure system. Fig. 3.3.b shows a commercial EBL system. The first EBL system emerged from an SEM imaging tool that was developed by a beam blaster and a pattern generator. Using these extra tools the area of the exposure with electron beam could be defined. However, modern EBL systems are solely used for patterning purposes. In these advanced machines, high brightness electron sources are used that allows faster throughput fabrication with high resolution.

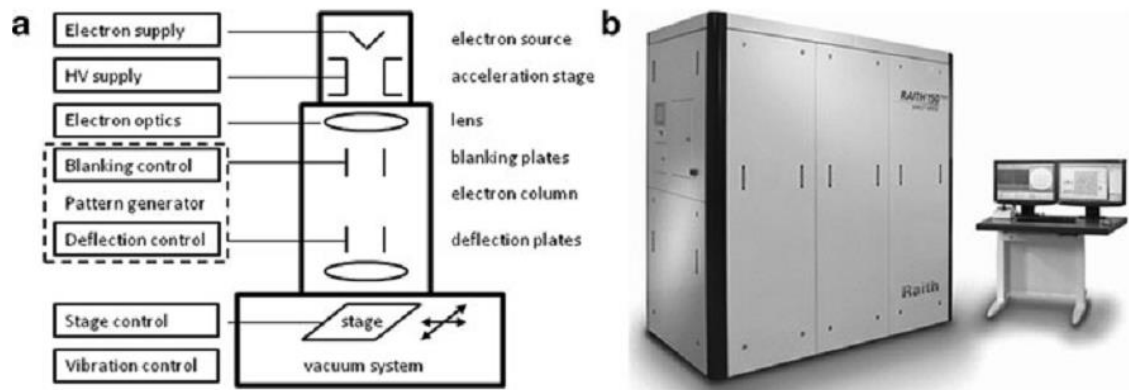


Figure 3.3 a) Schematic diagram of the electron exposure system b) A commercial EBL system. Reprinted with permission from Ref. [56]

The primary goal of EBL is arbitrarily patterning of the resist with high resolution, high sensitivity, and high reliability. These are related to the factors such as the quality of the focused electron beam, the resist type, electron beam energy and dose, and

development time and temperature. Table 3.2 shows the parameters affecting the EBL process.

Table 3.2 The influence of different parameters on EBL process. Reprinted with permission from Ref. [56]

Parameter	Process impact
Exposure energy	Resolution, sensitivity, proximity
Exposure dose	Pattern quality
Pattern density	Proximity, pattern quality
Resist material	Sensitivity, resolution, contrast
Resist thickness	Sensitivity, resolution, pattern quality
Developer	Sensitivity, resolution, development window
Development temperature	Sensitivity, resolution, exposure window
Development time	Sensitivity, resolution, exposure window

3.2.3 Fabrication of Nanogaps by Atomic Layer Deposition and Lithography

This section explains the atomic layer deposition (ALD) and lithography as a high throughput tool for fabrication of an array of annular ring apertures. Using EBL, an array of circular holes is fabricated on a 150 nm gold film on a Pyrex glass substrate utilizing negative resist (NR71-1500P) and photolithography. After cleaning the surface with acetone, methanol, and IPA and drying with N₂ gas, a thin layer of Al₂O₃ is deposited on the patterned surface of the metal at 250° C. The thickness of deposited Al₂O₃ is controlled by using ellipsometer on a silicon wafer that is placed in the same chamber. Trenches are filled with gold after evaporation. Using an adhesive tape, the excess metal which is deposited on the surface can be easily removed. The final step in the process is anisotropic ion milling that is carried out by Ar beam incident at 10° angle for polishing the surface or plane planarization [57]. Figs. 3.4.a and b show the different steps in the process of atomic layer lithography method for fabrication of the annular ring arrays. Fig.

3.4.c-e shows SEM images of the sample after each step in atomic layer lithography process.

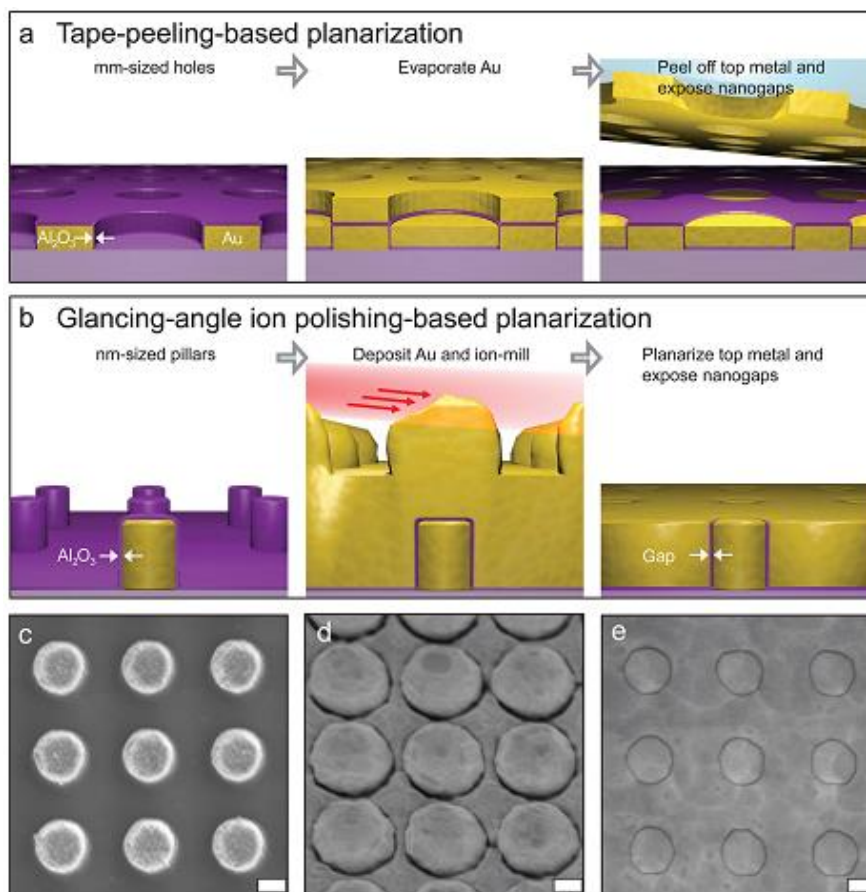


Figure 3.4 a) Schematic diagram of the tape-peeling nanogap fabrication. b) Glancing-angle ion polishing process. c) SEM image of the patterned gold pillars array on a sapphire wafer, a very thin layer of Al_2O_3 is deposited on the surface of the sample by using ALD. d) SEM image of the sample after deposition of the second layer of gold. e) SEM image of the sample after glancing –angle ion polishing. The scale bars in e-d are 150 nm. Reprinted with permission from Ref. [57]

3.2.4 Template Stripping

The process of template stripping method is depicted in Fig. 3.5. Ultra flat metal surface can be achieved by using this method [58]. It can also be used as a high-

throughput approach to make apertures with the gap size smaller than 10 nm. Recently, this method was used to fabricate double nanohole (DNH) optical tweezers with the gap size smaller than 10 nm [85].

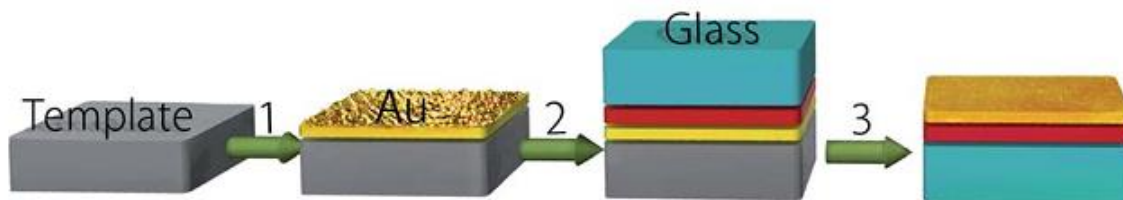


Figure 3.5 Schematic diagram of the template stripping process: A gold thin film is evaporated on a flat template. A mechanical support is glued to the surface of the gold and then cleaved at the weakest adhesion point. The outcome of the process is a flat gold surface which its roughness is comparable to the template surface. Reprinted with permission from Ref. [58].

Fig. 3.6 shows the fabrication process to yield DNH with sub-10 nm gap sizes. First, FIB is used to fabricate DNH structures on the silicon samples to make the required templates. This milling must be done for enough depth to make sure that the deposited gold on the surface of the silicon sample is not connected to the gold inside the DNH structures. Using the FIB current of 0.019 nA, 80 \times magnification, 10 μ s dwell time, and 17 ion beam passes assure that the depth is suitable. In the next step, gold is deposited on the surface of the silicon templates. A very thin layer of UV epoxy is sandwiched between a glass slide and the surface of the gold-deposited-silicon templates.

This thin layer provides an adhesion layer between the glass slide and the deposited gold on the silicon surface. Due to the weaker bonding of the gold to the silicon, the gold layer can be stripped off from the silicon easily.

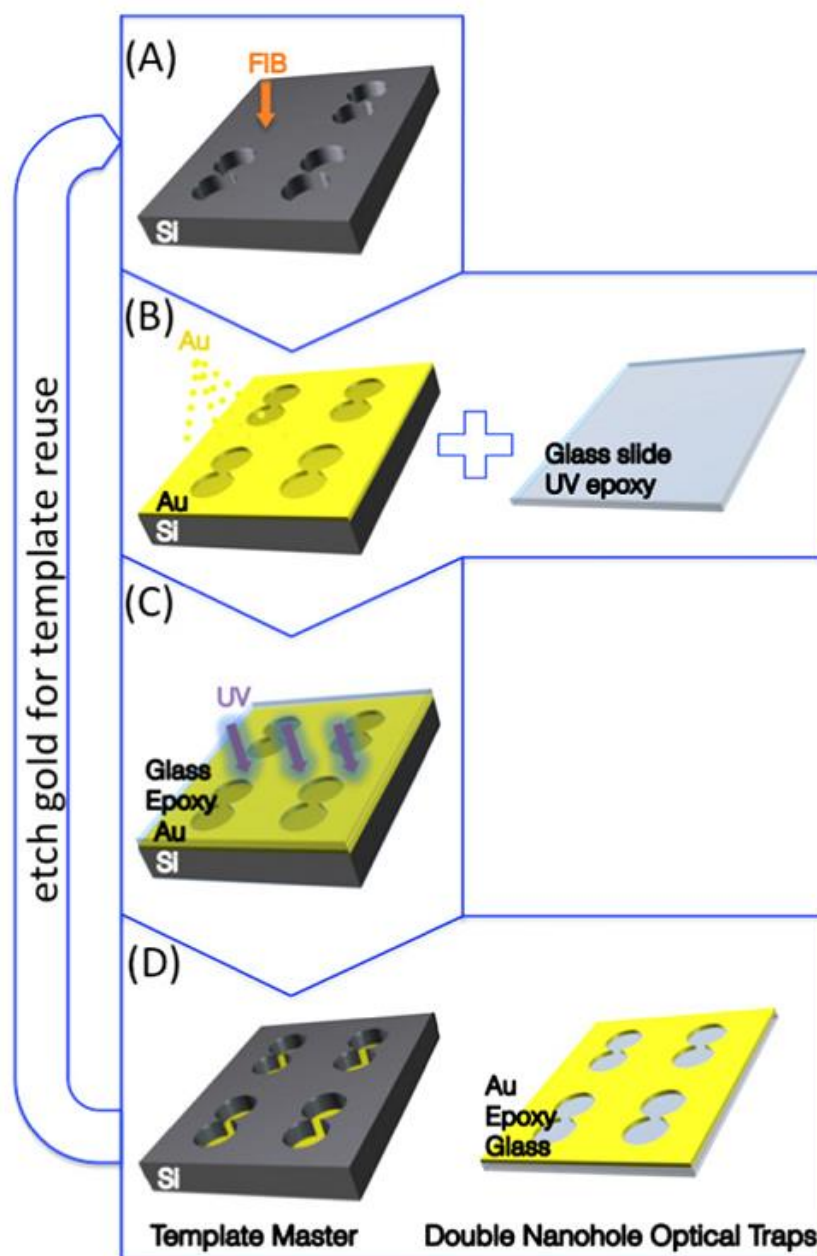


Figure 3.6 Schematic diagram of the template stripping process flow a) the structure is milled on the silicon templates. b) The desired thickness of gold is deposited on the surface of the silicon template. (The deposited gold thickness must be less than the depth of the milled structure to avoid connection of the gold on the surface to the gold that fills the structure). A glass slide is attached to the surface of the sample by using UV epoxy c) UV exposure d) the DNH structures transferred to the glass slide after stripping. The silicon masters are reusable. Reprinted with permission from Ref. [85].

Fig. 3.7.a shows the fabricated DNH structure on a silicon template. The resulted template-stripped structures are shown in Figs. 3.7.b-d. Some examples of our fabricated aperture arrays using template-stripping method are provided in Appendix C.

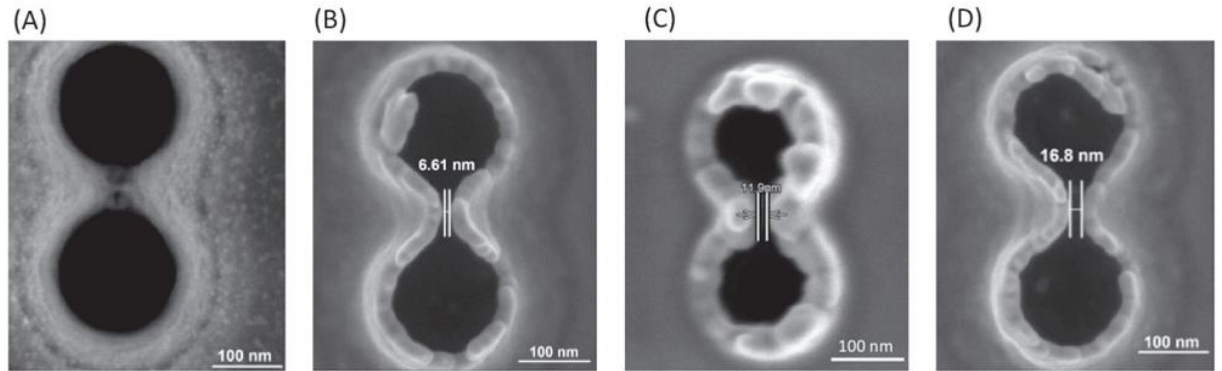


Figure 3.7 a) Fabricated silicon template master. b) Template-stripped DNH with a gap of ~ 7 nm using the template shown in (a) c) Template-stripped DNH with a gap of ~ 12 nm. d) Template-stripped DNH with a gap of ~ 17 nm. Reprinted with permission from Ref. [85].

3.3 Characterization Methods

In this research, scanning electron microscopy was used extensively to characterize the fabricated structures. This section reviews the principle of the SEM. Moreover, the specification of Hitachi S-4800 FESEM machine is provided

3.3.1 Scanning Electron Microscopy

Electron microscopes are normally used to resolve objects smaller than $1 \mu\text{m}$ that optical microscope failed to handle. In particular, SEM is used to observe the structure of the surface of a specimen. Fig. 3.8 depicts the resolving power of the human eye as compared to an optical microscope and an electron microscope. Due to greater focal depth comparing to optical microscopes, the stereoscopic imaging is also possible with electron microscopy. Many SEMs have an x-ray analyzer for compositional analysis of the desired region.

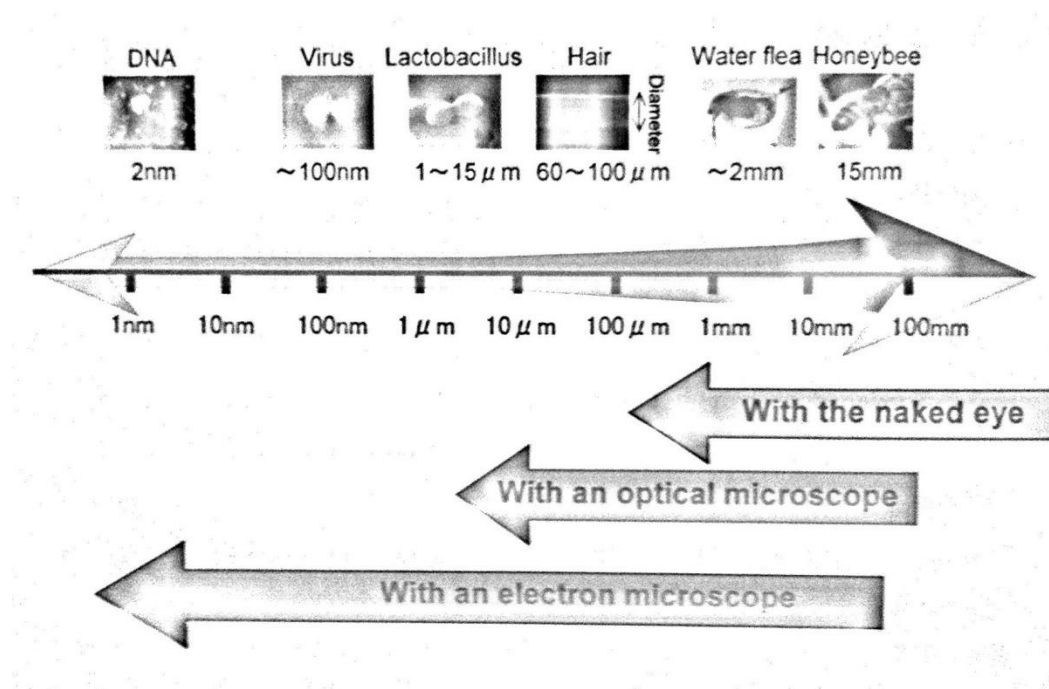


Figure 3.8 The resolving power of the human eye, optical microscope and electron microscope [59].

An SEM rasters the surface of the specimen with a focused electron beam in vacuum. The scattering of electrons by the surface can be detected, and converted into an image. Fig. 3.9 shows the principles of SEM. As a result of the incident electron beam's interaction with the surface of the specimen, secondary electrons, backscattered electrons, characteristic x-rays and other signals are generated. To form an image, SEM uses the secondary electrons and backscattered electrons. The fine topographical image of the sample results from secondary electrons which are generated near the surface of the sample. The backscattered electrons are those electrons that are reflected upon striking the atoms of the sample under observation. The number of backscattered electrons is related to the crystallographic orientation of the specimen, the average atomic number, and other compositional parameters. Therefore detecting these electrons along with an x-

ray analyzer leads to a compositional analysis of the specimen. This way the type and percentage of the elements included in the sample can be observed.

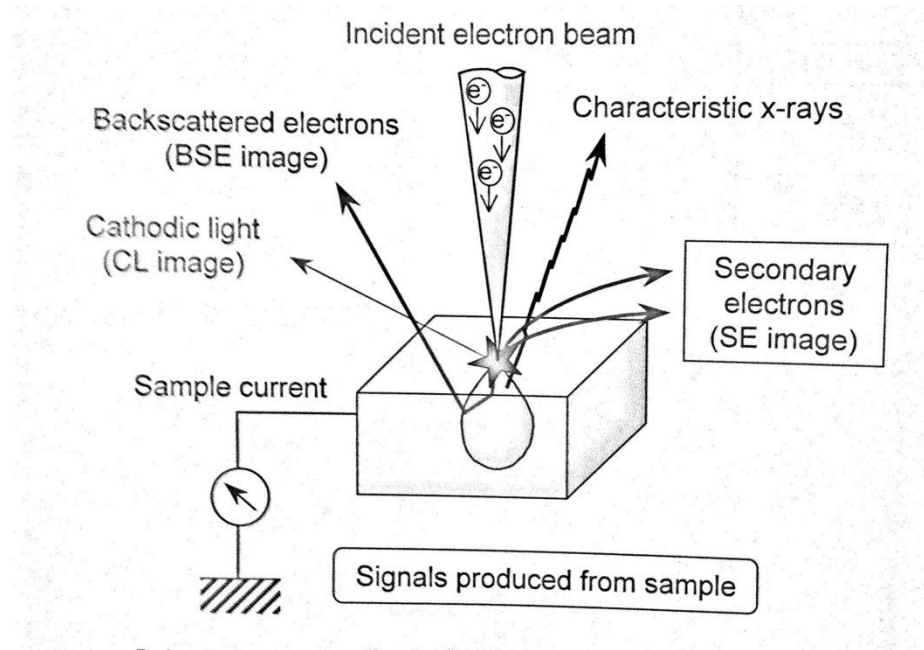


Figure 3.9 Illustration of the signals produced from the sample as a result of exposure to a focused electron beam [59].

Fig. 3.10 shows the schematic of the SEM configuration. The main parts of the device are electron gun, a condenser lens, deflection coil, an objective lens, secondary electron detector, display and vacuum pump. In this thesis, there are examples of SEM images from our works and other related works that are mainly used to evaluate the quality of fabricated structures.

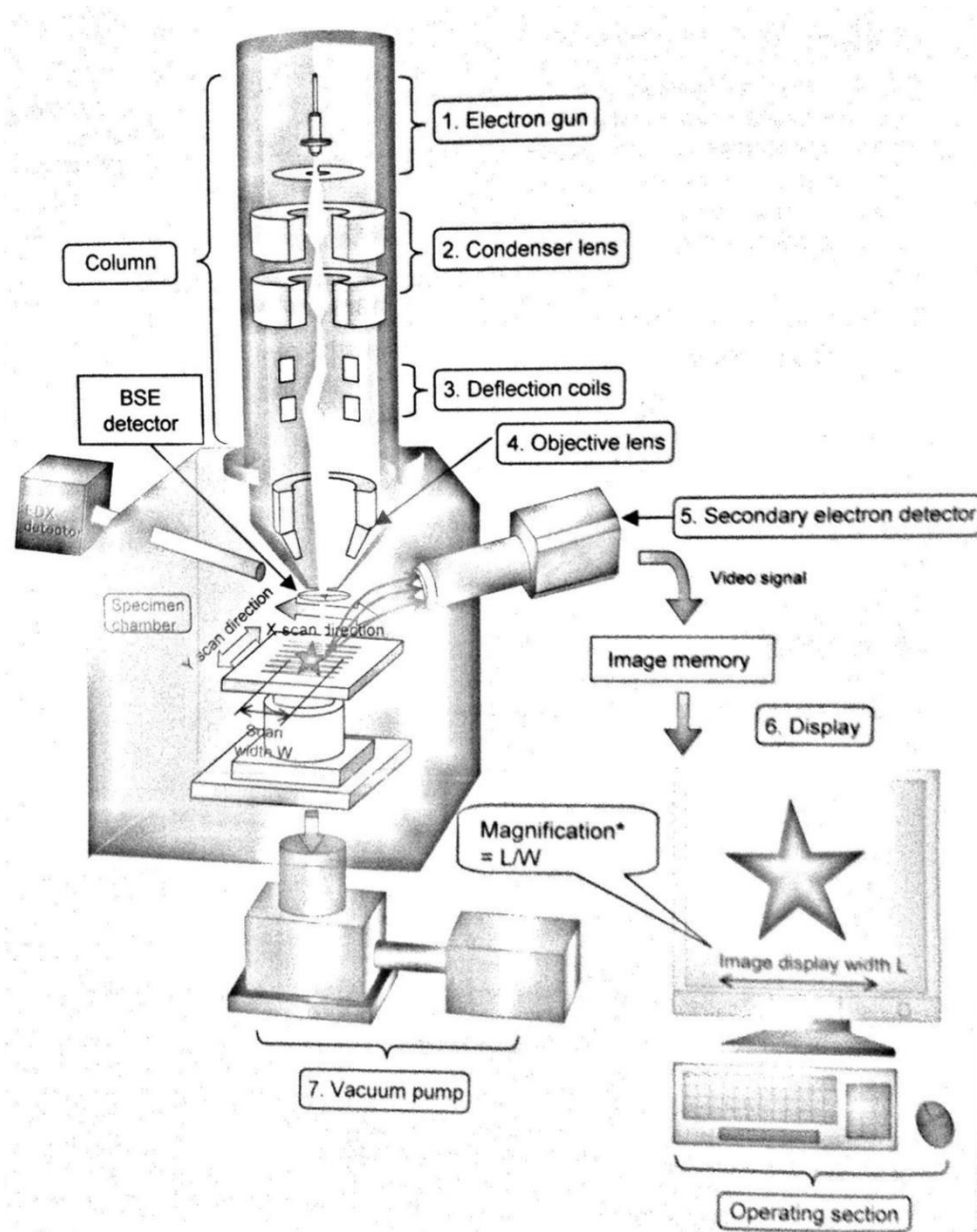


Figure 3.10 Schematic diagram of SEM configuration [59]

3.3.2 Specifications of the Hitachi S-4800 FESEM [60]

The specifications of the Hitachi S-4800 FESEM machine that was used at the advanced microscopy facility at the University of Victoria are as follows:

- 0.5 kV to 30 kV accelerating voltage
- 1 nm resolution at 15 kV, 1.4 nm at 1 kV

- Magnification from 30x to 800,000x
- Maximum specimen size = 100 mm
- Super ExB filter technology
- Dry vacuum system
- X+Y motorized eucentric stage with trackball interface (tilt and Z by manual control)
- Ring-type YAG backscatter detector
- Bruker Quantax EDS System for X-ray spectroscopy.

3.4 Summary

This chapter devoted to the experimental methods that were involved in the project. First, the conventional fabrication methods such as focused ion beam milling and electron beam lithography were explained. More complex fabrication methods such as atomic layer lithography and template stripping were discussed later. Scanning electron microscopy as an efficient tool for characterization of the fabricated structures was also presented.

Chapter 4 : Experiments on Nonlinear Optics

4.1 Introduction

This chapter represents the configurations of experimental setups for nonlinear optical response measurement of the metasurfaces. For non-aperture metasurfaces, these measurements are limited to the reflected signal whereas both transmitted and reflected signal can be measured for aperture-based metasurfaces. The main part of these experimental setups is a pulsed laser that delivers a high amount of energy to the metasurface in a small fraction of the time. This intense source stimulates the nonlinear processes that were measured by a fast response detector such as avalanche photodiodes (APD) or spectrometer. The details of the experimental setups are discussed in the following sections.

4.2 Experimental Setups in Reflection Geometry

Fig. 4.1 shows an experimental setup for SHG measurements. An inverted microscope configuration has been utilized for this experimental configuration. A Yb:KGW (Ytterbium:potassium gadolinium tungstate) femtosecond laser with a pulse duration of 140 fs and repetition rate of 100 KHz was used as the source. The incident beam is reflected by a dichroic mirror and focused on the sample by a dry microscope objective (Nikon S Plan Flour x40, 0.6 NA). In this work the fundamental beam wavelength is 1500 nm and the back-reflected third harmonic beam is at 500 nm which is collected through the same objective as the incident beam. The third harmonic signal is split into two different beams via a 70:30 cube beam splitter. One beam is directed toward a spectrograph (PI Acton SP2300 by Princeton Instruments) to measure the spectra of the third harmonic signal. The other beam is steered toward an avalanche photodiode (MPD

PDM Series by Picoquant) for nonlinear imaging. The sample can be moved precisely at the laser focus spot by using a multi-axis piezoelectric stage (Nano-Drive, Mad City Labs). The excitation power is set below $50 \mu\text{W}$ (peak intensities of $45.7 \text{ GW}/\text{cm}^3$) to prevent sample damage [61]. This setup has been used to measure the THG of the ITO assembled nanoantennas depicted on the inset of the Fig. 4.1 [61].

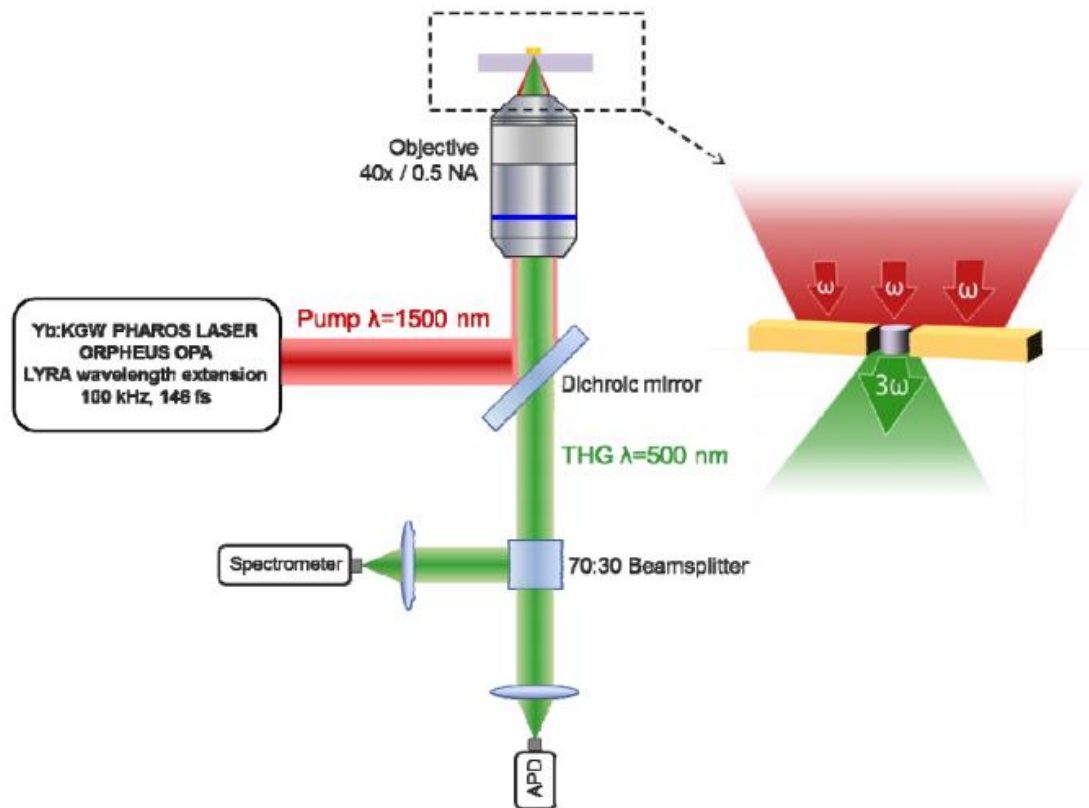


Figure 4.1 Schematic diagram of an experimental setup for SHG measurement. Reprinted with permission from Ref. [61]

Fig. 4.2.a shows the THG spectra for a single ITO nanoparticle. Fig. 4.2.b shows the THG results for the ITO-assembled plasmonic nanoantenna and Fig. 4.2.c shows the THG power as a function of the incident power. It can be seen that the THG from the hybrid structure is enhanced by six orders of magnitude [61].

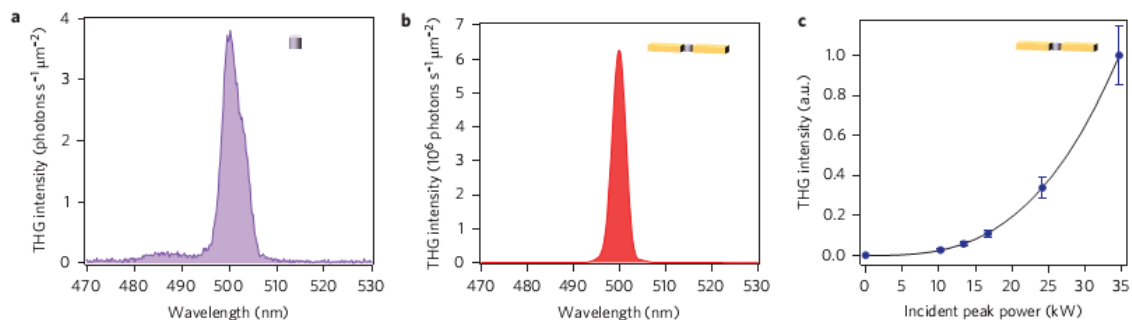


Figure 4.2 a) THG spectra for single ITO nanoparticle b) THG spectra for ITO assembled nanoantenna c) THG power dependence. Reprinted with permission from Ref. [61]

Fig. 4.3.a shows another experimental configuration in reflection geometry for THG measurements. A femtosecond pulsed laser (Mercury 1550-100-100-MOD, PolarOnyx) was used to provide the fundamental beam at the wavelength of 1570 nm and repetition rate of 38 MHz. A long pass filter is used to remove the harmonic signals before the sample. The TM polarization of the incident beam can be ensured by using a half-wave plate and polarizer in the beam path toward the sample. This beam passes through an objective lens to get focused on the sample. The beam enters the 50 \times microscope objective (0.85 NA, Melles Griot) is slightly off center, so the incident beam is not normally incident on the sample. The reflected beam also collected by the same microscope objective lens. By using a bandpass filter, the source signal is removed from the reflected beam. Eventually, the beam is steered toward the spectrometer and CCD camera. Fig. 4.3.b shows the THG measured spectra and Fig. 4.3.c shows the THG spotted on the CCD camera [95].

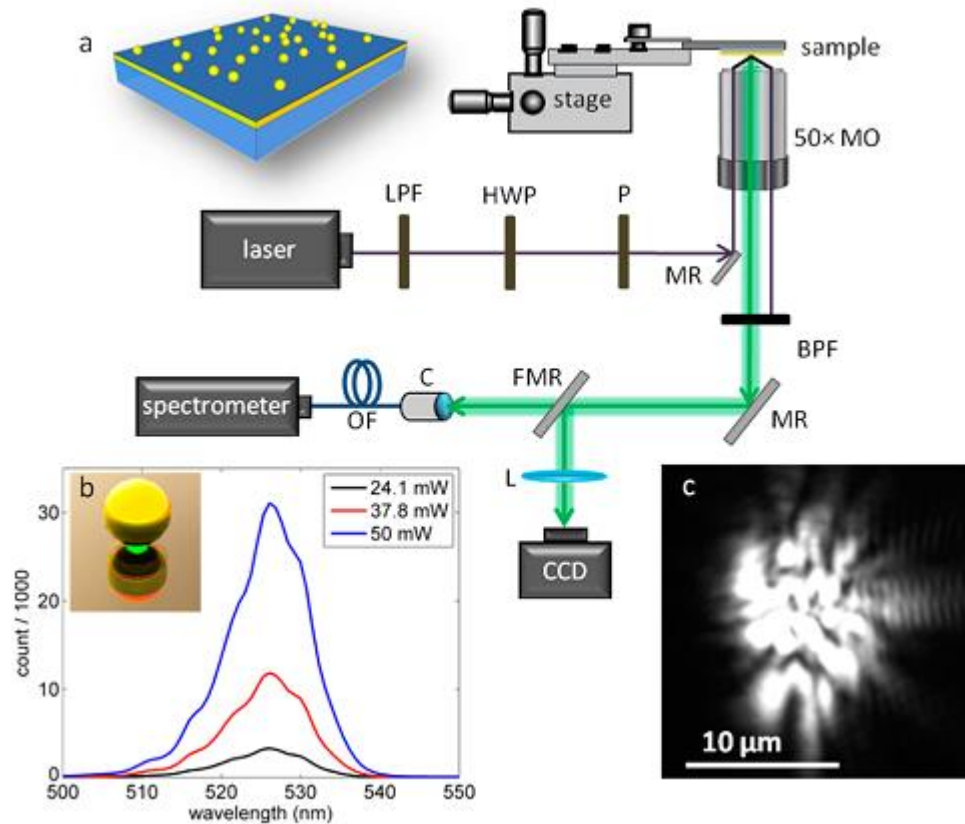


Figure 4.3 a) Schematic diagram of the experimental setup where LPF is a low pass filter, HWP is a half wave plate, P is a polarizer, MR is a mirror, FR is a flipper mirror, BPF is a bandpass filter b) The THG spectra of the nanosphere assembled thin film structure c) Observed THG on the CCD camera [95]

4.3 Experimental Setups in Transmission Geometry

Fig. 4.4.e show an experimental setup for SHG measurement of metasurfaces in transmission geometry. A femtosecond laser with the pulse (~ 170 fs pulse width, 1060 nm central wavelength, 82 MHz repetition rate, 350 mW average power) supplies the fundamental beam. The beam is modulated and weakly focused to a spot diameter of 200 μm on the sample. The direction of polarization is adjusted by using a polarizer and a half-wave plate. A visible blocking filter is used to block unwanted wavelengths before the sample. Following the sample, an IR filter removes the fundamental signal from the

SH signal. The second polarizer is used to select the polarization of the SH signal. This signal is passed through an interference filter and a photomultiplier tube that is connected to a lock-in amplifier (not shown). The modulation frequency is used as the reference signal for the lock-in amplifier [23]. Fig 4.4.d shows the SHG results for the nanostructures shown in Fig.a-c.

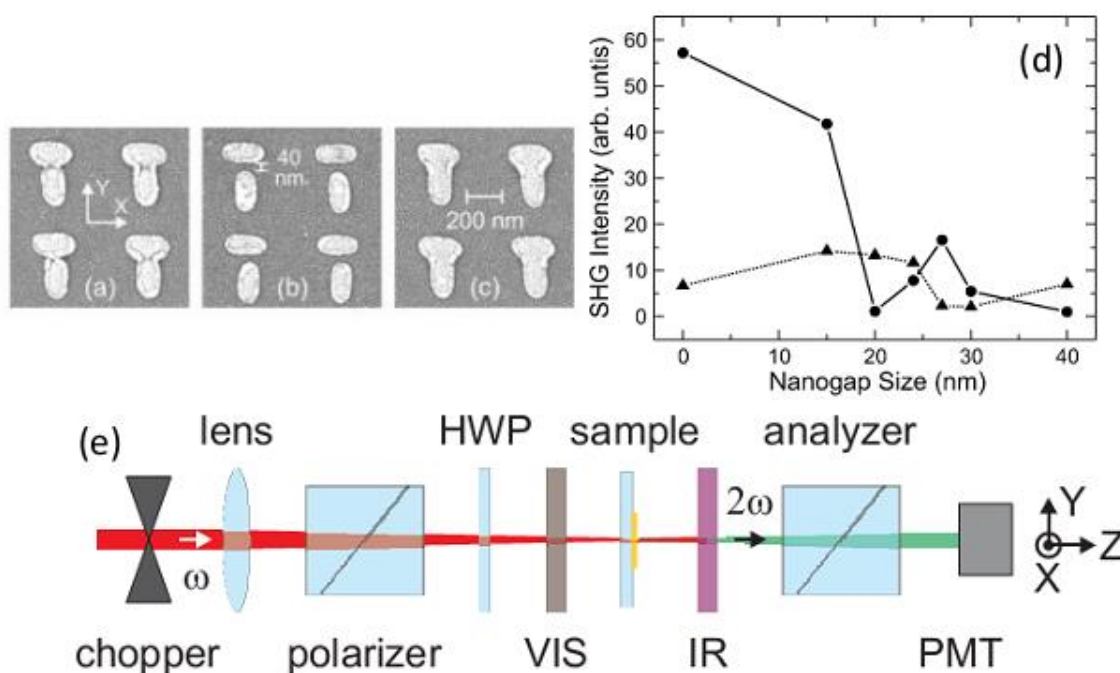


Figure 4.4 a,b,c) SEM images of the nanoantennas d) SHG as a function of the nanogap size e) The schematic diagram of the experimental setup in transmission geometry. Reprinted with permission from Ref. [23]

Fig. 4.5.a shows the schematic of another optical setup that has been used for THG measurement in transmission geometry. Fig. 4.5.b shows the normalized transmitted fundamental, SH and TH signals for different angles of incidence. From this graph, it is apparent that the peak third harmonic signal happens at the peak fundamental signal. Fig. 4.5.c shows the normalized THG signals for different periodicities of the array. Fig. 4.5.d shows the influence of the hole size on the THG [33]. Melentiev et al. [19] have studied

the effect of the material in the aperture-based THG. They have compared the THG from the single aperture in aluminum and gold film.

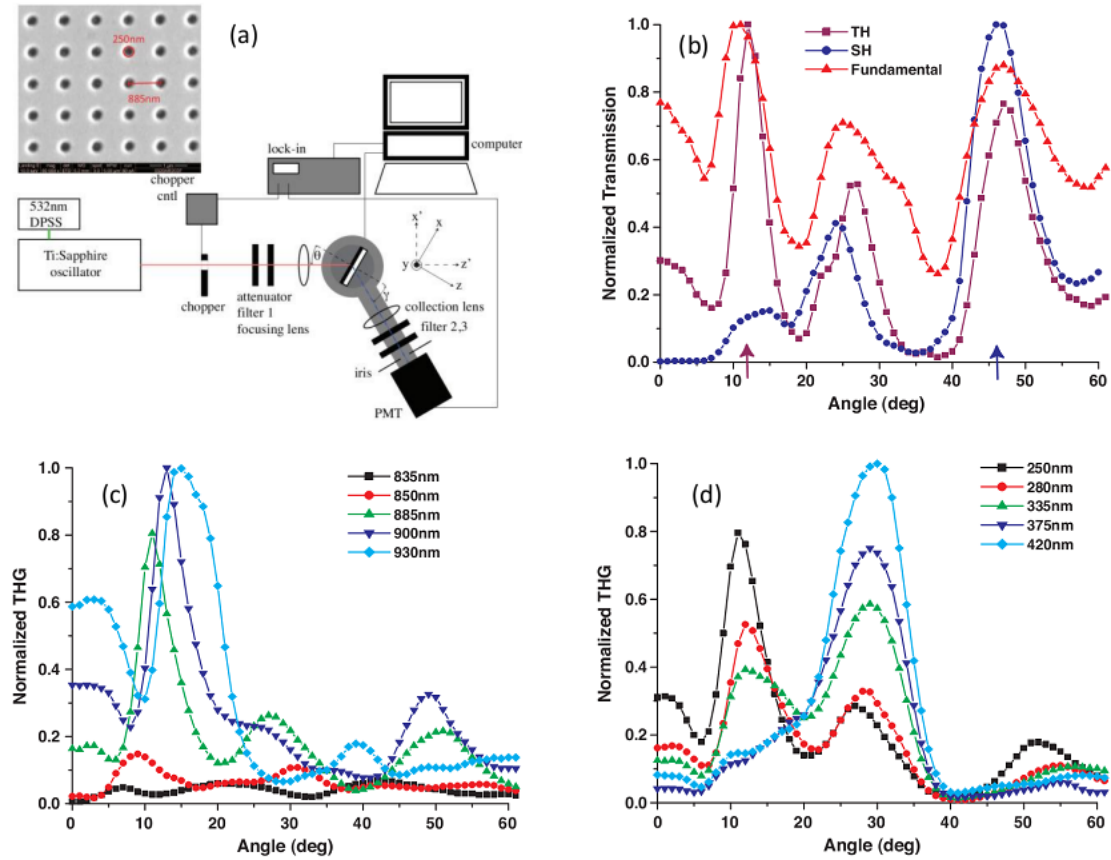


Figure 4.5 a) The schematic of the optical setup used for investigation of the effects of b) angle of incidence, c) lattice arrangement and d) the hole size on the THG. Reprinted with permission from Ref. [33]

They have found that the aluminum thin film has better performance at the fundamental wavelength of $1.56 \mu\text{m}$. The reported third order susceptibility of the aluminum in this work is 1000 times higher than gold. Fig. 4.6 shows the schematic of the optical setup used to study the THG of a single aperture. The experiments on THG of single apertures that were performed in this research is presented in Appendix 4.

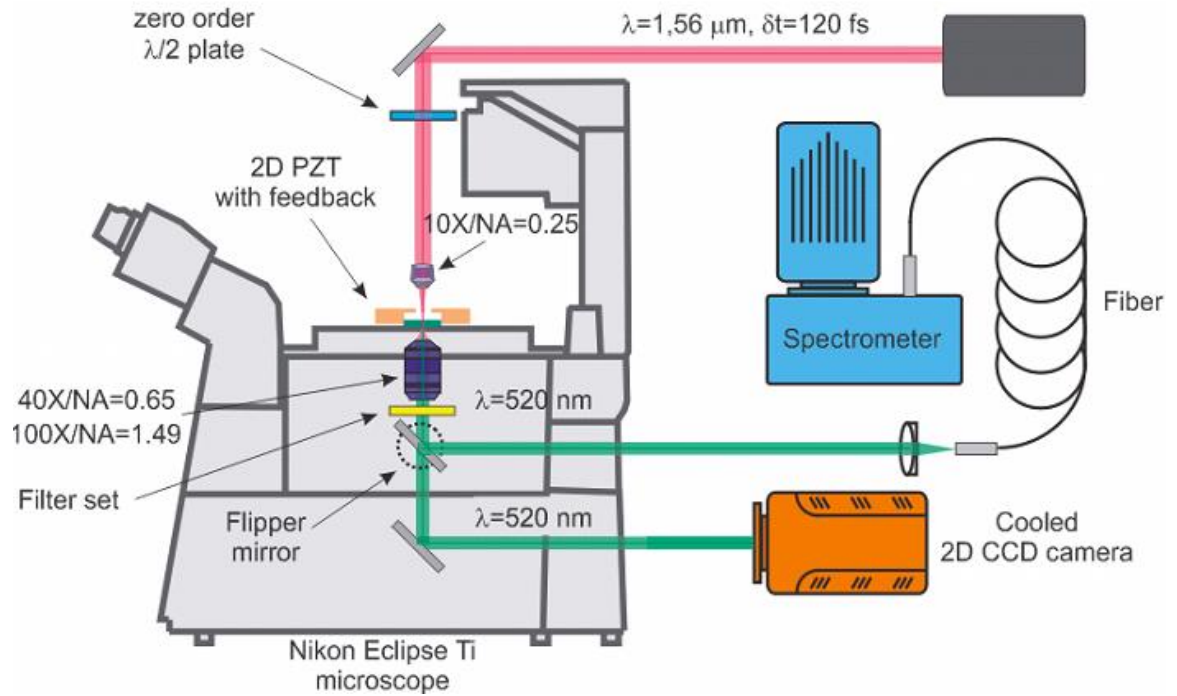


Figure 4.6 The schematic of the optical setup used in the references [19,20] to investigate aperture-based THG in transmission geometry. Reprinted with permission from Ref. [19]

4.4 Summary

Different configurations of experimental setups that are used for the measurement of the nonlinear optical response of the metasurfaces were presented. Some experimental setups in reflection and transmission geometries were introduced.

Chapter 5 : Theoretical Models in Nonlinear Optics

5.1 Introduction

This chapter reviews the theoretical methods for predicting the nonlinear optical response of metasurfaces. The harmonic oscillator model based on Miller's theory are explained. The nonlinear scattering theory is another model that is discussed in this chapter. The efficiency of these models in predicting the nonlinear optical response of metasurfaces is also discussed in more detail. Eventually, our recent work on the influence of surface plasmons on aperture-based THG is presented. In this work, the nonlinear scattering theory was used for estimating THG in an array of rectangular aperture.

5.2 Harmonic Oscillator Model

Nonlinear optical response of the metasurfaces can be estimated by harmonic oscillator model. This model has been developed based on Miller's theory [62]. Using this model, one can estimate the THG as the direct consequence of linear response of the nanostructure. The harmonic oscillator model can be represented by:

$$\ddot{x} + \gamma_0 \dot{x} + \omega_0^2 x - bx^3 = -\frac{e}{m} E_0 e^{-i\omega t} \quad (5.1)$$

Where γ_0 is the damping constant, ω_0 is the resonance frequency e is the electron charge and m is the effective mass of electron. The cubic perturbation b models the third harmonic response. The driving electric field E_0 at frequency ω stimulates the oscillator. This oscillator exists in a medium with electron density N that can be represented by linear susceptibility $\chi^{(1)}(\omega)$:

$$\chi^{(1)}(\omega) = \frac{Ne^2}{\epsilon_0 m} \frac{1}{\omega_0^2 - \omega^2 - i\omega\gamma_0} = \frac{Ne^2}{\epsilon_0 m} \frac{1}{D(\omega)} \quad (5.2)$$

The linear extinction spectra can be represented by:

$$\alpha(\omega) = \frac{\omega}{c} \text{Im} \left(\chi^{(1)}(\omega) \right) \quad (5.3)$$

Similarly, the THG is given by:

$$\chi^{(3)}(\omega_i, \omega_j, \omega_k, \omega_{THG} = \omega_i + \omega_j + \omega_k) = \frac{Ne^4}{\epsilon_0 m^3} \frac{b}{D(\omega_i)D(\omega_j)D(\omega_k)D(\omega_{THG})} \quad (5.4)$$

The third harmonic emission spectrum can be derived from:

$$I_{THG}(\omega_{THG} = \omega_i + \omega_j + \omega_k) \propto \omega_{THG}^2 \left| \int \chi^{(3)} E_0(\omega_i) E_0(\omega_j) E_0(\omega_k) \right|^2 \quad (5.5)$$

The contribution of the substrate is considered as constant, $\chi_{sub}^{(3)}$, that can be coherently added to the result. It has been shown in a few works that the calculated THG using this model is generally in good agreement with the measured THG [63-65]. Fig. 5.1.a shows the schematic of THG from a nanoantenna array. Fig. 5.1.b shows the SEM image of the fabricated nanoantennas.

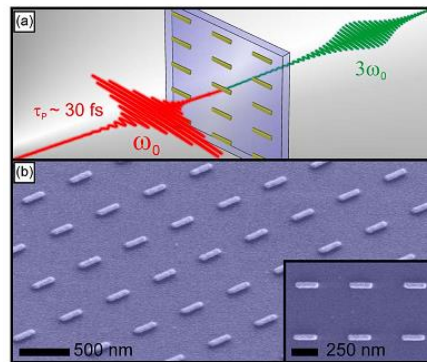


Figure 5.1 a) Schematic illustration of the plasmonic nanostructure under THG measurement b) Tilted SEM image of the fabricated structures. Reprinted with permission from Ref. [63]

Fig.5.2 shows the comparison of the normalized measured TH efficiencies on the linear extinction spectra of the nanoantenna array for different lengths of the nanoantenna depicted in the inset. There is a good agreement between calculated and measured values.

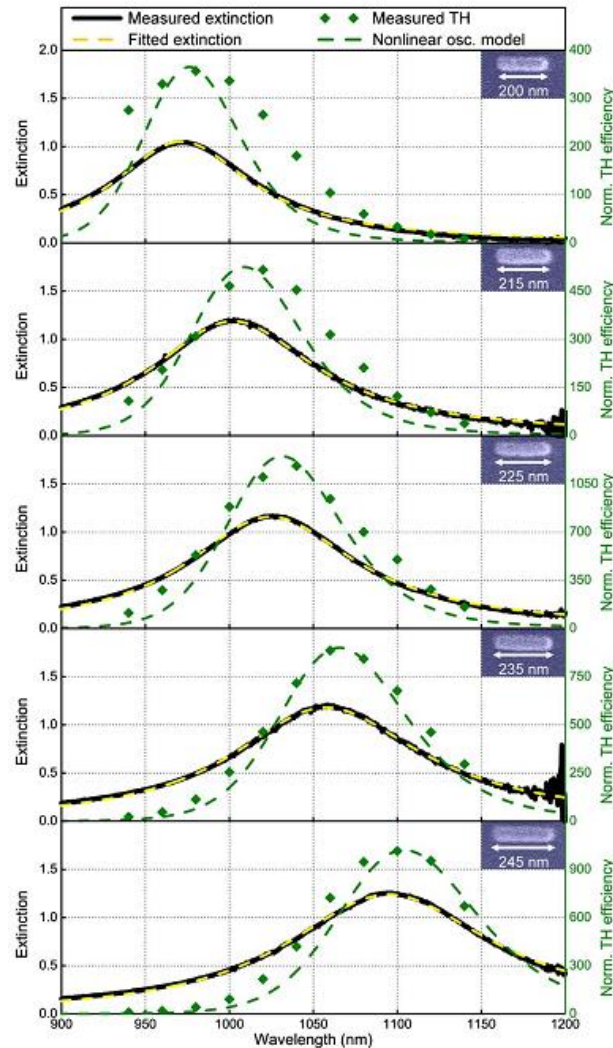


Figure 5.2 Illustration of calculated TH efficiency on the linear extinction spectra using harmonic oscillator model and corresponding measured spectra for different lengths of nanoantenna. Reprinted with permission from Ref. [63]

5.3 Nonlinear Scattering Theory

First, this section reviews a recent work that has utilized nonlinear scattering theory to predict the nonlinear optical response of the U-shaped structures. Later on in this section,

the model for the third harmonic case is developed. Towards the end of this section, the works related to the quantification of THG from metasurfaces by the nonlinear scattering theory are detailed.

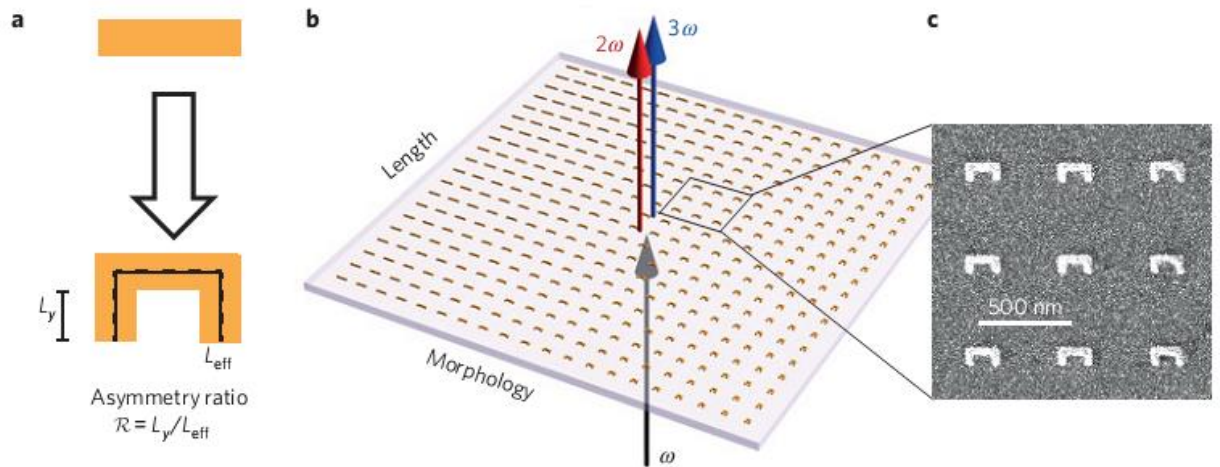


Figure 5.3 a) Illustration of parameter space: the length of the U-shaped structure arms are changed throughout the array b) Schematic of SHG and THG from the U-shaped structure: these nonlinear responses are a function of length and morphology of the structures. c) an SEM image of fabricated U-shape structures. Reprinted with permission from Ref. [67]

Fig. 5.3.a shows the parameter space of the U-shaped structure. Fig 5.3.b shows the schematic of the configuration of the incident beam and nonlinear optical responses that are a function of length and morphology of the structures and Fig. 5.3.c shows an SEM image of the fabricated structures. Fig. 5.4 Miller's theory does not match the experimental result for SHG. However, nonlinear scattering theory is quite efficient in finding the optimal structure [67]. The evaluation of the harmonic oscillator model and nonlinear scattering theory shows the domination of the latter in predicting SH response of the metasurfaces [66].

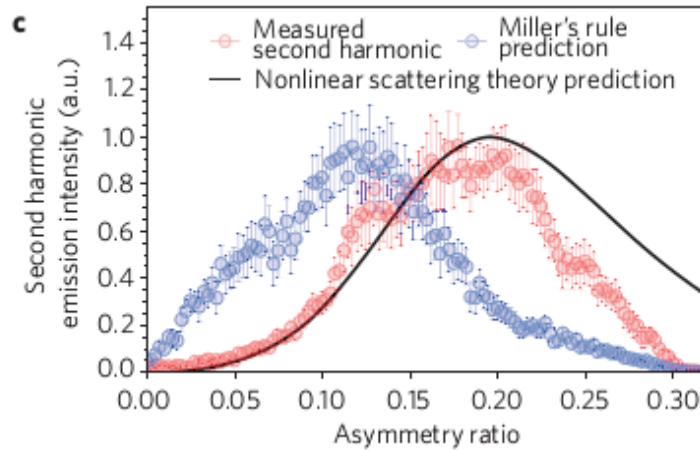


Figure 5.4 Illustration of the calculated SHG using two different methods: Miller's theory and nonlinear scattering theory as compared to the measured values. Reprinted with permission from Ref. [67]

Fig. 5.4 shows the comparison of the calculated result using harmonic oscillator model and nonlinear scattering theory for the U-shaped structure depicted in Fig. 5.3.a. According to these results, nonlinear scattering theory is an efficient tool to predict the nonlinear optical response of the U-shaped nanoparticles [67]. This approach is an extension of the Lorentz reciprocity theorem [68] in a nonlinear media [69,70]. For two current sources $\mathbf{j}_1(r, \omega)$, $\mathbf{j}_2(r, \omega)$ and their corresponding emitted optical electric fields $\mathbf{E}_1(r, \omega)$ and $\mathbf{E}_2(r, \omega)$ in a reciprocal medium, Lorentz reciprocity theorem results in the following integral relation over the volume of the excited nanostructure:

$$\int \mathbf{j}_2(r', \omega) \cdot \mathbf{E}_1(r', \omega) dV = \int \mathbf{j}_1(r, \omega) \cdot \mathbf{E}_2(r, \omega) dV \quad (5.6)$$

To extend this relationship to the nonlinear case, one can take the current source $\mathbf{j}_1(r, \omega)$ as the stimulating factor of the nonlinear dipoles in the surface or volume of the nanostructures exposed by this source. The current source and the polarization of the structures, $\mathbf{P}(r, \omega)$, are related by equation below:

$$\mathbf{j}_1(r, \omega) = \frac{\partial \mathbf{P}(r, \omega)}{\partial t} = i\omega \mathbf{P}(r, \omega) \quad (5.7)$$

The dipoles, on the other hand, emit unknown electric field of \mathbf{E}_1 . In the reciprocal condition of Eq. 5.6 the second source need to be in the detector place. This is a current dipole source with a polarization axis of $\hat{\mathbf{j}}$ and a length of Δl that emits the electric field $\mathbf{E}_2(r, \omega)$:

$$\mathbf{j}_2(r, \omega) = J_0 \delta(r - r_2) e^{i\omega t} \hat{\mathbf{j}} \quad (5.8)$$

By substituting Eq. 5.7 and Eq. 5.8 in Eq. 5.6, we obtain an equation for estimating the \mathbf{E}_2 :

$$\int \mathbf{E}_1 \cdot J_0 \delta(\mathbf{r}' - \mathbf{r}_2) e^{i\omega t} \hat{\mathbf{j}} dV' = \int i\omega \mathbf{P} \cdot \mathbf{E}_2 dV \quad (5.9)$$

$$\mathbf{E}_1 \cdot \hat{\mathbf{j}} = \frac{e^{-i\omega t}}{J_0 \Delta l} \int i\omega \mathbf{P} \cdot \mathbf{E}_2 dV \quad (5.10)$$

Fig. 5.5 shows the illustration of the nonlinear scattering theory in the reciprocal configuration.

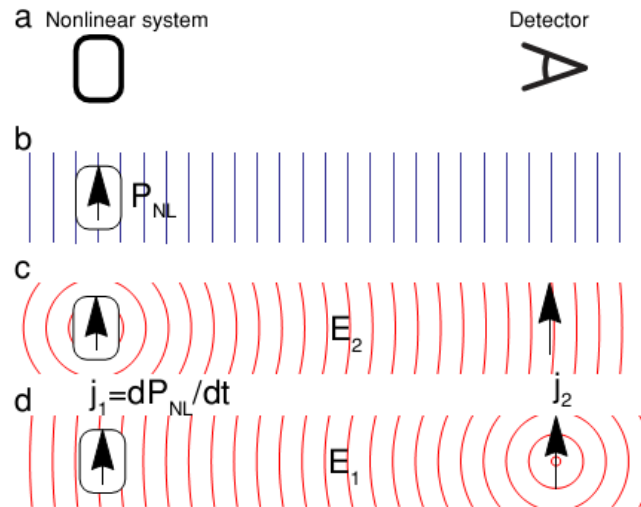


Figure 5.5 Illustration of the nonlinear scattering theory: The source at the detector position radiates a field at the harmonic wavelength toward the structure. The emitted harmonic

signal from the nonlinear system can be estimated by Eq. 5.10. Reprinted with permission from Ref. [67]

The theory has been previously developed to estimate SHG in the reciprocal media [69]. The theory was modified to quantify the THG in the aperture-based metasurfaces on a gold thin film. Fig. 5.6.a shows the schematic of the THG from an array of apertures in transmission geometry. The emitted third harmonic signal can be measured by a detector (spectrometer or photodiode) on the other side of the sample. In Eq. 5.10, E_1 is the unknown emitted third harmonic signal ($E_1 = E_{TH}$) and E_2 is the emitted field by a source at the third harmonic wavelength from the opposite side ($E_2 = E_{3\omega}$). Given the fact that the third order polarization of the nanostructure has cube dependence to the fundamental beam ($\mathbf{P} \propto \chi^{(3)} E_{\omega}^3$), the emitted third harmonic signal can be estimated by:

$$THG \propto \int_{gold} \chi_{gold}^{(3)} \mathbf{E}_{3\omega} \cdot \mathbf{E}_{\omega}^3 dV \quad (5.11)$$

Where $E_{3\omega}$ is electric field of the third harmonic and E_{ω} is the electric field of the fundamental light.

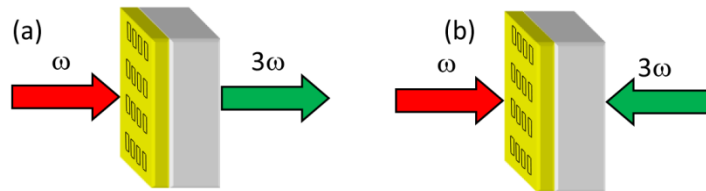


Figure 5.6 a) Schematic of third harmonic generation from a rectangular aperture array b) Simulated configuration for incident fundamental and third harmonic waves (using time-reversal for the harmonic beam).

FDTD simulation was performed (Lumerical FDTD 8.12.501) based on this approach to guide the experiments on aperture-based THG in transmission geometry. Fig. 5.6.b shows the configuration was used in the simulation.

5.4 Investigating the Effect of Localized Surface Plasmons (LSPs) and Propagating Surface Plasmon Polaritons (SPPs) on THG of the Aperture Arrays

The optimized structure for the efficient THG can be found by using the above-mentioned integral relation of Eq. 5.11 for all possible combination of LSP and SPP resonances. In the calculation, the third order susceptibility of the gold was excluded for the simplicity. These resonances are tuned either to the fundamental wavelength or third harmonic wavelength. On a related point, LSP resonance is controlled by the dimensions of the aperture in the array and the SPP resonance is sensitive to the periodicity of the array. Fig. 5.7.a shows the resultant THG using Eq. 5.11 ($\chi_{gold}^{(3)}$ is excluded for simplicity) for LSP resonance at the harmonic wavelength (523 nm) and SPP resonance at the fundamental wavelength (1570 nm) where l is the length of the rectangular aperture and P_y is the periodicity of the rectangular array in y direction. The width of the aperture, w , and the periodicity of the array, P_x , were fixed at 30 nm and 1400 nm.

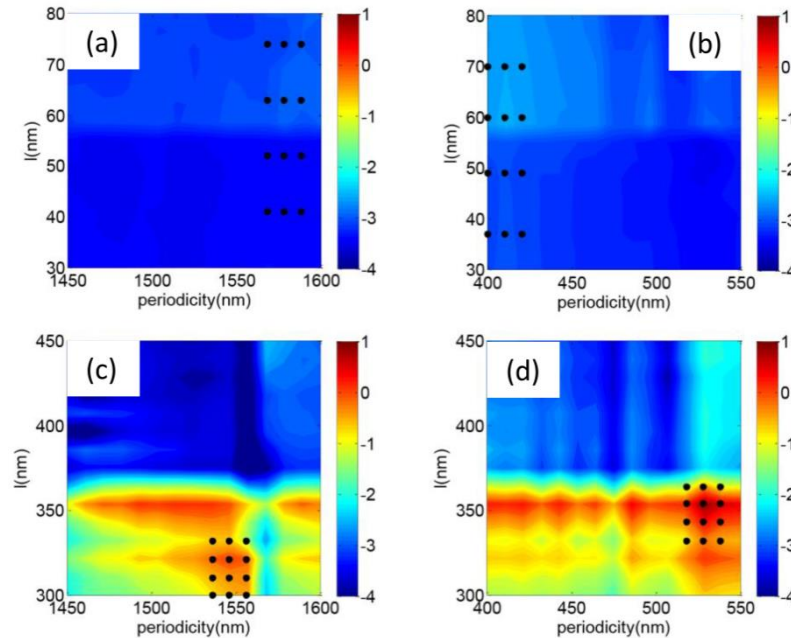


Figure 5.7 a) Calculated THG in natural logarithm scale using the nonlinear scattering theory of Eq. 2.24 for LSP resonance at 523 nm and SPP resonance at 1570 nm. b) Same as (a) for LSP and SPP resonance at 523 nm. c) Same as (a) for LSP and SPP resonance at 1570 nm. d) same as (a) for LSP resonance at 1570 nm and SPP resonance at 523 nm.

Fig. 5.7.b shows the same results for LSP and SPP resonances at the third harmonic wavelength. Fig. 5.7.c shows the calculated THG for LSP and SPP resonances at the fundamental wavelength and Fig. 5.7.d shows the results for LSP resonance at the fundamental wavelength and the SPP resonance at the third harmonic wavelength. These are plotted on a natural log scale. From these simulations, a region of interest was obtained for fabrication for each scenario to give the best conversion efficiency. The fabricated dimensions are shown with the black dots on Figs. 5.7.a-d.

5.4.1 Fabrication and THG Measurement

Guided by the simulation results, the nanostructures were fabricated around the maxima shown in Fig. 5.8. Focused ion beam (FIB) milling was used to fabricate the arrays of rectangles. A Ga ion beam was focused on a spot of 15 μm of 100 nm thick

gold film at 40 KV acceleration voltage, 0.01064 nA beam current and dwell time of 10 μ s. Fig. 3.6 shows scanning electron microscope images of the fabricated structures for different periodicities in the y direction (P_y) and length of the rectangle (l) corresponding to different LSP and SPP resonances. The periodicity in the x direction (P_x) and width of the rectangle (w) took fixed values of 1400 nm and 30 nm.

Fig. 5.9.a shows a schematic of the optical setup used for the THG measurements. A 100 fs pulsed laser was used at 1570 nm with 40 MHz repetition rate. The incident power was 40 mW, focused onto the sample by an objective lens (40 \times , NA=0.65).

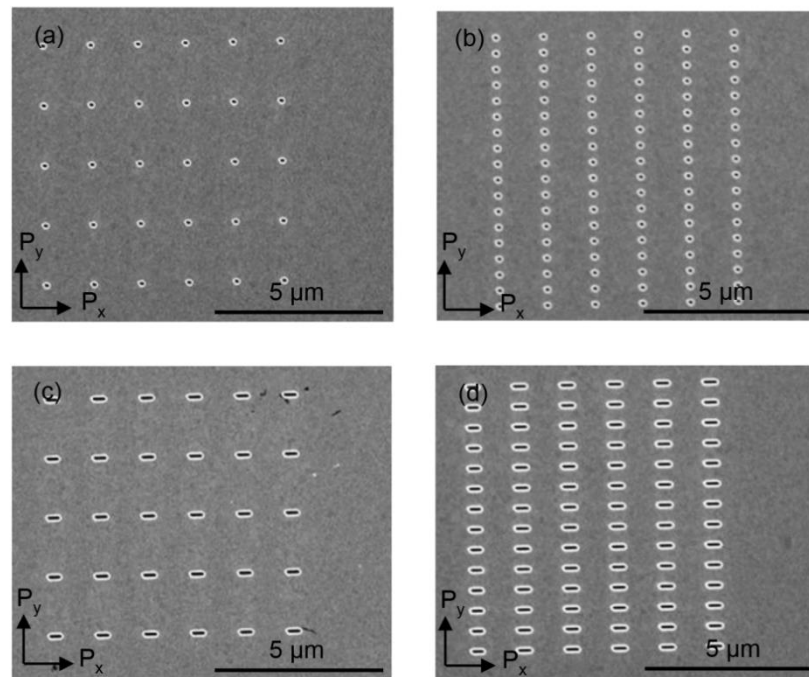


Figure 5.8 Scanning electron microscopy images of the fabricated structures on a 100 nm thick gold film for: (a) LSP resonance at 523 nm and SPP resonance at 1570 nm ($l=41$ nm, $P_y=1578$ nm). (b) LSP resonance at 523 nm and SPP resonance at 523 nm ($l=70$ nm, $P_y=400$ nm). (c) LSP resonance at 1570 nm and SPP resonance at 1570 nm ($l=310$ nm, $P_y=1546$ nm). (d) LSP resonance at 1570 nm and SPP resonance at 523 nm ($l=343$ nm, $P_y=528$ nm). Where l is the length of the rectangular aperture and P_y is the periodicity of the array in the y-direction. The width of the aperture (w) and the periodicity of the array in the x-direction (P_x) were fixed values of 30 nm and 1400 nm.

Theoretically, the pulsed laser spot size should be approximately 3 microns. In practice, it was discovered that the focusing was sensitive to translations around 10 microns (smoothly varying over this range), so the spot size is likely slightly larger than the array. A guide laser beam at the wavelength of 853 nm was used to help alignment but was turned off during the measurements. The third harmonic beam on the transmission side was collected by a second objective lens (40 \times , NA=0.65).

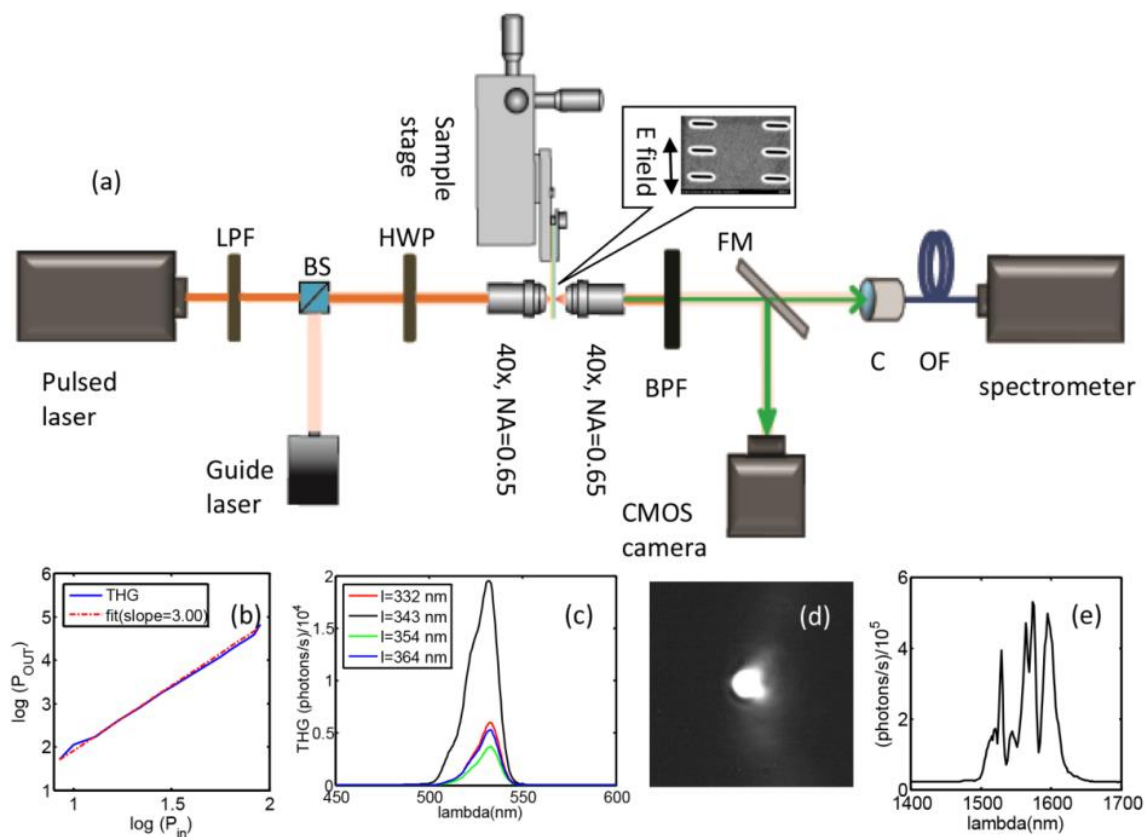


Figure 5.9 a) Schematic of the experimental setup used to measure THG of the fabricated array of rectangles where LPF is low pass filter, BS is a beam splitter, HWP is half wave plate, FM is flip mirror, C is collimator and OF is an optical fiber. The inset shows the sample with the electric field polarization of the incident beam. b) Power dependence of measured THG (solid blue curve) on the input power in logarithm scale. The dashed red curve shows a fit with slope 3. c) Measured THG for the array designed for LSP resonance at 1570 nm and SPP resonance at 523 nm that yields the maximum conversion efficiency for

a different length of the aperture and fixed $P_y = 518$ nm. d) Third harmonic green spot imaged on the CCD camera. e) The measured power spectrum of the pulsed laser source.

The transmitted beam contained THG was confirmed by the power scaling of the light at the spectrometer (Fig. 5.9.b) and by the wavelength of the emitted light (Fig. 5.9.c). The fundamental beam was not detected by the photodiode. Bright green emission was visible on a CMOS camera (Thorlabs, DCC1545M), as shown in Fig. 5.9.d. There was photoluminescence [71,72] present in the measurements; however, this signal was much weaker than the third harmonic and consequently not visible in Fig. 5.9.c. To estimate the directivity of the THG, the collection objective was removed and an iris was placed in the beam 3 cm from the gold surface. The THG collected was reduced when the iris was reduced to 1 mm, implying a half angle of approximately 1° . Theoretically, the angle from a Gaussian aperture of 7.3 microns (width of the array) at 523 nm should be 1.3°

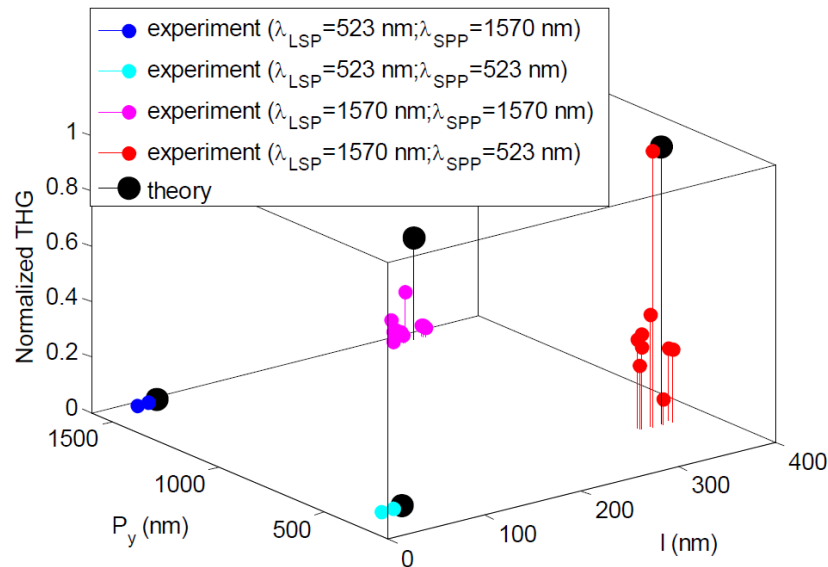


Figure 5.10 Normalized third harmonic generation versus array parameters for different LSP and SPP resonance scenarios. Theoretical results from simulations are also shown.

Fig. 5.10 shows the final result of this work, comparing the THG for different configurations of SPP and LSP resonances at the fundamental and the third harmonic wavelengths. Good agreement is seen between the simulation results using the reciprocity relation in Eq. 5.11 and the experiment.

5.4.2 Discussion

Here, the key features found for efficient THG from the simulations and experiments are discussed. First, it is advantageous to tune the SPP resonance (i.e., the Bragg resonance of the periodic hole spacing) to the third harmonic wavelength instead of the fundamental wavelength. This is seen for both LSP configurations. The reason for this is related to the requirement to efficiently out-couple the THG away from the aperture array and towards the detector. The Bragg resonance improves the out-coupling efficiency of the third harmonic by directly coupling it to an outgoing plane wave. While nonlinear interactions can be boosted by tuning the Bragg resonance of the lattice to the third harmonic, the directivity of the third harmonic signal is also improved. The latter helps to efficiently out-couple third harmonic signal towards the detector and consequently prevents the resonant absorption of THG at the gold surface.

Next, we note that it is best to have the LSP resonance of the aperture at the fundamental wavelength. The LSP resonance provides a strong local field at the aperture, which gives an increased THG when considering Eq. 5.11 (since the THG scales as the cube of the fundamental intensity). Of course, it is possible to obtain high field intensity by using the SPP Bragg (grating) resonance as well, and indeed, the second best efficiency results are obtained when both the LSP and SPP are at the fundamental wavelength. However, this comes at the expense of efficient directive out-coupling of the

THG, and so it did not yield the greatest THG detected. In other words, in this case, the LSP resonance of the apertures is tuned to the fundamental wavelength, which results in efficient confinement of the incident beam. The Bragg resonance can also improve nonlinear interactions inside the apertures further due to an improved in-coupling. However, the TH signal is not efficiently out-coupled in this case, and so the overall THG collected is reduced.

Interestingly, it does not seem particularly advantageous to put the LSP at the third harmonic wavelength. While the resonance at the third harmonic will enhance the THG from Eq. 5.11, it does so only with a linear power. Furthermore, the LSP at the third harmonic leads to local resonant absorption by the gold, so that much of the light will not be detected. Related to this point, it should be noted that the LSP resonance is very effective at coupling the incident light into the aperture, and so there is little benefit from adding the SPP Bragg resonance. For example, it has been shown that the normalized transmission through an aperture at the LSP resonance is close to a quarter of the wavelength squared [73]. When we consider the aperture as a dipole that radiates in the forward and backward directions equally, the total scattering of that aperture is already close to the single channel limit [74,75]. This should be compared with particle plasmonics, where the scattering cross section is usually less than a third of the single channel limit [76-80]. In summary, rectangular apertures have a very strong LSP resonance that benefits THG.

From our experiments, we measured an output power at 523 nm by replacing the spectrometer with an avalanche photodiode (Thorlabs – APD 110A). Using the responsivity specified for this APD at 523 nm (measuring 30 mV for the maximum

THG), we estimated that the maximum achieved total conversion efficiency of the aperture array (including all collection optics) was 0.05%. The green light was clearly observable by bare eyes. For comparison, the conversion efficiency of a split ring resonator array was reported to be 3×10^{-5} % [81], and the conversion efficiency for a single aperture was reported to be 0.001% [20]. Even though we are still far away from ~10% percent conversion efficiencies that are our ultimate goal for real applications, there are some avenues that could lead us to get closer to that goal. Using apertures prevents the sample from overheating by having a good conducting layer [19,20]. Therefore, we can benefit from a higher power pulsed laser to boost conversion efficiency without suffering from melting (estimated to be three orders of magnitude lower heating than for comparable plasmonic particles [20]). Moreover, confining light in a very small gap can increase the power further and contribute to increasing THG. By using new fabrication techniques such as He beam milling [82], atomic layer deposition (ALD) [83], shadow mask lithography [15,84], and template stripping [85], a gap size below 10 nm should be achievable. The effect of gap size on THG is discussed in detail in Chapter 7.

5.2 Summary

In this chapter, the theoretical models for the estimation of the nonlinear response of the metasurfaces were introduced. The harmonic oscillator model based on Miller's theory which is quite efficient in predicting SHG was explained. The nonlinear scattering theory based on Lorentz reciprocity theorem was also discussed. It was shown that nonlinear scattering theory could successfully predict the optimum U-shaped structure for maximum SHG. Finally, our recent work on the design and characterization of the array

of rectangular aperture for maximum THG was introduced. In this work, we investigated the effect of tuning LSP and propagating SPP resonance to the fundamental and third harmonic wavelength. Our experimental result supports the predicted THG based on nonlinear scattering theory.

Chapter 6 : Quantum Corrected Model and THG

6.1 Introduction

This chapter explains the principles of the quantum-corrected model as an effective tool to study nonlocal effects on the confined electric field in very small gap region where the classical quantum mechanics fails. In this chapter first, the rectangular barrier model is utilized to predict the electron transmission through a self-assembled monolayer (SAM). The prediction of THG on the onset of tunneling using QCM will also be discussed in this chapter.

6.2 THG on the Onset of Electron Tunneling

Quantum electron tunneling can limit the field enhancement in the sub-nanometer gap region and consequently can suppress the third harmonic generation. Previously, the quantum-corrected model (QCM) has been used to theoretically predict the saturation of plasmonic fields at the onset of tunneling, with good agreement with more comprehensive quantum simulations [86]. In those works, the scattering rate was used as a fitting parameter; however, in the supplementary information of the QCM model paper [87], the modified carrier density in the gap was also considered as a fitting parameter. We adopted the latter approach because it is expected that the carrier density will be reduced in the gap, but the scattering rate will be similar to that of the metal. This is analogous to the famous debate about the existence of a superconducting state in the barrier between Josephson and Bardeen (for example, see note added at proof [88]), where ultimately was determined that the Cooper pairing was not broken by scattering in the barrier region. We used the standard transmission coefficient for tunneling with different gap sizes similar to the Eq. 2.65 for $E_f < V$ [54]:

$$T(d) = \frac{1}{1 + \frac{1}{4} \frac{V^2 \sinh^2(\alpha k d)}{\alpha E_f (V - E_f)}} \quad (6.1)$$

$$V = E_f + \varphi_B \quad (6.2)$$

$$\kappa = \frac{\sqrt{2m\varphi_B}}{\hbar} \quad (6.3)$$

Where φ_B is the barrier height, E_f is Fermi energy, α is the ideality factor that accounts for deviation from rectangular barrier shape, m is the electron mass, k is the electron wave vector in the barrier, V is the barrier height plus the Fermi energy (i.e., the total energy) and \hbar is the reduced Planck constant. The values

$$\alpha = 0.65, V = E_{fAu} + \varphi_{B-SAM} = 5.53eV + 1.42eV = 6.95eV \quad (6.4)$$

were taken from a past work on tunneling through SAMS [89]. The plasma frequency inside the gap can be derived from [90]:

$$\omega_g(d) = \sqrt{T(d)} \omega_{pAu} \quad (6.5)$$

We set the scattering rate equal to that of gold $\gamma_{gAu} = 4 \times 10^{13}$ (rad/sec) as a fixed value which is equal to the collision frequency of gold [91].

To modify material inside the gap region, we used effective Drude model:

$$\varepsilon(d, \omega) = \varepsilon_\infty - \frac{\omega_g^2(d)}{\omega(\omega + i\gamma_g)} \quad (6.6)$$

The electric field intensity of the third harmonic $I_{3\omega}$, for lossless homogeneous waveguide is directly proportional by cube electric intensity of fundamental beam I_ω [92]. The χ^3 susceptibility of gold is three orders of magnitude higher than quartz, and we considered it to be the dominant contribution to nonlinear conversion [43,93]. This is

supported by the experimental observation that varying the SAM layer thickness on the gold film did not vary the THG for the case where no nanoparticles were present.

$$I_{3\omega} \propto \int I_{\omega}^3 dV \quad (6.7)$$

Table 6.1 shows calculated plasma frequencies and resulted integrated values inside the gap for five different SAM layer spacers.

Table 6.1 Calculated plasma frequencies and resulted integrated values inside the gap for five different SAM layer spacers.

d (nm)	$\omega_g(d)$ (rad/sec)	$\int I_{1570}^3 dv$ (over metal region)
0.51(c2)	2.4×10^{15}	3.8222×10^{-7}
0.69(c3)	1.1777×10^{15}	1.6162×10^{-6}
0.94(c6)	4.3897×10^{14}	1.0241×10^{-6}
1.16(c8)	1.8427×10^{14}	9.4336×10^{-7}
1.55(c11)	3.9555×10^{13}	3.1823×10^{-7}

We simulated the scattering using Lumerical FDTD ver. 8.1. A single Drude-model material was used to model the tunneling region in the gap. This was set to a diameter of 3 nm and had the width of the gap. The scattering rate was chosen to be the same as gold, and the plasma frequencies are shown in Table 6.1. The SAM was assumed to have a refractive index of 1.5. Experimental data for Au was chosen from Johnson and Christy [94]. The mesh spacing was set to 0.3 nm in the gap region and over the thin film, and 5 nm encompassing the nanoparticle. We used a plane wave source at 50-degree incident angle with TM polarization and perfectly matched layer boundaries. Figs. 6.1 and 6.2 show the simulation results for the QCM and classical Drude model conditions. The

QCM clearly shows the saturation of the field beginning for c3 and becoming pronounced for c2.

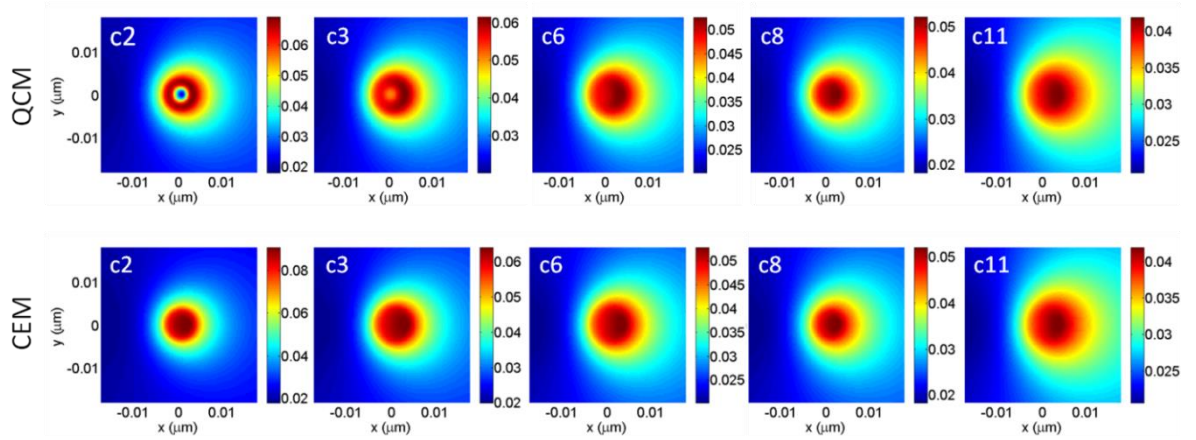


Figure 6.1 Spatial distribution of electric field intensity at the metal surface in the xy plane for five different spacer sizes at wavelength 1570 nm. QCM has been used to achieve top row results whereas CEM results have been depicted in the bottom row.

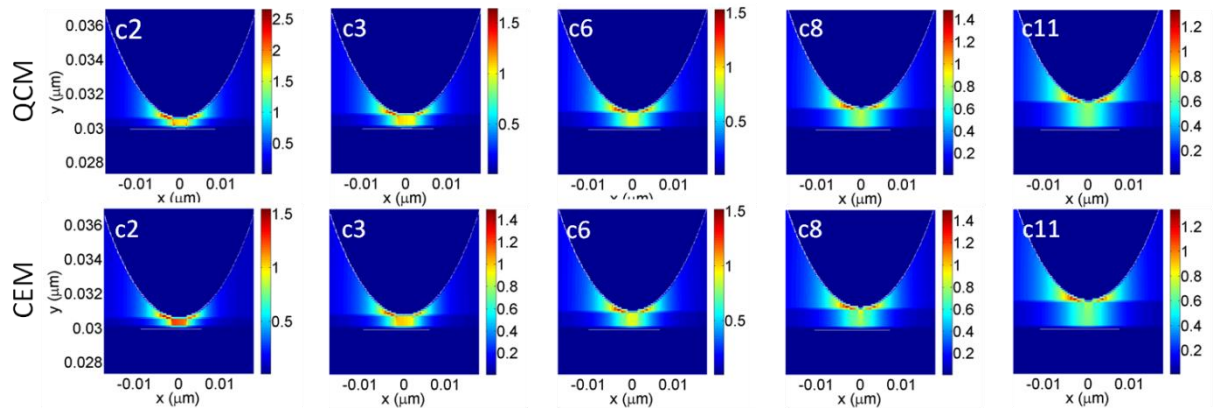


Figure 6.2 Spatial distribution of electric field intensity at the metal surface in the xz plane for five different spacer sizes at wavelength 1570 nm. QCM has been used to achieve top row results whereas CEM results have been depicted in the bottom row.

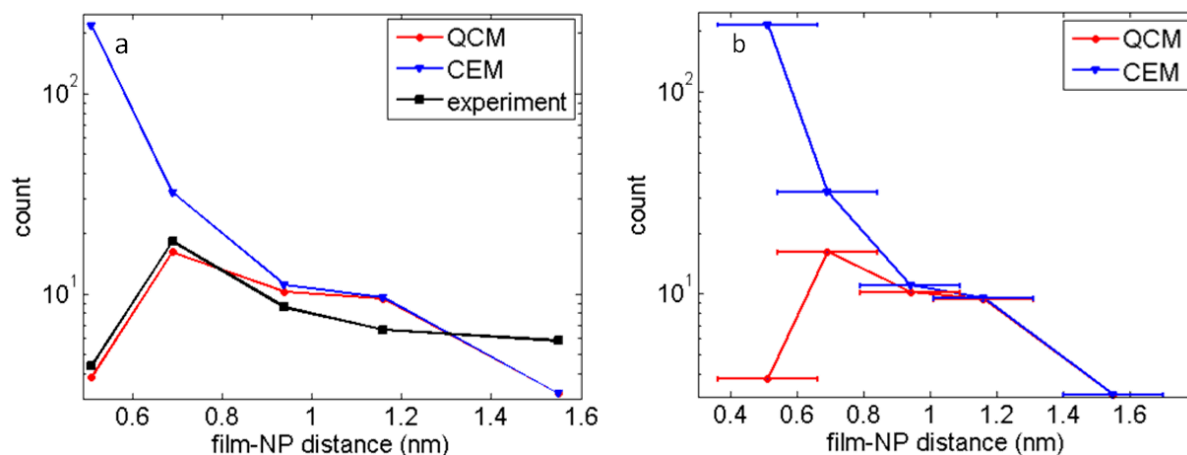


Figure 6.3 THG intensity simulation results versus film-NP distance for QCM and CEM approaches. There is extraordinary suppression in field intensity as the gap size goes beyond 0.57 nm which is in extremely good agreement with our experimental results.

The integrated intensity cubed over the region of the metal region was used to quantify the third harmonic generation, as given in Eq. 6.7. This is shown in Fig. 6.3.a, as compared with the experiment, for both the classical model and the QCM. The uncertainty is given by the half the mesh size in the gap region (Fig. 6.3.b).

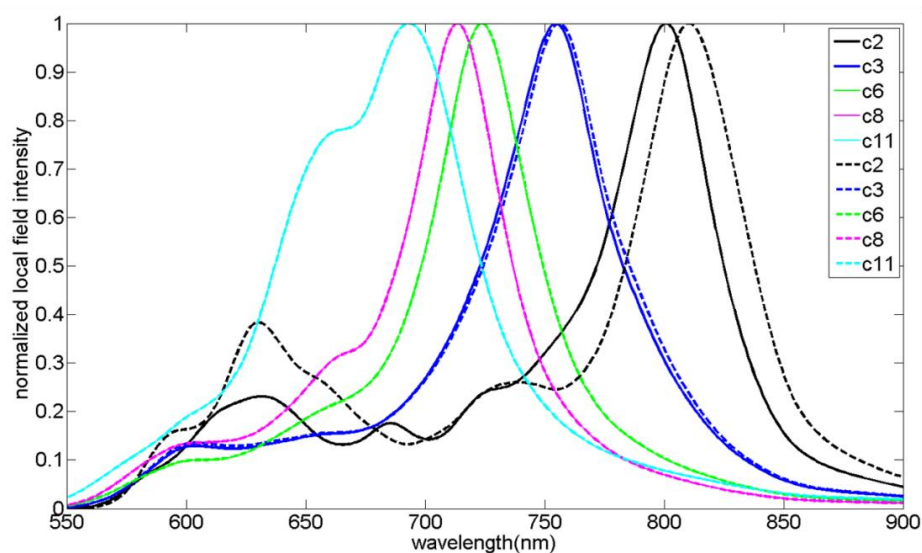


Figure 6.4 Local field intensity at the maximum point inside the gap under the nanoparticle using QCM (solid line) and CEM (dashed line) for different SAM layer types.

Fig. 6.4 shows the local field intensity at the maximum point under the nanoparticle as a function of wavelength for the classical and QCM models. What is clear from these simulations is that the classical and QCM models show nearly identical values for the peak resonance wavelength, and these both agree reasonably well with the resonance values found by dark-field scattering measurements in Figure 4 of reference [95].

6.3 Summary

This chapter presented the simulation results for THG from the film-coupled nanosphere structures. A modified QCM was used to estimate the THG for different gap sizes in the range of 0.51-1.55 nm. It was discovered that the THG on the onset of tunneling is suppressed dramatically. However, CEM failed to predict such behavior. On the other hand, using these approaches, there was no significant change in the position of the maximum local field intensity in the gap region.

Chapter 7 : Gap Plasmon Enhanced THG In Aperture-based Metasurfaces

7.1 Introduction

This Chapter mainly discusses the effect of gap plasmon resonance on the nonlinear optical response of the plasmonic structures. First, some works related to the influence of gap plasmons on local electric field enhancement are reviewed. An attempt is made to bridge the optimal nanoantenna design methodology for enhanced electric field to its THG counterpart. To do this, a review of the theory of optical resonance circuits is included. We used this theory to justify our findings regarding optimal nanostructure design for THG.

7.2 Film-coupled Nanosphere Structure [96]

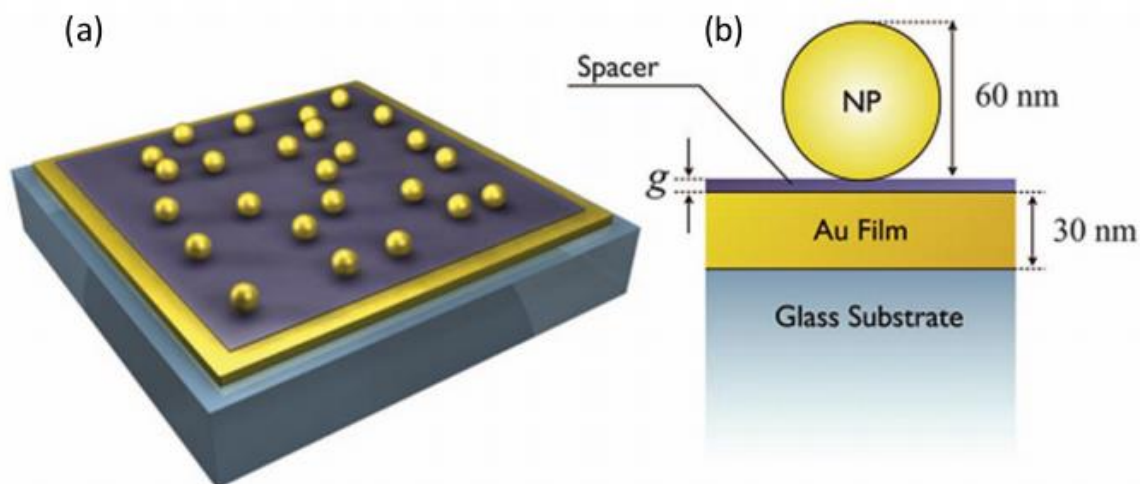


Figure 7.1 Illustration of the geometry of the film-coupled nanoparticle a) sample b) the cross section view of a single film-coupled nanoparticle. Reprinted with permission from Ref. [96]

Fig. 7.1 shows the schematic of a film-coupled nanoparticle sample. Fig. 7.1 shows the cross section of a single nanoparticle on a gold film. A self-assembled monolayer (SAM)

of amine terminated alkanethiol has been used as the spacer between the nanoparticle and the gold film. Using this method, a separation range of 0.5 to 2.0 nm is achievable. For larger separations of the range 2.8 to 26.6 nm, a layer-by-layer (LBL) deposition of polyelectrolytes is used. In this work, the resonance scattering peaks of the film-coupled nanoparticle system for different gap sizes have been calculated. Both local and nonlocal models have been utilized for this purpose. Fig. 7.2.a shows the resonant peak position and Fig. 7.2.b shows the corresponding enhancement factor using these approaches.

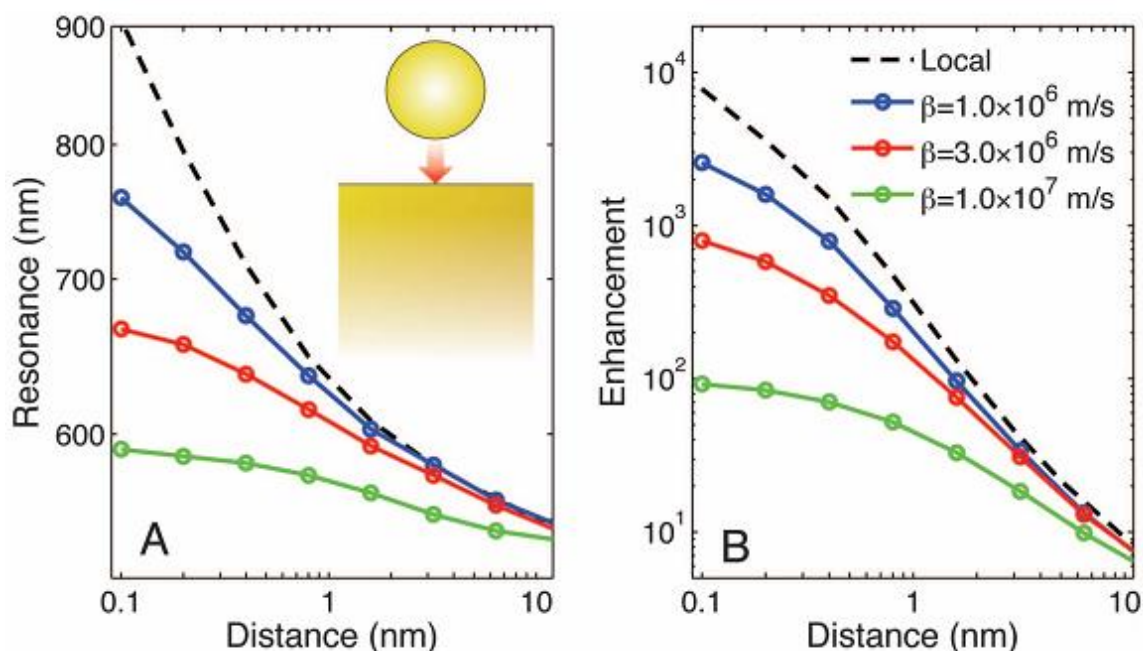


Figure 7.2 a) The position of peak scattering intensity versus gap size b) The field enhancement ratio as a function of gap size. Reprinted with permission from Ref. [96]

From these results, it is obvious that there is an extreme on the enhancement rate in the absence of nonlocality. In the nonlocal results, however, there is a limit on the ultimate enhancement [96]. However, it has been recently discovered that these are essentially related to the surface roughness [97]. In other words, for an ultra flat gold surface and before the onset of tunneling, the electric field within the gap region is enhanced with no

saturation as the gap size is decreased [97]. Since third order nonlinear response of the materials has a cube dependence to the fundamental beam intensity, enhanced third harmonic generation from plasmonics structures with the small gap regions should be observed. We explore this effect in subsequent sections.

7.3 THG in Bowtie Nanoantenna Structure [64]

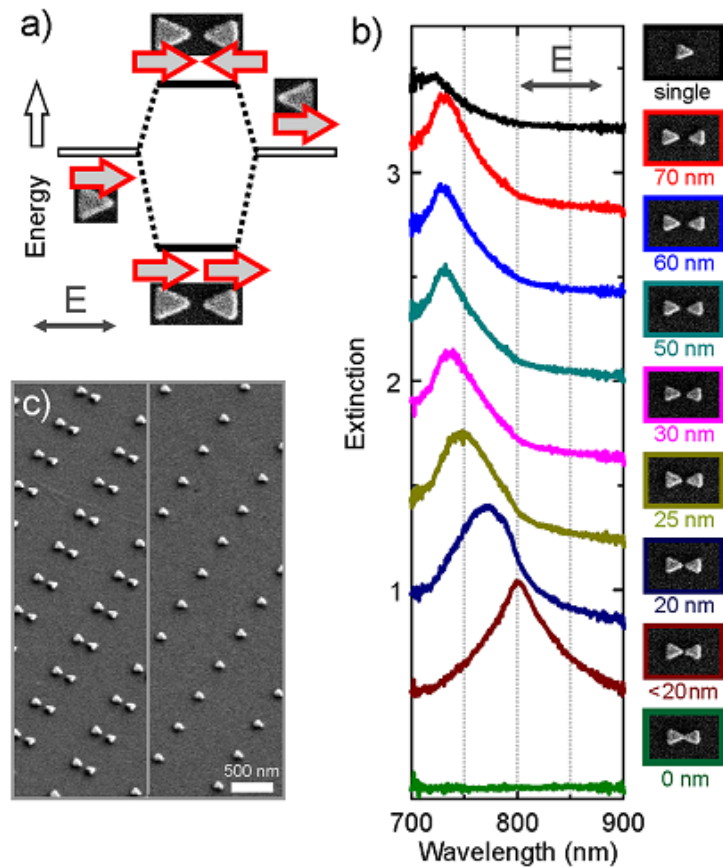


Figure 7.3 a) Plasmonic dimer within the framework of plasmon hybridization b) Measured extinction spectra as a function of gap size c) Tilted SEM image of the bowtie nanoantenna array. Reprinted with permission from Ref. [64]

Fig. 7.3.a describes the bowtie plasmonic dimer within the framework of plasmon hybridization. Fig. 7.3.b shows the linear measured spectra of the bowtie dimer for different gap sizes. It can be seen that the peak redshifts as the gap size decreased. Fig. 7.3.c shows the tilted SEM image of the fabricated bowtie nanoantennas as an example of

plasmonics structures with the gap. Fig. 7.4 shows the linear and nonlinear results for the bowtie nanoantennas with different gap sizes. Both experimental and calculated results are shown in these figures. Harmonic oscillator model has been used for the calculation. The gray area in the left column is the incident beam spectra. The maximum third harmonic generation is observed at the gap of 20 nm.

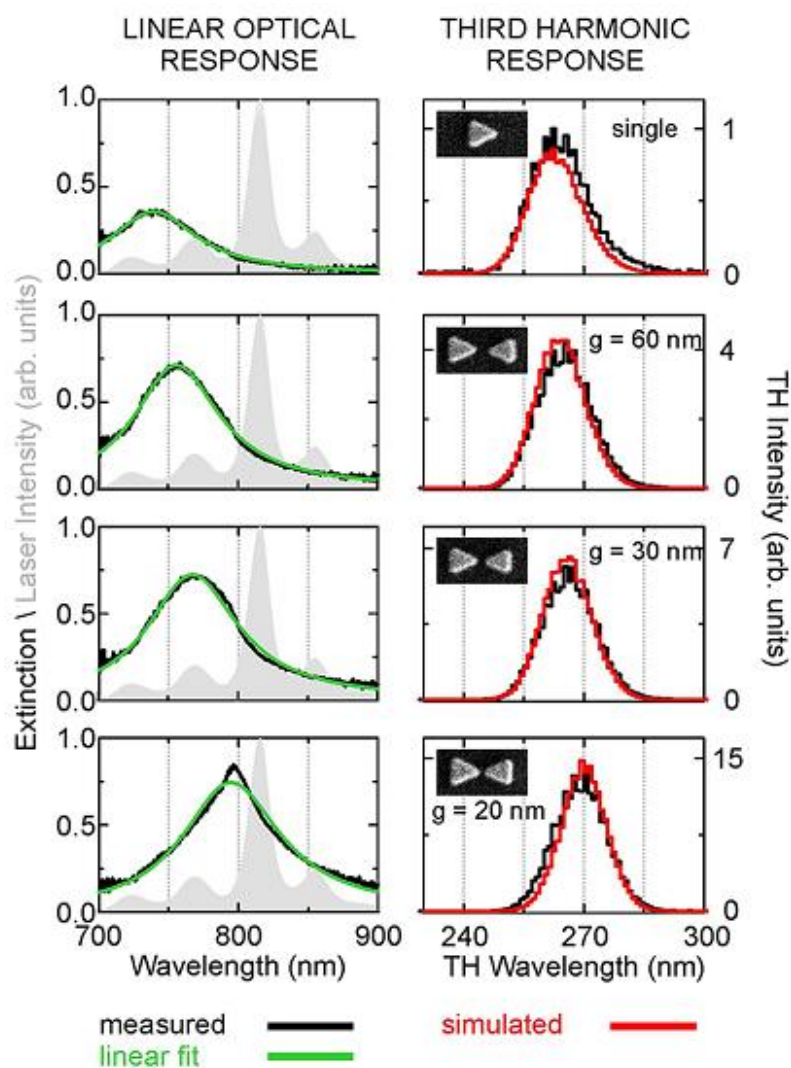


Figure 7.4 Comparison of the calculated and measured linear (left column) and nonlinear (right column) optical response of the bowtie nanoantenna for single and gap sizes: $g=60$, $g=30$ and $g=20$ nm. Reprinted with permission from Ref. [64]

As it was seen before, by decreasing the gap size the linear extinction spectra redshifts and overlaps with the maximum incident field intensity. This further contributes to the THG enhancement at the corresponding gap size (20 nm).

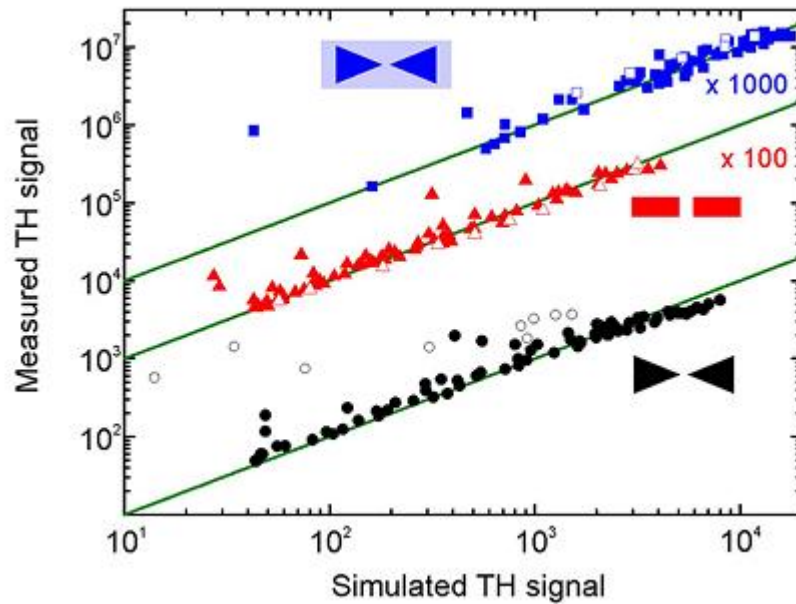


Figure 7.5 Measured spectrally integrated TH signal versus simulated TH signal based on single nonlinear oscillator model for the gap antennas (red) the glass covered bowtie (blue) and the bowties (black). Reprinted with permission from Ref. [64]

Fig. 7.5 shows the measured and calculated third harmonic signal using single nonlinear oscillator model for different nanoantenna structures: glass covered bowtie (blue), gap antenna (red) and bowtie (black). Eq. 5.5 has been used in this calculation. As it can be seen from this figure, the calculated values are in very good agreement with the experimental measurements except for the smallest gap size (~ 20 nm) samples that are shown with the white symbols. It can be noted that harmonic oscillator model fails to predict the nonlinear response of the nanostructures with the gap size close to 20 nm or smaller.

In this thesis, the third harmonic generation in transmission geometry was investigated. Therefore, the loss inside the aperture also plays an important role that is related to the radiation engineering of nanoantennas for optimal field enhancement. An explanation of the nanoantenna design methodology is provided in the following sections.

7.3 Radiation Engineering for Maximum Field Enhancement [98]

Nanoantennas are metal structures that can emit electromagnetic fields in the optical range from visible to infrared. At these nanoscale dimensions, the behavior of the devices cannot be explained by RF antenna theory. Since metallic nanoantennas have a negligible loss at RF frequencies, they can be considered as perfect electric conductor; however, at optical frequencies, they have large resistive losses. Therefore, to maximize the energy transfer from the incident radiation, the radiative impedance should match the absorptive impedance. This is also valid for the nanostructures with a small gap. The field enhancement at resonant wavelength based on coupled mode theory (CMT), can be derived from [98]:

$$\frac{|E_{loc}|^2}{|E_i|^2} = \frac{aA_c \lambda_{res}}{\pi} \frac{Q}{Q_{rad}} \frac{Q}{V_{eff}} \quad (7.1)$$

Where E_{loc} and E_i are the local field amplitude and the incident field amplitude at the hot spot in the gap region, A_c is the maximum effective aperture of the antenna, V_{eff} is the effective mode volume of the resonator and the total quality factor of Q is related to the radiation quality factor (Q_{rad}) and absorption quality factor Q_{abs} by equation below:

$$\frac{1}{Q} = \frac{1}{Q_{rad}} + \frac{1}{Q_{abs}} \quad (7.2)$$

The condition for maximum field enhancement in the gap nanoantenna can be achieved by solving:

$$\frac{\partial}{\partial Q_{rad}} \left(\frac{|E_{loc}|^2}{|E_i|^2} \right) = 0 \quad (7.3)$$

That leads to:

$$Q_{rad} = Q_{abs} \quad (7.4)$$

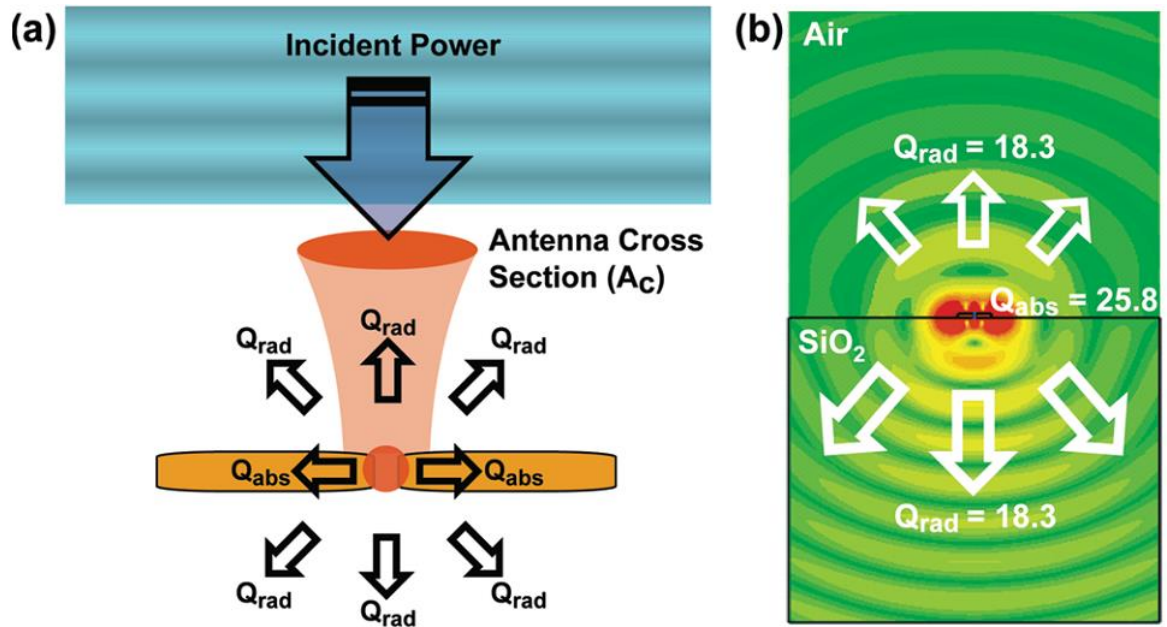


Figure 7.6 Schematic diagram of a nanoantenna within the framework of coupled mode theory b) Simulation of the radiation pattern of the dipole nanoantenna on a quartz substrate. Reprinted with permission from Ref. [98]

Fig. 7.6.a shows the configuration of nanoantenna within the framework of coupled mode theory. Fig. 7.6.b shows the simulation of a dipole antenna on a quartz substrate. It is obvious that the most of the radiated field from the antenna is lost in the substrate that further results in weak coupling of the excitation radiation to the antenna.

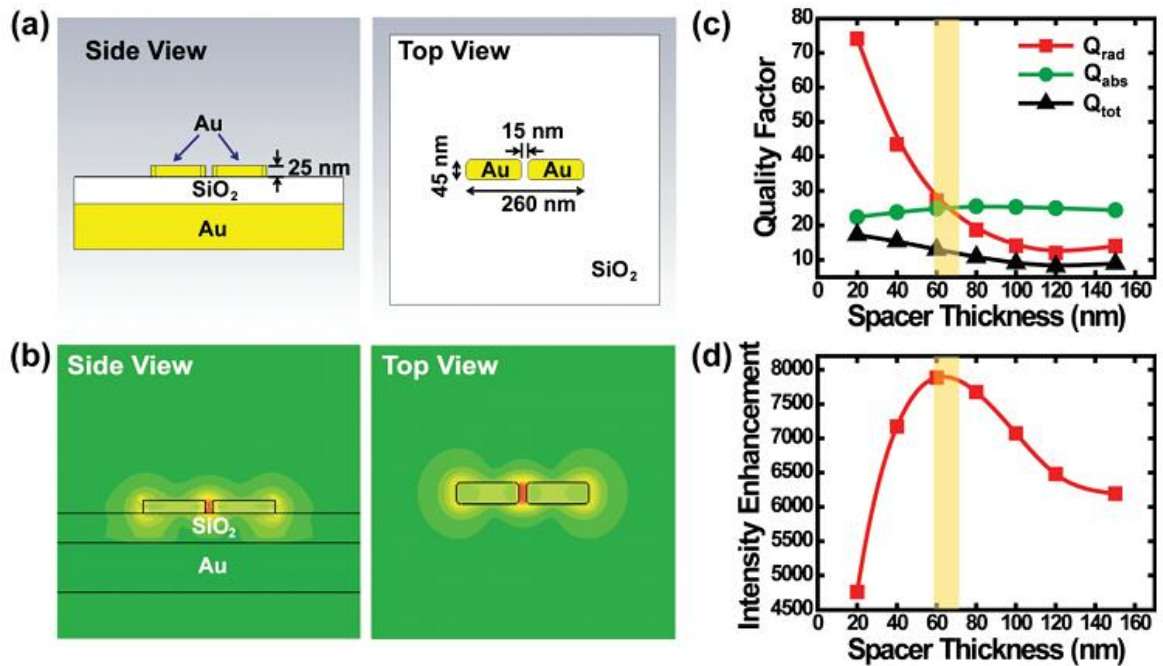


Figure 7.7 a) The schematic diagram of a dipole nanoantenna with a small gap b) the electric magnitude distribution c) Quality factor plots as a function of the spacer thickness d) Field intensity enhancement as a function of space thickness: the maximum enhancement happens where the quality factor of absorption and radiation coincide. Reprinted with permission from Ref. [98].

Fig. 7.7.a shows the schematic of a nanoantenna with a small gap. Fig. 7.7.b shows electric field magnitude distribution of the nanoantenna. By controlling the absorption or radiation part of the quality factor, the efficiency of the antenna can be improved. Since the absorption is dictated by the properties of the metal and its losses, the quality factor of radiation should be controlled such that it crosses the absorption quality factor. The radiation of the dipole antenna and its image cancel each other more and more as the spacer thickness reduced beyond $(\frac{\lambda}{4})$ thickness. At the optimum spacer thickness, the radiation Q of the antenna could be matched to the absorption Q of the antenna that consequently leads to the maximum field enhancement condition. Fig. 7.7.c shows the quality factor plots versus the SiO₂ dielectric spacer thickness. Fig. 7.7.d shows the field

intensity enhancement as a function of the SiO₂ dielectric spacer thickness. The maximum enhancement is achieved for the matching condition of Eq. 7.4.

7.4 Effect of Matched Scattering and Absorption Rate on THG From a Single Slit

The same approach as the linear case was used to investigate the effect of matching scattered and absorbed field on the THG from a single slit. For this purpose, the FDTD simulation was utilized for calculation of the scattering and absorption cross section of the single slit structure (the inset in Fig. 7.8.a) for the gap sizes 1 nm to 20 nm. Later, nonlinear scattering theory was used to estimate the third harmonic generation from this structure. Fig. 7.8.a shows the scattering and the absorption cross section spectra which resulted from the FDTD simulation. Fig. 7.8.b shows the scattering cross section, absorption cross section and related THG for different gap sizes. These are all calculated in a resonance condition. In analogy to the fundamental theory of impedance matching for maximum power delivery in circuits, the maximum THG results from a gap of 4 nm where the scattering and absorption cross sections match. Later in this chapter, this theory is used to interpret our findings for the array of annular ring array.

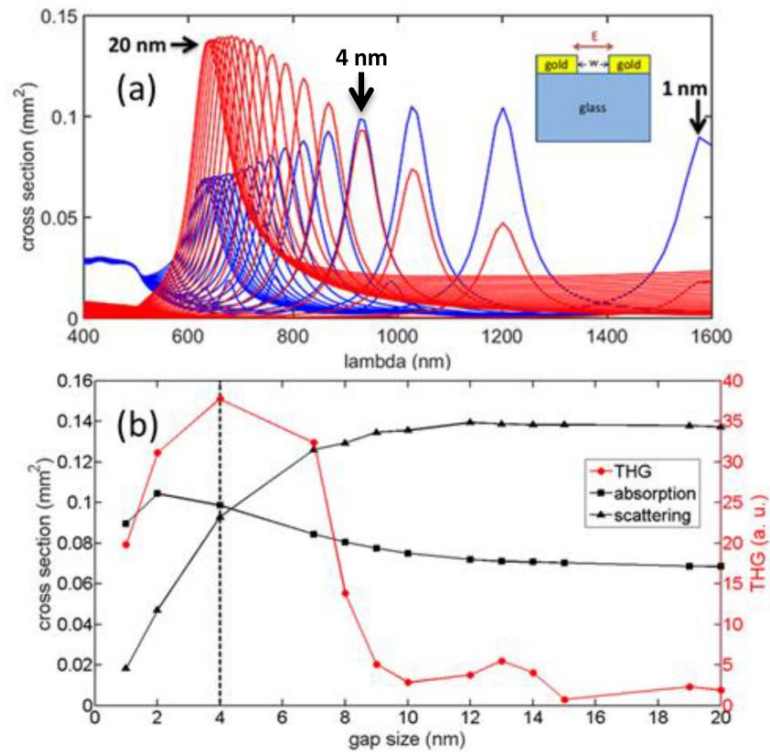


Figure 7.8 a) Absorption (blue curve) and scattering (red curve) cross section spectra for different gap sizes, w , of the slit configuration depicted in the inset. The polarization of the incident light is parallel to the width, w , of the slit. The thickness of the gold film is 100 nm. b) Resonant THG prediction based on nonlinear scattering theory (red) and corresponding absorption and scattering (black) for different gap sizes, w , of the slit. Note that the optimal THG occurs when the absorption and scattering cross sections are equal.

7.5 Effect of Gap Plasmons on Aperture-based THG

Research has recently been conducted on the effect of gap plasmons on THG. The THG of the array of annular ring apertures as a closed loop structure has been measured in transmission geometry. In this structure, the gap is filled with alumina. Moreover, we repeated the experiment for the open-loop structures such as an array of double nano-holes (DNHs) and an array of H-shaped apertures. These results were compared with our previous results for an array of rectangular apertures. Our results showed that the

conversion efficiency of the array of H-shaped apertures is up to 9 times greater than the array of rectangular apertures. FDTD simulations based on nonlinear scattering theory were carried out which support the experimental finding for the closed loop structures. We found that the thermal damage could be a limiting factor of THG enhancement. Since the dielectric region plays an important role in THG, particularly at the smallest gap, it should be considered in calculating the total THG from the annular ring structure. The total out-coupled THG from the annular ring structure can be estimated by:

$$\text{THG} \propto \int_{\text{gold}} \chi_{\text{gold}}^{(3)} \mathbf{E}_{3\omega} \cdot \mathbf{E}_{\omega}^3 dV + \int_{\text{Al}_2\text{O}_3} \chi_{\text{Al}_2\text{O}_3}^{(3)} \mathbf{E}_{3\omega} \cdot \mathbf{E}_{\omega}^3 dV \quad (7.5)$$

Where $\chi_{\text{gold}}^{(3)}$ is the third order susceptibility of gold and $\chi_{\text{Al}_2\text{O}_3}^{(3)}$ is the third order susceptibility of alumina that are $7.6 \times 10^{-19} \text{ (m/v)}^2$ [43] and $2.3 \times 10^{-23} \text{ (m/v)}^2$ [99]. For other structures such as the H-shaped aperture, DNH and rectangular arrays, we used equation 5.11 since there is no alumina in the gaps. Fig. 7.9 shows the calculated THG from the annular ring structures versus the inner ring diameter and for different gap sizes. It can be seen from the results that the peak conversion efficiency occurs at smaller ring diameters for the smaller gap sizes. Maximum conversion efficiency is from the 14 nm gap at 150 nm inner ring diameter.

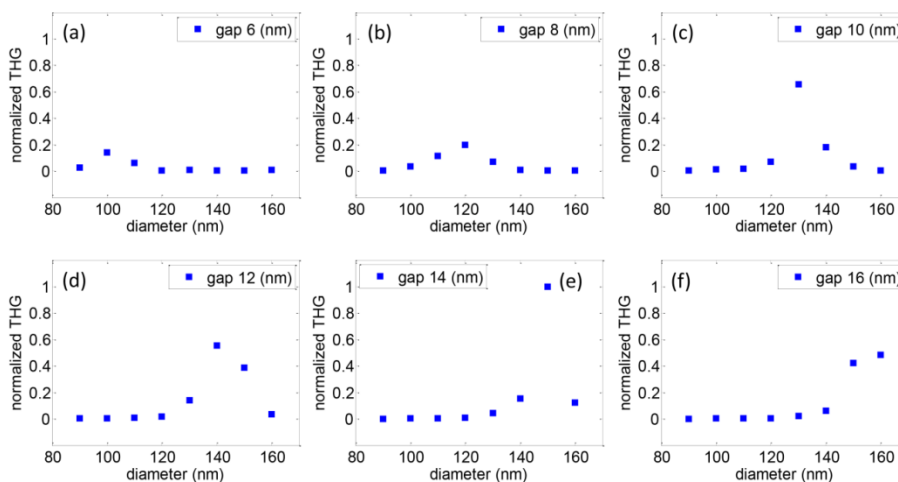


Figure 7.9 Calculated normalized THG versus inner ring diameter in annular ring structures using Eq. 3.1 for different gap sizes: a) 6 nm b) 8 nm c) 10 nm d) 12 nm e) 14 nm f) 16 nm.

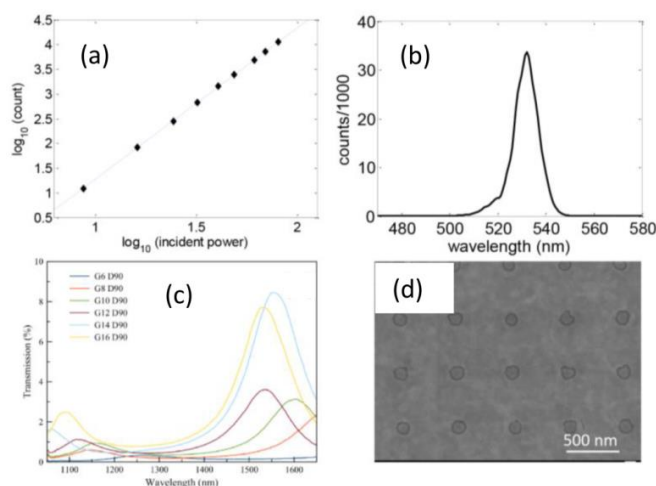


Figure 7.10 (a) THG incident power dependence is shown on a logarithmic scale with a slope of 3.07. (b) Measured THG signal from the spectrometer. (c) Linear transmission spectra of the annular ring structures for different gap sizes and fixed ring diameter of 90 nm.

7.5.1 Nonlinear Measurements and Discussion

We used the same optical setup configuration as Fig. 5.9.a. A He-Ne laser beam at 633 nm used on top of the fundamental beam at 1550 nm. Fig. 7.10.a shows the power dependence of the third harmonic signal to the input power on a logarithmic scale with

the slope of 3.07. Fig. 7.10.b shows the measured spectrum of the third harmonic signal of the spectrometer, shown a peak at a third of the fundamental wavelength, as expected from THG. Fig. 7.10.c shows measured linear transmission spectra of the fabricated annular ring structures for different gap sizes and fixed ring diameter of 90 nm. Fig. 7.10.d shows the SEM image of an array of annular ring apertures.

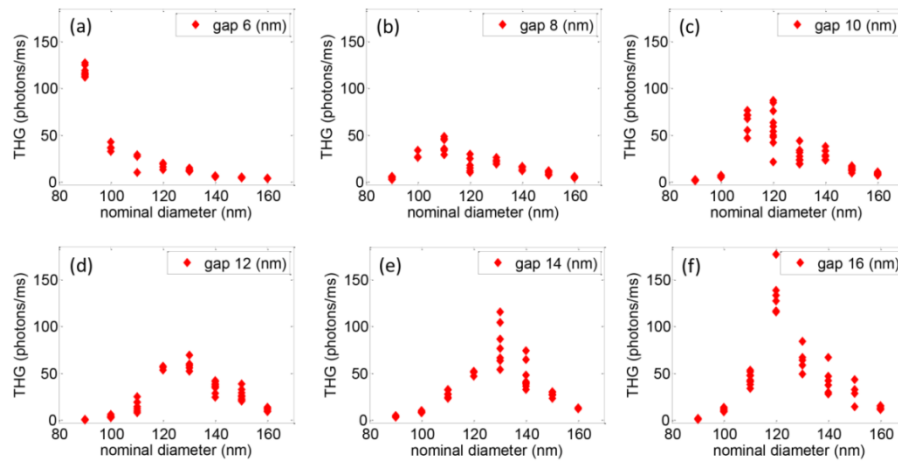


Figure 7.11 Measured THG signals versus inner ring diameter in the annular ring structures for different gap sizes: (a) 6 nm (b) 8 nm (c) 10 nm (d) 12 nm (e) 14 nm (f) 16 nm

Fig. 7.11 shows the measured THG in transmission geometry versus inner ring diameter in annular ring structures with different gap sizes. The trend shows a good agreement with the simulation results except for two outliers: 1- For the smallest gap size and at the smallest diameter, the THG is quite high whereas it was weak in the simulation results. This may be the result of shape imperfections in the fabricated structure, which may be improved with further iterations. 2- The larger gaps have peaks at smaller diameters than predicted by theory. This might be related to the thermal damage to the samples at these high powers which we had observed in the disconnected structures in the past as depicted in Fig. 8.1.

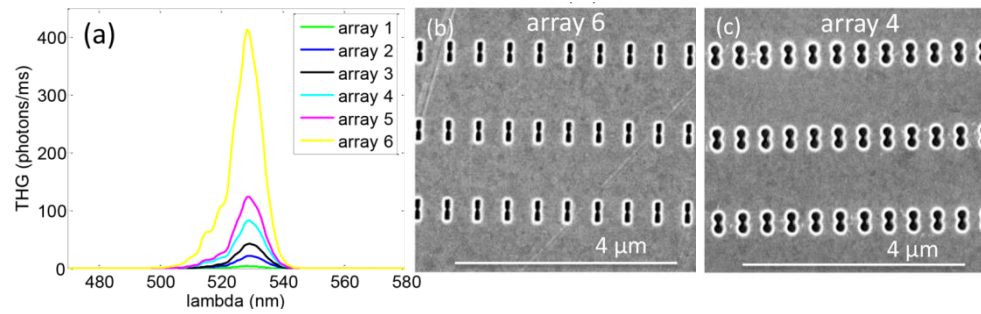


Figure 7.12 a) Measured THG spectra for different aperture geometries and periodicities; array 1: array of rectangular aperture, $w=20$ nm, $l=343$ nm, $P_x=518$ nm; array 2: DNH, $g=60$ nm, $P_x=518$ nm; array 3: rectangle, $w=40$ nm, $l=343$ nm, $P_x=518$ nm; array 4: DNH, $g=60$ nm, $P_x=410$ nm, array 5: H-shaped, $g=40$ nm, $P_x=410$ nm; array 6: H-shaped, $g=40$ nm, $P_x=530$ nm where w is the width of rectangular aperture, l is the length of rectangular aperture, g is the gap size of the DNH and H-shaped aperture, and P_x is the periodicity of the array in the direction of the fundamental wave polarization b) SEM image of the optimum H-shaped array structure for THG c) SEM image of the optimum DNH array structure for THG.

Fig. 7.12.a shows the measured THG from aperture arrays with different geometries and fabrication parameters. H-shaped, DNH, and rectangular arrays were fabricated on the same sample. Figs. 7.12.b and c show the SEM images of the optimum aperture array structures for THG. The figures shown are for the best results found among a wider range of parameters scanned. Comparing to our previous results for an array of rectangular apertures, these new results show that the H-shaped aperture can show even higher conversion efficiencies by a factor of 9 due to the smaller gap and local confinement in the center. The DNH also has a narrow gap but is not an as good candidate for THG enhancement. From these results, we found that the gap plasmon resonance in the H-shaped and DNH apertures could improve third harmonic conversion efficiency further.

Table 7.1 shows a quantitative comparison of the experimental and simulation results for the fabricated structures that are generally a good agreement.

Table 7.1 Comparison of the experimental and simulation results for different aperture array structures

Structure	Normalized experiment	Normalized simulation
Rectangular array	0.10	0.13
DNH array	0.20	0.24
H-shaped array	1	1
Annular ring array	0.43	0.30

7.5.2 Methods

7.5.2.1 FDTD Simulation

Lumerical FDTD 8.12.501 was used to perform simulations to feed into the nonlinear scattering theory. Anti-symmetric boundary condition in the x-direction and symmetric boundary condition in the y direction were used. Two 3D monitors at 1570 nm and 523 nm around the aperture region were used to collect the induced fundamental and third harmonic beam in the gold and dielectric region. A 2D index monitor was used in the xy plane to collect the refractive index of the material in the xy plane. Using this technique, we could discriminate dielectric and metal region. Using the index monitor, two overlay masks were defined to extract fundamental and third harmonic electric fields for dielectric and gold regions. For the annular ring structure, the THG from Eq. 7.5 was found by superposition of the resulted THG from gold volume around the aperture and dielectric volume inside the aperture. For other fabricated structures (H-shaped, rectangular, DNH), just the gold volume around the apertures was taken into account. A mesh override region with the same dimensions as the 3D monitors was used. We used 1

nm mesh size in all directions. The conformal mesh 1 refinement technology that is reliable in metal-dielectric structures was also utilized.

7.5.2.2 Fabrication Methods

Annular ring arrays fabricated using ALD similar to the past works [100-102]. The thickness of the fabricated annular ring arrays is 150 nm. To fabricate arrays of H-shaped and DNH apertures, focused ion beam milling technique was used. The details of fabrication methods is provided in Chapter 3.

7.6. Summary

This chapter described the influence of gap size on the THG. Previous works on the effect of gap size on the field enhancement within the gap were introduced. Radiation engineering for maximum field enhancement was discussed later. Eventually, our recent work on the effect of gap plasmons on the THG of the aperture-based plasmonic structures was presented. In this work, we proved that the maximum THG does not result from the minimum gap size. However, at the optimum gap size, where the scattering and absorption rate match, the maximum THG can be achieved. This is more obvious in the results presented for an array of annular ring apertures. Our simulation and experimental results for an array of H-shaped and DNH apertures were also provided. The THG results were compared to the array of rectangular apertures that previously discussed in Chapter 5. We achieved a third harmonic conversion efficiency of 0.5 percent for the H-shaped structure that, to date, is the greatest reported efficiency for the aperture-based structures in transmission geometry.

Chapter 8 : Conclusion and Future Work

8.1 Introduction

Our previous work on the effect of gap plasmon on aperture-based THG in transmission geometry showed a promising result. In particular, we found that with a gap of around 30 nm for an array of a connected structure such as H-shaped aperture, we could achieve up to 0.45 % conversion efficiency. These results are promising for nonlinear metasurfaces with >1-10% efficiency for applications including optical switching, wavelength conversion, near field imaging, subwavelength photolithography, and spectroscopy. As mentioned before, the field inside the aperture is inversely proportional to the gap size. On the other hand, THG has cube dependence to the fundamental beam. This basically means that if we could get a gap size of sub 10 nm, we would achieve close to 30 times higher conversion efficiency that makes our structures suit for industrial applications. However, there are two main challenges to getting to this point. First, the enhanced field in that small gap region increases the temperature that consequently could lead to damage to the structure. Due to lack of removing heat from the surface, this issue is more obvious in the closed loop (disconnected) apertures (e.g. coaxial structures). Fig. 8.1 shows two examples of the damaged structures exposed by the same pulsed laser power. Encapsulating disconnected structures could help to prevent the structure from thermal damage.

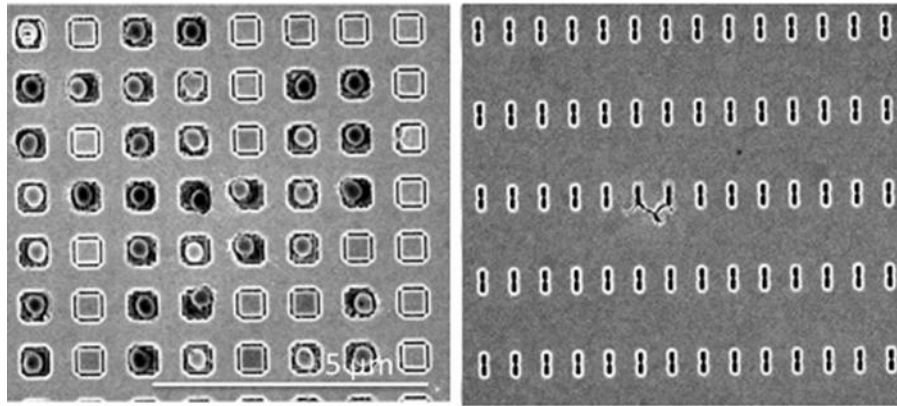


Figure 8.1 Examples of damaged structures a) disconnected structures b) connected structures

The second challenge that we were facing is the fabrication of the sub-10 nm structures. With the focused ion beam milling machine and with the perfect alignment of the ion beam, a gap of around 20 nm is achievable. With new fabrication techniques such as He beam milling, atomic layer deposition and template stripping, sub 10 nm structures are achievable. Template stripping is a cheap and fast way of making structures. In Appendix 3 examples of the fabricated silicon templates and template-stripped structures are provided.

8.2 Metasurfaces for Nonlinear Wave Front Phase Control

It has been shown that the linearly transmitted light through an aperture-based metasurface can be steered or focused at the desired point near the surface of the sample [103,104]. The phase of the wavefront can be manipulated by changing the shape or dimensions of the aperture. Fig. 8.2 shows an example of a flat focusing lens using cross-shaped aperture. The phase can be tuned such that the transmitted light from the boundary of the array constructively interferes with the light passed through the center apertures of the array.

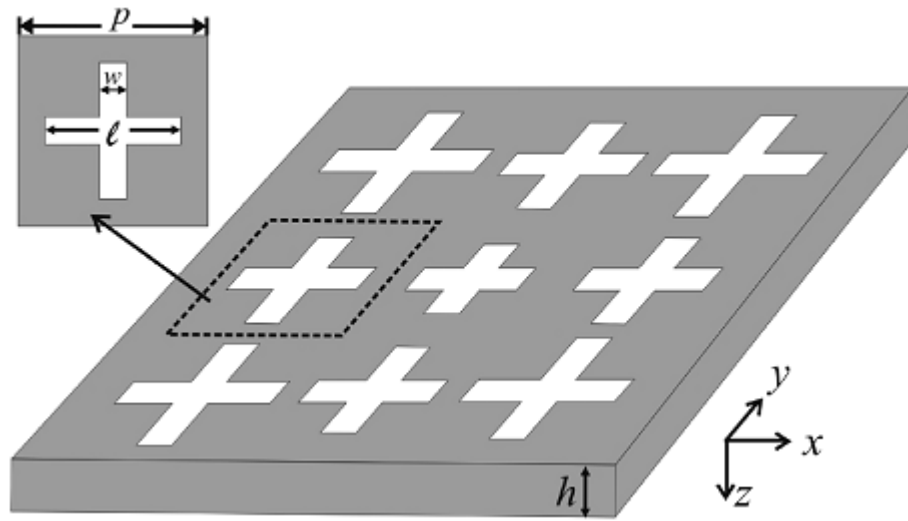


Figure 8.2 The schematic diagram of a linear plasmonic lens with cross-shaped apertures.

Reprinted with permission from Ref. [103]

The phase at each array position (x,y) can be obtained from [103]:

$$\varphi_{xy} = 2\pi \left(f_D - \sqrt{x^2 + y^2 + f_d^2} \right) / \lambda + 2n\pi + \varphi_{00} \quad (8.1)$$

where f_D is designed focal length, λ is the wavelength of the focused light, φ_{00} is the phase at the center of the array. The maximum phase shift in this case can not be more than π radian. Therefore another condition for the design of such a lens can be represented by:

$$|\varphi_{xy} - \varphi_{00}| \leq \pi \quad (8.2)$$

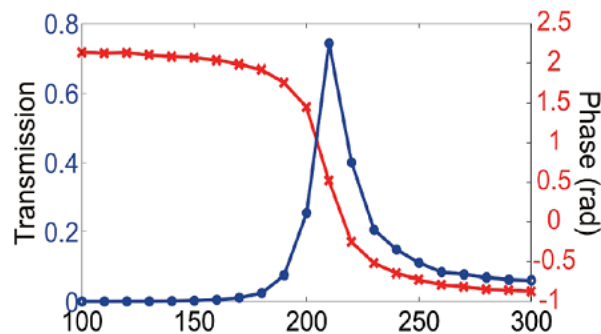


Figure 8.3 The transmission efficiency and the corresponding phase of the transmitted light as a function of arm length. Reprinted with permission from Ref. [103]

Fig. 8.3 shows the linear transmission efficiency and the phase of the transmitted field as a function of the arm length of the cross-shaped aperture. Figs. 8.4.a-b show the calculated phase and arm length for the 2D lens structures shown in Figs. 8.4.c-d for $f_D=15\ \mu\text{m}$ and $f_D=25\ \mu\text{m}$.

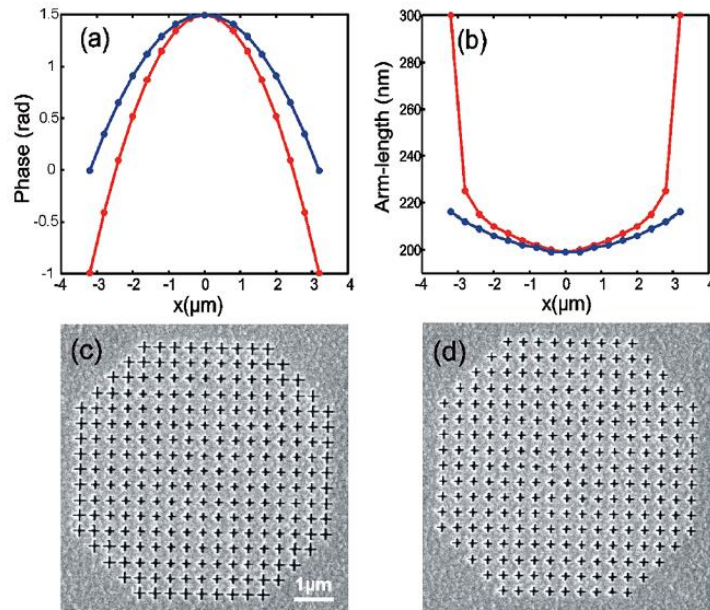


Figure 8.4 a) The calculated phase associated with apertures in a 2D array along x-axis b) The calculated arm length associated with apertures in a 2D array along the x-axis. Reprinted with permission from Ref. [103]

Fig. 8.5.a shows measured intensity profile for the 2D structure with fixed arm length apertures as a reference, Fig. 8.5.b shows the intensity profile for the flat lens with $f_D=15\ \mu\text{m}$, Fig. 8.5.c shows the intensity profile for the flat lens with $f_D=25\ \mu\text{m}$. Figs. 8.5.d-h shows 2-D intensity profile of the transmitted light at $z=0, 7, 14, 21,$ and $28\ \mu\text{m}$.

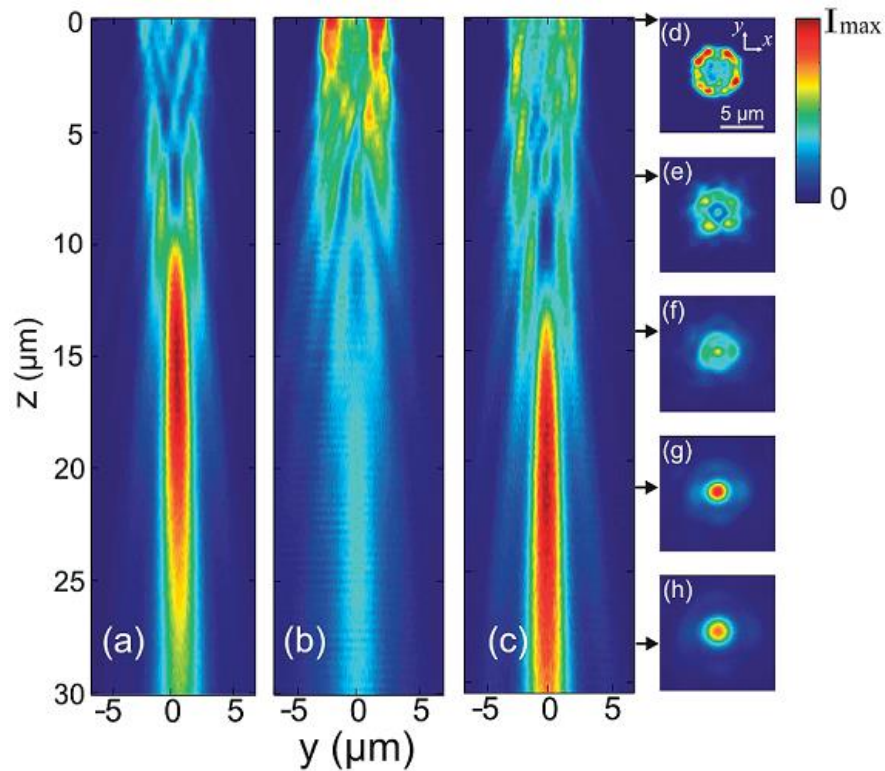


Figure 8.5 Intensity profile of the transmitted light in z direction a) apertures with fixed arm lengths (250 nm) b) designed lens with $f_D=15 \mu\text{m}$ c) designed lens with $f_D=25 \mu\text{m}$ d-h) 2D intensity profile at $z=0, 14, 21,$ and $28 \mu\text{m}$. Reprinted with permission from Ref. [103].

Extending this design methodology to the nonlinear case, the phase of the third order nonlinear signal can be tuned such that it get focused on the desired spot near the close to the surface of the sample. Recently, an effort has been made toward the steering of the focusing and steering of the transmitted four-wave mixing signal.

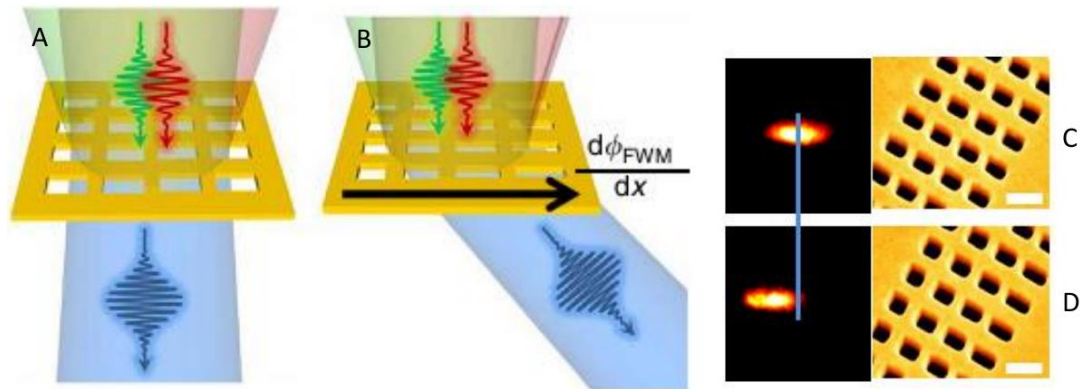


Figure 8.6 A) Schematic diagram of metasurface with a) a uniform unit cell b) phase gradient unit cell. Corresponding observed transmitted light observed on the CCD camera c) uniform unit cell d) phase gradient unit cell. Reprinted with permission from Ref. [104].

Fig. 8.6 is an illustration of metasurfaces for anomalous phase matching (a,b) and CCD images of the corresponding metasurfaces (c,d).

In our laboratory, we initiated the research on TH focusing lens. We applied the same approach similar to the linear case introduced above and performed FDTD simulation to find the optimum length for the rectangular aperture in an array structure. These lenses were designed such that they focus light at the wavelength of 523 nm. However, to achieve efficient TH lenses, further investigation is required.

8.3 TH Focusing Lens

Fig. 8.7 shows the calculated results for the array of rectangular aperture with the periodicity of 400 nm in both x and y directions for an arbitrary focal point. From this figures, it can be seen that the deviation of the length of the aperture at the edge of the array as compared to the length of the center aperture is not considerable. We have not yet experimentally evaluated the quality of the designed lens. Therefore there is a good potential for further research on this topic.

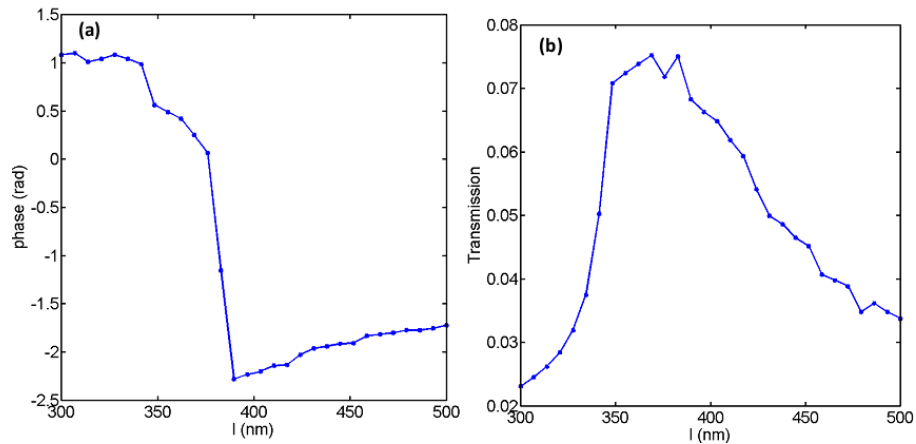


Figure 8.7 a) phase of the transmitted light through a metasurface with rectangular aperture b) corresponding transmission as a function of the aperture length

8.4 TH Wave Plates

We also tried to design metasurface wave plates to manipulate the polarization of the third harmonic signal. Figs. 8.8.a-b show examples of the fabricated structure as TH wave plate. Experiments have not been done yet to analyze the quality of the fabricated structures. This field needs to be explored more. Therefore it could be a suggested future research topic related to our findings in this work.

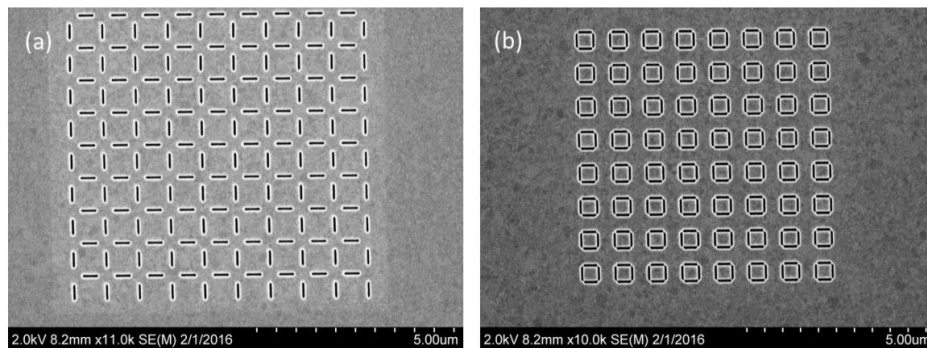


Figure 8.8 SEM images of the fabricated metasurface wave plates to control TH beam polarization.

Conclusion

Aperture-based third harmonic generation can be enhanced by tuning LSP and SPP resonance to the fundamental and harmonic wavelength. Experiments were conducted to study all possible scenarios for the arrays of rectangular aperture. We found that tuning the LSP resonance to the fundamental beam and propagating SPP resonance to the third harmonic beam result in the greatest conversion efficiency. We also investigated the effect of gap plasmon resonance on the THG of the annular ring structure, DNH array, and H-shaped array. Our results showed that the field enhancement in the gap could lead to the even higher conversion efficiencies than the array of rectangular apertures. However, the electron tunneling is a limiting factor in the sub-nanometer regime. Using modified quantum-corrected model, we previously investigated this quantum effect on THG. Moreover, we proved that the maximum THG does not result from the smallest gap, however, matching the absorption and scattering cross sections lead to the enhanced THG. This is very similar to the fundamental circuit theory of impedance matching of a source and load for the maximum power delivery from the source to the load. We also performed FDTD simulations based on the nonlinear scattering theory that supports our findings. To achieve higher conversion efficiencies, other parameters such as film thickness, aperture shape, materials (considering optical, nonlinear and thermal characteristics), and structure (e.g., adding encapsulation to help stabilize the structure and manage thermal damage), should be explored. Another interesting topic for future research related to this thesis is the design and fabrication of the TH focusing lens and wave plates.

Appendix A: Focused Ion Beam Milling Parameters

Table A-1 Milling Parameters for Fabrication of Single Apertures

Magnification	80,000×
Fabrication area	1.9×1.9 μm^2
Electron beam current	0.01064
Dwell time	10 μs
Number of beam passes	10

Table A-2 Milling Parameters for Fabrication of Aperture Arrays

Magnification	18,000×
Fabrication area	8.1×8.1 μm^2
Electron beam current	0.01064
Dwell time	10 μs
Number of beam passes	150

Appendix B:Lumerical FDTD Simulation Parameters

Table B-1 FDTD simulation parameters for a 60 nm nanosphere on the gold surface

Software	Lumerical FDTD Solutions 8.6.3
Source type	Plane
Polarization	TM
Angle of incidence	50°
Boundary condition	PML
Mesh size	0.3 nm in the gap region 5 nm over the nanosphere particle
Mesh technology	Conformal mesh 1

Table B-2 FDTD simulation parameters for aperture arrays

Software	Lumerical FDTD Solutions 8.12.501
Source type	Plane
Polarization	TM
Angle of incidence	Normal
Boundary condition	asymmetric in the direction of polarization symmetric perpendicular to the direction of polarization
Mesh size	1 nm over the aperture area
Mesh technology	Conformal mesh 1

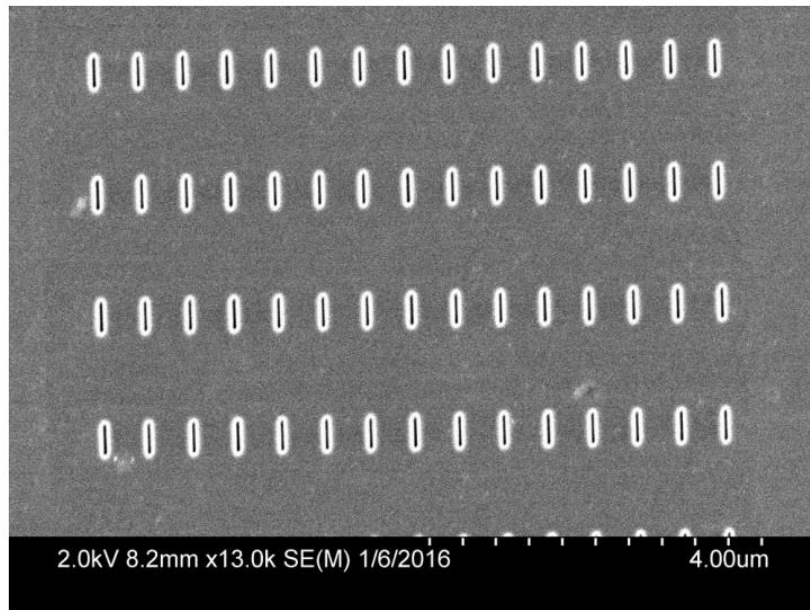
Appendix C: Template Stripping For Sub-10 nm Gap Aperture Arrays

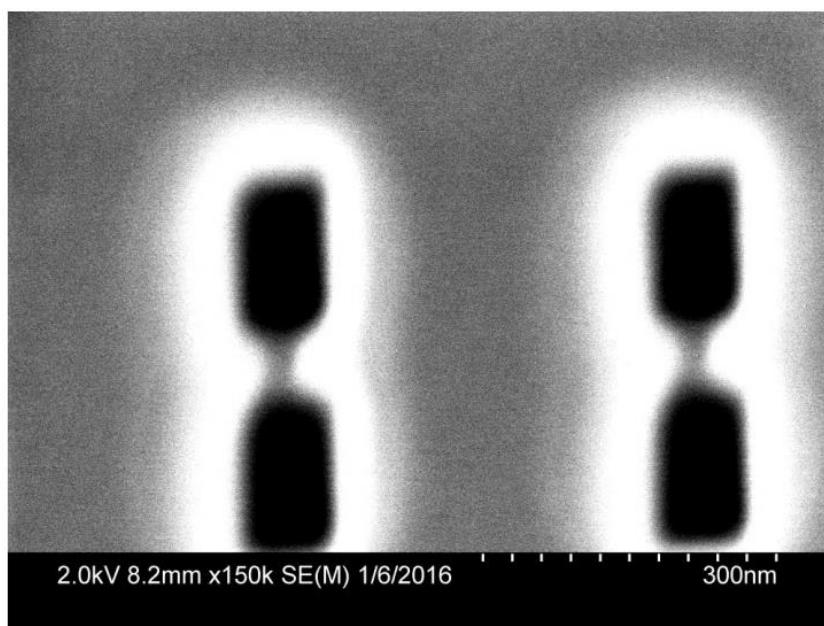
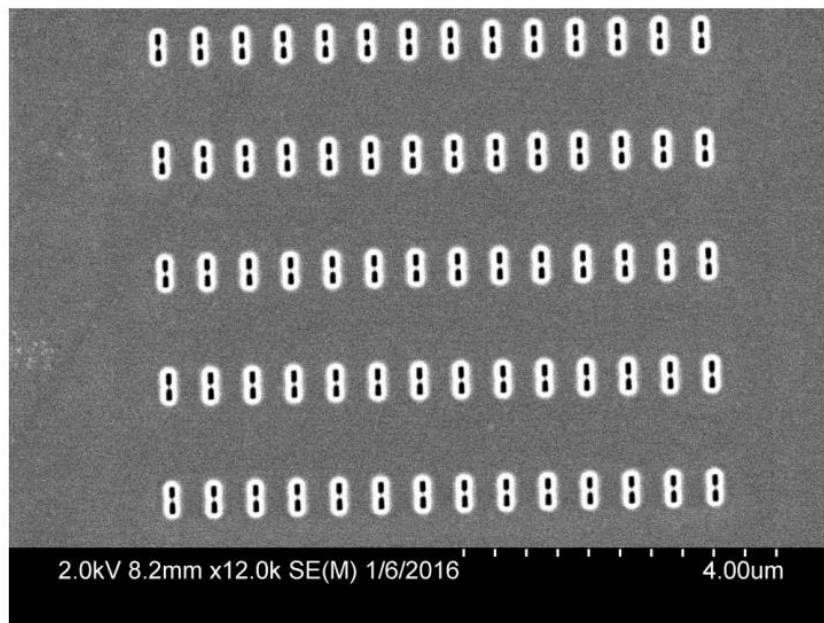
C.1 Silicon Templates SEM Characterization

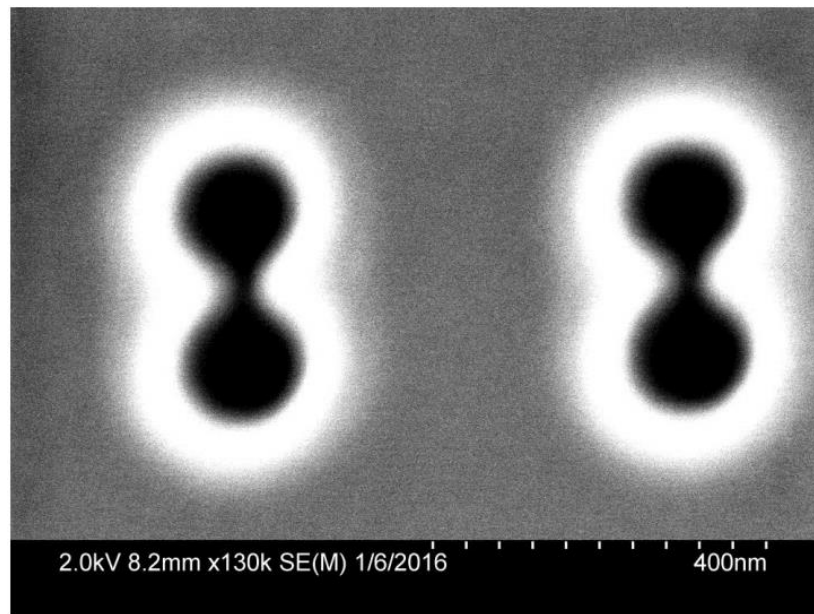
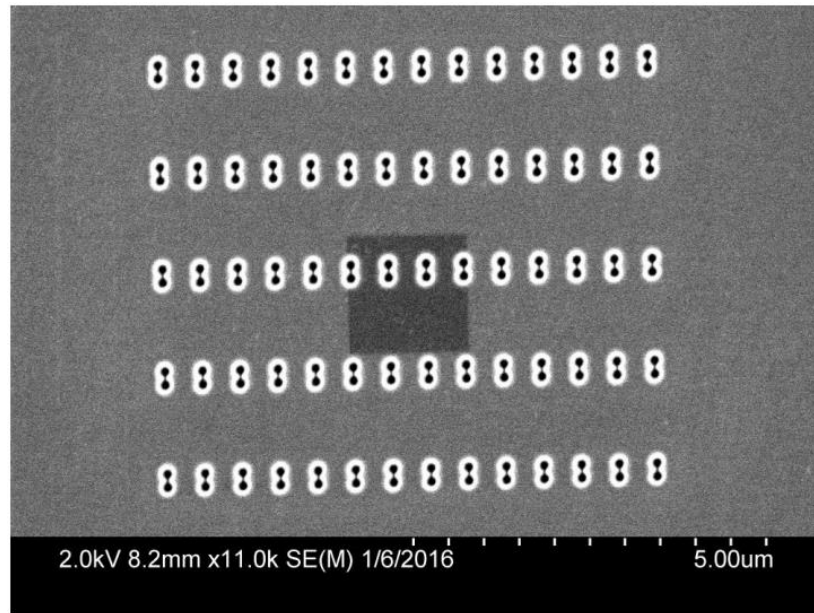
This appendix presents examples of SEM image of the silicon templates and the resulted template-stripped aperture arrays. The process of the template-stripping as a high throughput fabrication method is discussed in Chapter 3.

C.1.1 Normal images

The SEM images of the fabricated silicon templates at a normal angle:

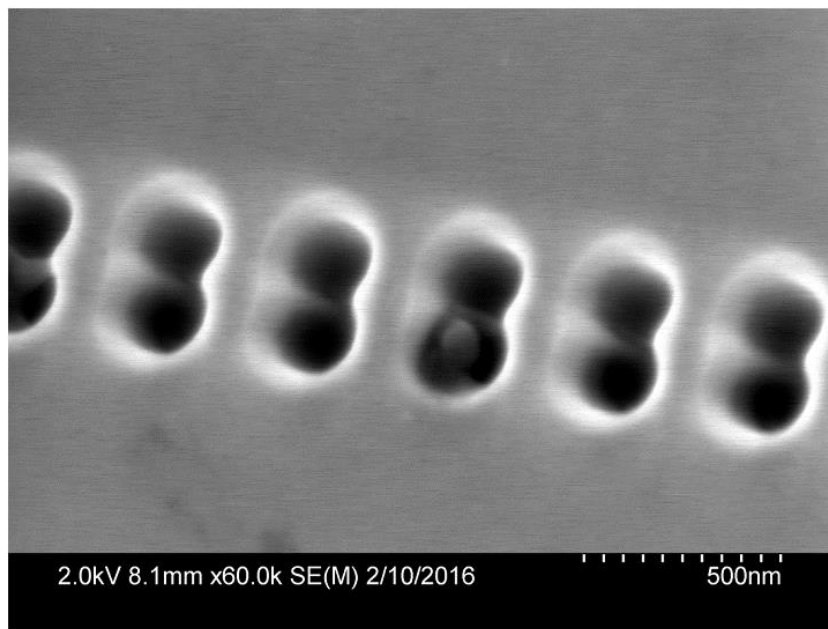
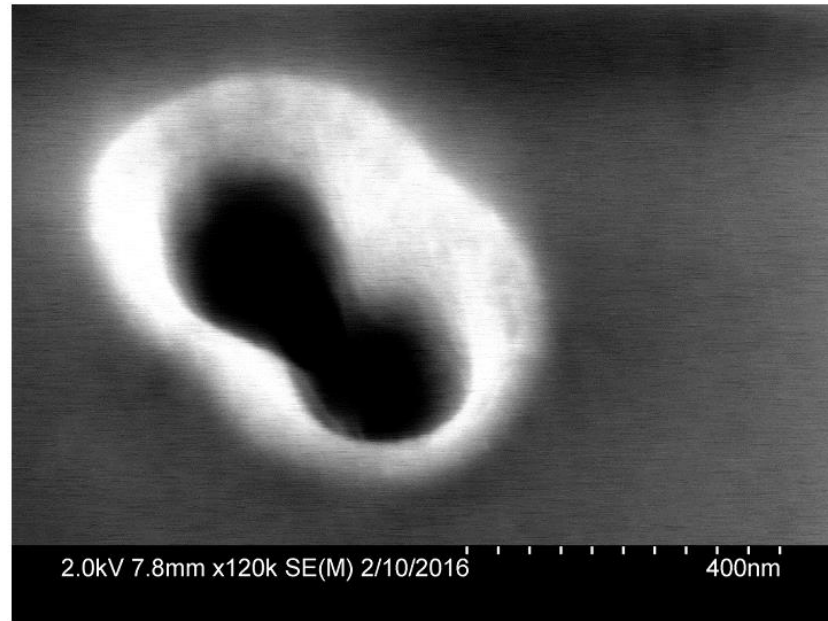






C.1.2 Tilted Images for Depth Estimation

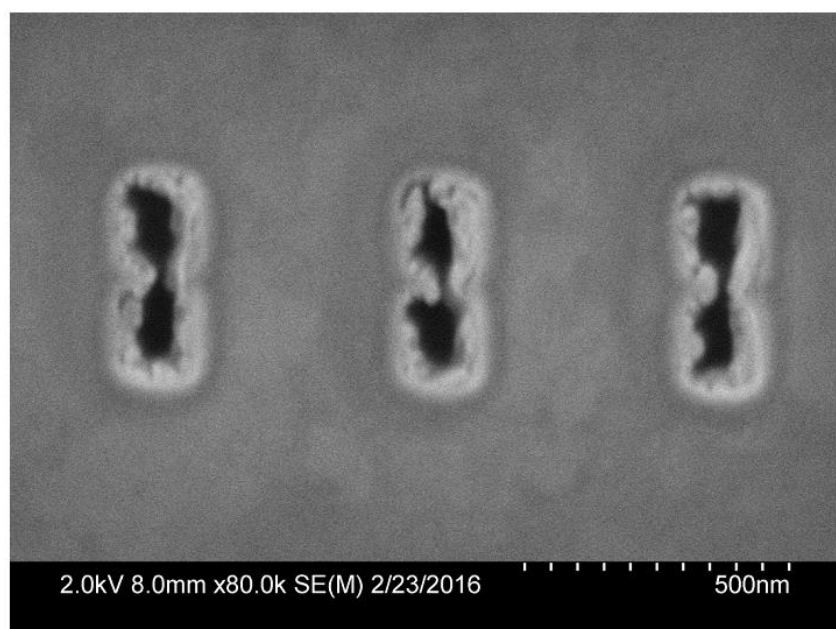
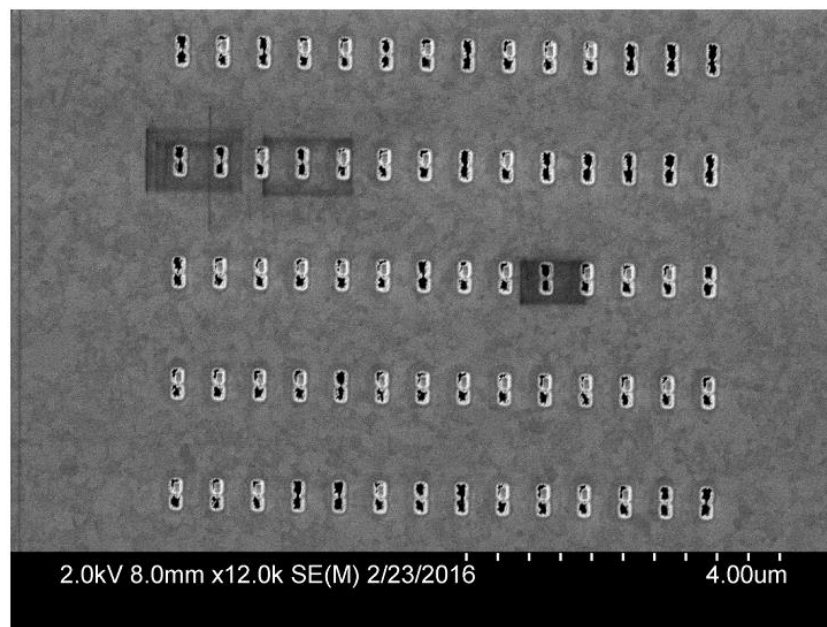
The SEM images of the silicon templates at an angle of 30 degrees to estimate the depth of the milled apertures before the gold deposition process. This need to be done to assure the depth is less than the desired deposited gold film to prevent connection.

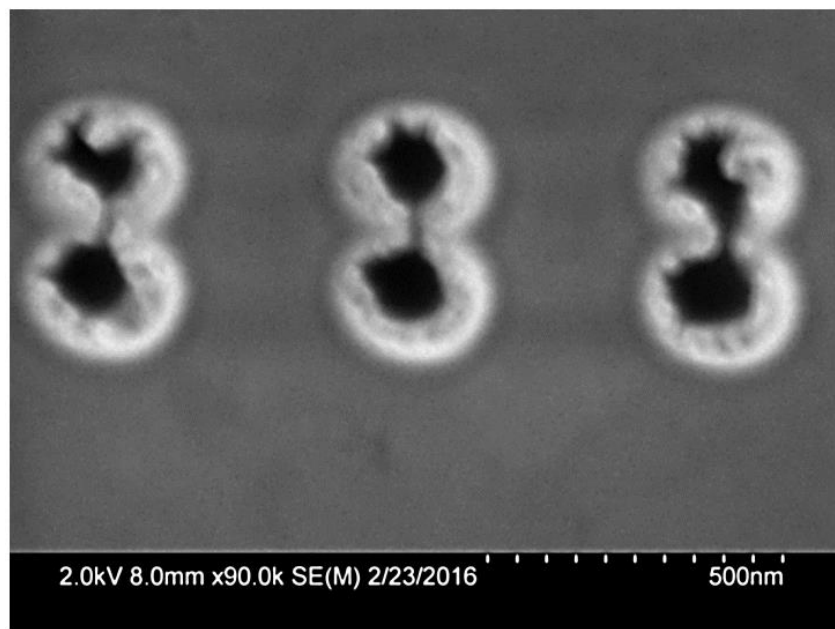
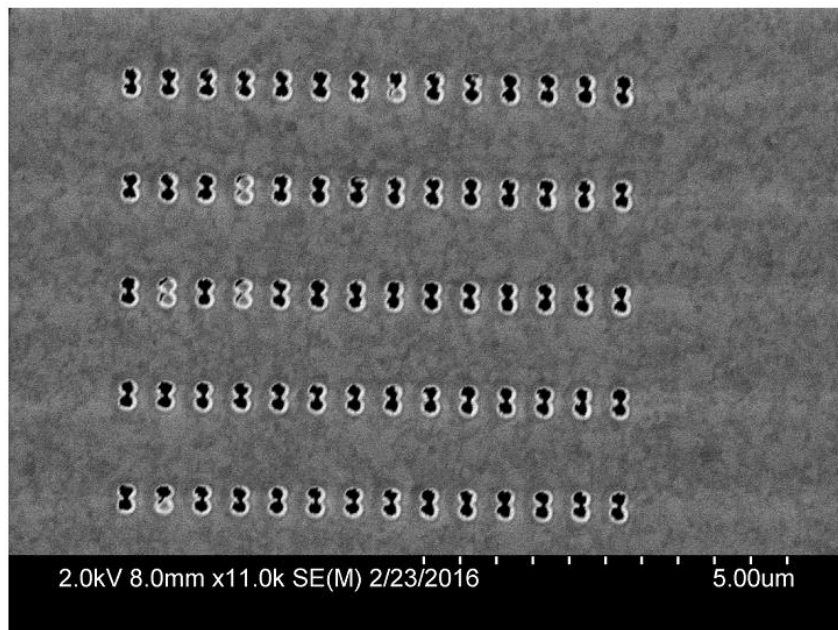


C.2 Template Stripped Structure SEM Images

The SEM images of the templates-stripped aperture arrays are provided in this section. The nominal thickness of evaporated gold was 100 nm. However, we utilized ellipsometry to measure the thickness of the gold film after evaporation. The measured

thickness of deposited gold was 114.45 ± 5.45 nm. The measured surface roughness was 0.50 nm.





Appendix D: THG Enhancement by Nano-apertures

D.1 Introduction

This appendix briefly explains one of our previous works that has been done in aperture-based THG. The effects of the lattice arrangement, the angle of incidence and the aperture size on the aperture-based THG have been investigated by Xu et al. [33].

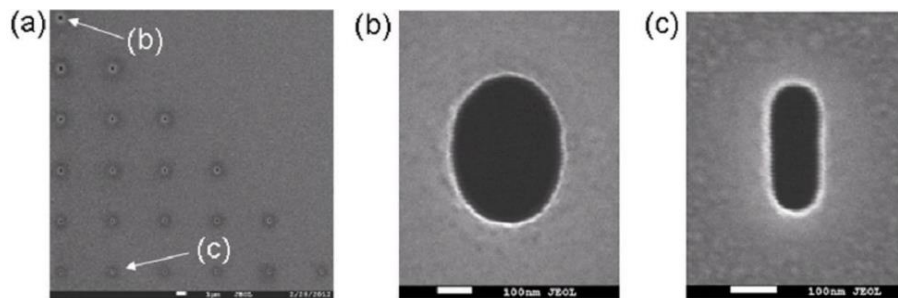


Figure D.1 The SEM images of the fabricated structures in the gold and aluminum thin films. Aluminum shows better performance regarding THG at $1.57 \mu\text{m}$. Reprinted with permission from Ref. [19].

Fig. D.1 show the SEM images of the fabricated structures in the gold and aluminum thin films. The same group has also reported a third harmonic conversion efficiency of 10^{-5} for the split hole resonator (SHR) perforated in the aluminum thin film [20]. They have measured the third harmonic signal at the fundamental wavelength of 1560 nm at the normal incidence. Fig. D.2.a shows the SEM image of the fabricated SHR in the aluminum thin film. Fig. D.2.b shows the spatial electric field distribution inside the SHR at the fundamental wavelength of 1560 nm. Fig. D.2.c shows the captured TH image from the CCD camera and Fig. D.2.d shows the measured emitted TH signal.

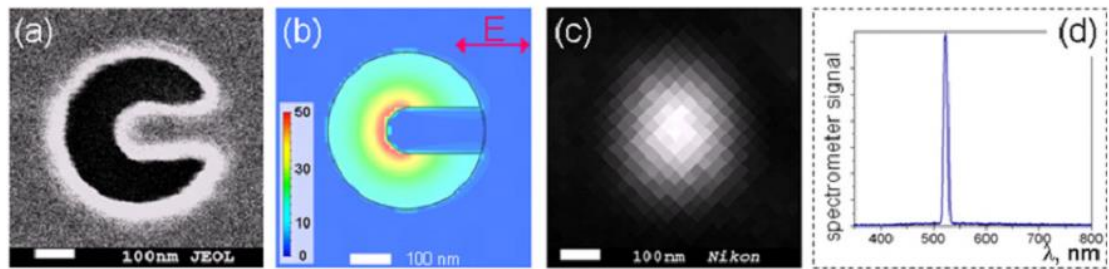


Figure D.2 a) The SEM image of fabricated SHR in an aluminum thin film b) the spatial electric field distribution in the aperture at the fundamental wavelength of 1560 nm c) the captured third harmonic signal on the CCD d) The measured third harmonic signal on the spectrometer. The conversion efficiency is around 10^{-5} . Reprinted with permission from Ref. [20].

D.2 The Single Aperture THG

We performed THG measurement for single apertures such as SHR and DNH on a gold thin film. Our results showed that DNH is a promising structure for THG. Fig. D.3.a shows the THG spectra for different radius and the spacing of the DNH for the fundamental of 1570 nm. Fig. D.3.b shows the same spectra for a single SHR for different diameter of the aperture and the nanorod length. Considering the aperture area, a single DNH conversion efficiency is more than its SHR counterpart.

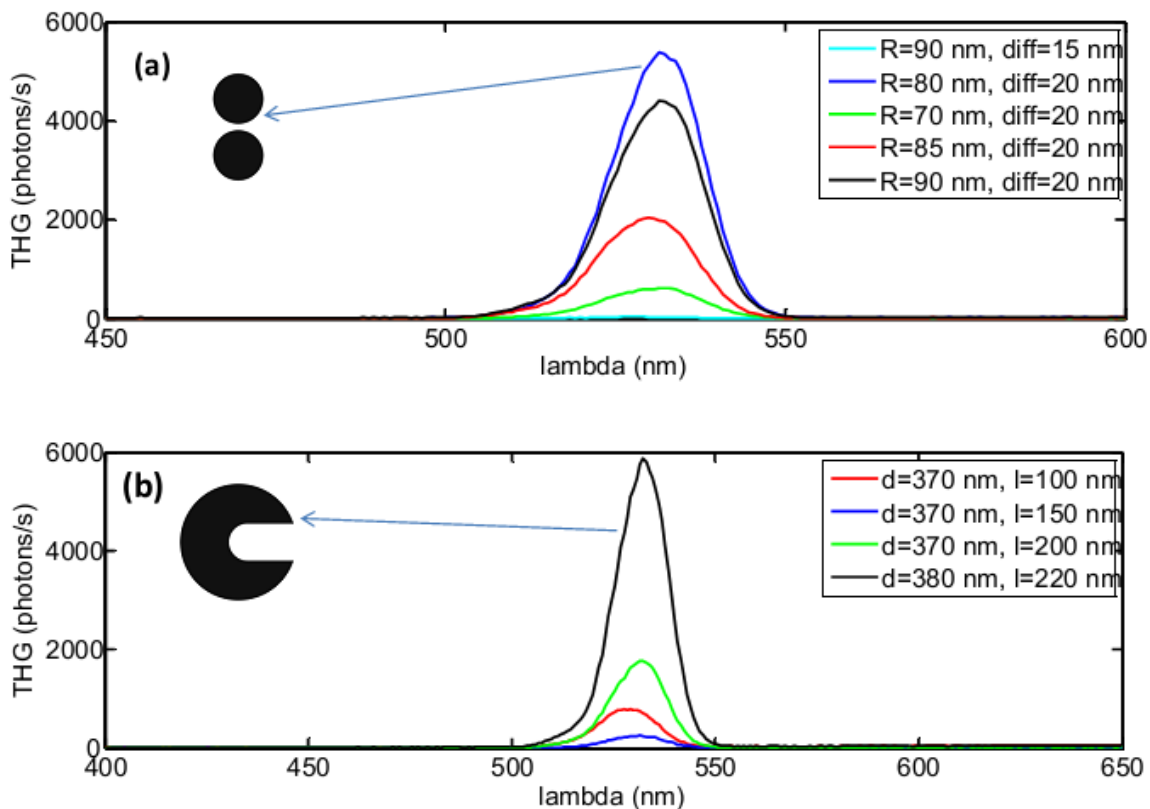


Figure D.3 a) THG spectra of a single double nanohole as a function of the hole radius and the spacing between two holes b) THG spectra of a single SHR as a function of the nanorod length and the diameter of the hole. The scaled version of the structures has been shown in the plots.

Related to the point, we also performed THG measurement for single template-stripped double nanoholes (DNH). The results did not show greater THG as compared to the normal DNH structures in Fig. D.4.

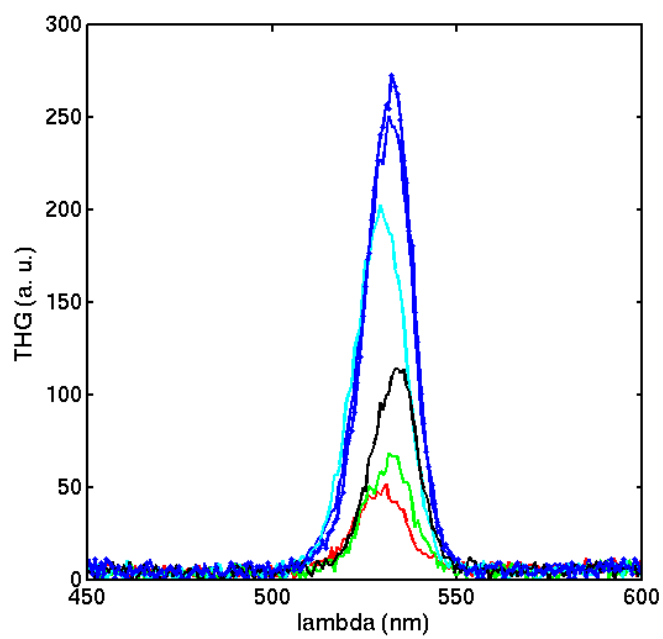


Figure D.4 THG spectra of different template-stripped single DNH aperture with sub 20 nm gaps

Publications and Contributions:

1. **M. S. Nezami**, D. Yoo, G. Hajisalem, S. -H. Oh, R. Gordon, "Gap plasmon enhanced metasurface third harmonic generation in transmission geometry." ACS Photonics (2016)
2. **M. S. Nezami** and R. Gordon, "Localized and propagating surface plasmon resonances in aperture-based third harmonic generation." Optics Express, 23(25), 32006-32014 (2015).
3. G. Hajisalem, **M. S. Nezami**, and R. Gordon. "Probing the quantum tunneling limit of plasmonic enhancement by third harmonic generation." Nano Letters 14(11), 6651-6654 (2014).

References

-
- [1] Yu, N.; Capasso, F. Flat Optics with Designer Metasurfaces. *Nature Materials* 2014, 13 (2), 139–150.
- [2] Ebbesen, T. W.; Lezec, H. J.; Ghaemi, H. F.; Thio, T.; Wolff, P. A. Extraordinary Optical Transmission through Sub-Wavelength Hole Arrays. *Nature* 1998, 391 (6668), 667–669.
- [3] Alali, F.; Kim, Y. H.; Baev, A.; Furlani, E. P. Plasmon-Enhanced Metasurfaces for Controlling Optical Polarization. *ACS Photonics* 2014, 1, 507–515.
- [4] Chen, C.-F.; Ku, C.-T.; Tai, Y.-H.; Wei, P.-K.; Lin, H.-N.; Huang, C.-B. Creating Optical Near-Field Orbital Angular Momentum in a Gold Metasurface. *Nano Letters* 2015, 15, 2746–2750.
- [5] Yao, Y.; Shankar, R.; Kats, M. A.; Song, Y.; Kong, J.; Loncar, M.; Capasso, F. Electrically Tunable Metasurface Perfect Absorbers for Ultrathin Mid-Infrared Optical Modulators. *Nano Letters* 2014, 14, 6526–6532.
- [6] Michel, A.-K. U.; Zalden, P.; Chigrin, D. N.; Wuttig, M.; Lindenberg, A. M.; Taubner, T. Reversible Optical Switching of Infrared Antenna Resonances with Ultrathin Phase-Change Layers Using Femtosecond Laser Pulses. *ACS Photonics* 2014, 1, 833–839.
- [7] Yu, N.; Capasso, F. Optical Metasurfaces and Prospect of Their Applications Including Fiber Optics. *Journal of Lightwave Technology* 2015, 33, 2344–2358.
- [8] Yu, N.; Capasso, F. Flat Optics with Designer Metasurfaces. *Nature Material* 2014, 13, 139–150.
- [9] Kauranen, M.; Zayats, A. V. Nonlinear Plasmonics. *Nature Photonics* 2012, 6, 737–748.
- [10] Lapine, M.; Shadrivov, I. V.; Kivshar, Y. S. Colloquium: Nonlinear Metamaterials. *Reviews of Modern Physics* 2014, 86, 1093.
- [11] Min, C.; Wang, P.; Chen, C.; Deng, Y.; Lu, Y.; Ming, H.; Ning, T.; Zhou, Y.; Yang, G. All-Optical Switching in Subwavelength Metallic Grating Structure Containing Nonlinear Optical Materials. *Optics Letters* 2008, 33, 869–871.

-
- [12] Ren, M.; Jia, B.; Ou, J.-Y.; Plum, E.; Zhang, J.; MacDonald, K. F.; Nikolaenko, A. E.; Xu, J.; Gu, M.; Zheludev, N. I. Nanostructured Plasmonic Medium for Terahertz Bandwidth All-Optical Switching. *Advanced Materials* 2011, 23, 5540–5544.
- [13] Nahata, A.; Linke, R. A.; Ishi, T.; Ohashi, K. Enhanced Nonlinear Optical Conversion from a Periodically Nanostructured Metal Film. *Optics Letters* 2003, 28, 423–425.
- [14] Palomba, S.; Novotny, L. Near-Field Imaging with a Localized Nonlinear Light Source. *Nano Letters* 2009, 9, 3801–3804.
- [15] Chen, P.-Y.; Alù, A. Subwavelength Imaging Using Phase-Conjugating Nonlinear Nanoantenna Arrays. *Nano Letters* 2011, 11, 5514–5518.
- [16] Zhu, W.; Banaee, M. G.; Wang, D.; Chu, Y.; Crozier, K. B. Lithographically Fabricated Optical Antennas with Gaps Well Below 10 nm. *Small* 2011, 7, 1761–1766.
- [17] Kim, E.; Wang, F.; Wu, W.; Yu, Z.; Shen, Y. R. Nonlinear Optical Spectroscopy of Photonic Metamaterials. *Physical Review B* 2008, 78, 113102.
- [18] Thio, T.; Lezec, H. J.; Ebbesen, T. W.; Pellerin, K. M.; Lewen, G. D.; Nahata, A.; Linke, R. A. Giant Optical Transmission of Sub-Wavelength Apertures: Physics and Applications. *Nanotechnology* 2002, 13, 429.
- [19] Melentiev, P. N.; Konstantinova, T. V.; Afanasiev, A. E.; Kuzin, A. A.; Baturin, A. S.; Tausenev, A. V.; Konyaschenko, A. V.; Balykin, V. I. Single Nano-Hole as a New Effective Nonlinear Element for Third-Harmonic Generation. *Laser Physics Letters* 2013, 10, 075901.
- [20] Melentiev, P. N.; Afanasiev, A. E.; Kuzin, A. A.; Baturin, A. S.; Balykin, V. I. Giant Optical Nonlinearity of a Single Plasmonic Nanostructure. *Optics Express* 2013, 21, 13896–13905.
- [21] Aouani, H.; Rahmani, M.; Navarro-Cía, M.; Maier, S. A. Third-Harmonic-Upconversion Enhancement from a Single Semiconductor Nanoparticle Coupled to a Plasmonic Antenna. *Nature Nanotechnology* 2014, 9, 290–294.
- [22] Lesuffleur, A.; Kumar, L. K. S.; Gordon, R. Apex-Enhanced Second-Harmonic Generation by Using Double-Hole Arrays in a Gold Film. *Physical Review B* 2007, 75, 045423.
- [23] Canfield, B. K.; Husu, H.; Laukkanen, J.; Bai, B.; Kuittinen, M.; Turunen, J.; Kauranen, M. Local Field Asymmetry Drives Second-Harmonic Generation in Noncentrosymmetric Nanodimers. *Nano Letters* 2007, 7, 1251–1255.

-
- [24] Van Nieuwstadt, J. A. H.; Sandtke, M.; Harmsen, R. H.; Segerink, F. B.; Prangma, J. C.; Enoch, S.; Kuipers, L. Strong Modification of the Nonlinear Optical Response of Metallic Subwavelength Hole Arrays. *Physical Review Letters* 2006, 97, 146102.
- [25] Wang, B.-L.; Wang, R.; Liu, R. J.; Lu, X. H.; Zhao, J.; Li, Z.-Y. Origin of Shape Resonance in Second-Harmonic Generation from Metallic Nanohole Arrays. *Scientific Reports* 2013, 3.
- [26] Fan, W.; Zhang, S.; Malloy, K. J.; Brueck, S. R. J.; Panoiu, N. C.; Osgood, R. M. Second Harmonic Generation from Patterned GaAs inside a Subwavelength Metallic Hole Array. *Optics Express* 2006, 14, 9570–9575.
- [27] Barakat, E. H.; Bernal, M.-P.; Baida, F. I. Second Harmonic Generation Enhancement by Use of Annular Aperture Arrays Embedded into Silver and Filled by Lithium Niobate. *Optics Express* 2010, 18, 6530-6536.
- [28] Simon, H. J.; Mitchell, D. E.; Watson, J. G. Optical Second-Harmonic Generation with Surface Plasmons in Silver Films. *Physical Review Letters* 1974, 33, 1531–1534.
- [29] Agarwal, G. S.; Jha, S. S. Theory of Second Harmonic Generation at a Metal Surface with Surface Plasmon Excitation. *Solid State Communications* 1982, 41, 499–501.
- [30] Renger, J.; Quidant, R.; van Hulst, N.; Novotny, L. Surface-Enhanced Nonlinear Four-Wave Mixing. *Physical Review Letters* 2010, 104, 046803.
- [31] Xu, T.; Jiao, X.; Zhang, G.-P.; Blair, S. Second-Harmonic Emission from Sub-Wavelength Apertures: Effects of Aperture Symmetry and Lattice Arrangement. *Optics Express* 2007, 15, 13894-13906.
- [32] Airola, M.; Liu, Y.; Blair, S. Second-Harmonic Generation from an Array of Sub-Wavelength Metal Apertures. *Journal of Optics A Pure and Applied Optics* 2005, 7, S118.
- [33] Xu, T.; Jiao, X.; Blair, S. Third-Harmonic Generation from Arrays of Sub-Wavelength Metal Apertures. *Optics Express* 2009, 17, 23582-23588.
- [34] Ko, K. D.; Kumar, A.; Fung, K. H.; Ambekar, R.; Liu, G. L.; Fang, N. X.; Toussaint, K. C. Nonlinear Optical Response from Arrays of Au Bowtie Nanoantennas. *Nano Letters* 2011, 11, 61–65.
- [35] Rodrigo, S. G.; Laliena, V.; Martín-Moreno, L. Second-Harmonic Generation from Metallic Arrays of Rectangular Holes. *Journal of Optical Society of America B* 2015, 32, 15-25.

-
- [36] Wellershoff, S. S.; Gudde, J.; Hohlfeld, J.; Muller, J. G.; Matthias, E. Role of Electron-Phonon Coupling in Femtosecond Laser Damage of Metals. *High-Power Laser Ablation*, 1998, pp 378–387.
- [37] Wang, B.; Gallais, L. A Theoretical Investigation of the Laser Damage Threshold of Metal Multi-Dielectric Mirrors for High Power Ultrashort Applications. *Optics Express* 2013, 21, 14698-14711.
- [38] Beermann, J.; Eriksen, R. L.; Holmgaard, T.; Pedersen, K.; Bozhevolnyi, S. I. Plasmonic Black Metals via Radiation Absorption by Two-Dimensional Arrays of Ultra-Sharp Convex Grooves. *Scientific Reports* 2014, 4, 6904.
- [39] Fedotov, A. B.; Koroteev, N. I.; Loy, M. M. T.; Xiao, X.; Zheltikov, A. M. Saturation of Third-Harmonic Generation in a Plasma of Self-Induced Optical Breakdown due to the Self-Action of 80-Fs Light Pulses. *Optics Communications* 1997, 133, 587–595.
- [40] Sundaramurthy, A.; Crozier, K. B.; Kino, G. S.; Fromm, D. P.; Schuck, P. J.; Moerner, W. E. Field Enhancement and Gap-Dependent Resonance in a System of Two Opposing Tip-to-Tip Au Nanotriangles. *Physical Review B* 2005, 72, 165409.
- [41] Suh, J. Y.; Huntington, M. D.; Kim, C. H.; Zhou, W.; Wasielewski, M. R.; Odom, T. W. Extraordinary Nonlinear Absorption in 3D Bowtie Nanoantennas. *Nano Letters* 2012, 12, 269–274.
- [42] Suh, J. Y.; Odom, T. W. Nonlinear Properties of Nanoscale Antennas. *Nano Today* 2013, 8, 469–479.
- [43] Boyd, R. W. *Nonlinear Optics*; Academic Press, 2003.
- [44] Hajisalem, G.; Hore, D. K.; Gordon, R. Interband Transition Enhanced Third Harmonic Generation from Nanoplasmonic Gold. *Optical Materials Express* 2015, 5, 2217–2224.
- [45] Gong, Y.; Li, Z.; Fu, J.; Chen, Y.; Wang, G.; Lu, H.; Wang, L.; Liu, X. Highly Flexible All-Optical Metamaterial Absorption Switching Assisted by Kerr-Nonlinear Effect. *Optics Express* 2011, 19, 10193–10198.
- [46] Sidiropoulos, T. P. H.; Nielsen, M. P.; Roschuk, T. R.; Zayats, A. V.; Maier, S. A.; Oulton, R. F. Compact Optical Antenna Coupler for Silicon Photonics Characterized by Third-Harmonic Generation. *ACS Photonics* 2014, 1, 912–916.
- [47] Barnes, W. L.; Dereux, A.; Ebbesen, T. W. Surface Plasmon Subwavelength Optics. *Nature* 2003, 424 (6950), 824–830.

-
- [48] Juan, M. L.; Righini, M.; Quidant, R. Plasmon Nano-Optical Tweezers. *Nature Photonics* 2011, 5 (6), 349–356.
- [49] Maier, Stefan Alexander. Plasmonics: fundamentals and applications. *Springer Science & Business Media*, 2007.
- [50] Gordon, R.; Brolo, A. G. Increased Cut-off Wavelength for a Subwavelength Hole in a Real Metal. *Optics Express* 2005, 13 (6), 1933-1938.
- [51] García-Vidal, F. J.; Moreno, E.; Porto, J. A.; Martín-Moreno, L. Transmission of Light through a Single Rectangular Hole. *Physical Review Letters* 2005, 95 (10), 103901.
- [52] Gordon, R.; Kumar, L. K. S.; Brolo, A. G. Resonant Light Transmission through a Nanohole in a Metal Film. *IEEE Transactions on Nanotechnology* 2006, 5 (3), 291–294.
- [53] Bethe, H. A. Theory of diffraction by small holes. *Physical Review* 1944, 66, 163–182.
- [54] Griffiths, David J. Introduction to Quantum Mechanics (2nd ed.). *Prentice Hall*, 2004.
- [55] Giannuzzi, Lucille A., ed. Introduction to focused ion beams: instrumentation, theory, techniques and practice. *Springer Science & Business Media*, 2006.
- [56] Mohammad, M. A.; Muhammad, M.; Dew, S. K.; Stepanova, M. Fundamentals of Electron Beam Exposure and Development; *Springer*, 2012.
- [57] Yoo, D.; Nguyen, N.-C.; Martin-Moreno, L.; Mohr, D. A.; Carretero-Palacios, S.; Shaver, J.; Péraire, J.; Ebbesen, T. W.; Oh, S.-H. High-Throughput Fabrication of Resonant Metamaterials with Ultrasmall Coaxial Apertures via Atomic Layer Lithography. *Nano Letters* 2016, 16 (3), 2040–2046.
- [58] Vogel, N.; Zieleniecki, J.; Köper, I. As Flat as It Gets: Ultrasoother Surfaces from Template-Stripping Procedures. *Nanoscale* 2012, 4 (13), 3820.
- [59] “Let’s Familiarize Ourselves With the SEM” by Hitachi.
- [60] <http://www.uvic.ca/research/advancedmicroscopy/about/microscopes/>, Advanced Microscopy Facility, University of Victoria,
- [61] Aouani, H.; Rahmani, M.; Navarro-Cía, M.; Maier, S. A. Third-Harmonic-Upconversion Enhancement from a Single Semiconductor Nanoparticle Coupled to a Plasmonic Antenna. *Nature Nanotechnology* 2014, 9 (4), 290–294.

-
- [62] Miller, R. C. OPTICAL SECOND HARMONIC GENERATION IN PIEZOELECTRIC CRYSTALS. *Applied Physics Letters* 1964, 5 (1), 17.
- [63] Metzger, B.; Hentschel, M.; Lippitz, M.; Giessen, H. Third-Harmonic Spectroscopy and Modeling of the Nonlinear Response of Plasmonic Nanoantennas. *Optics Letters* 2012, 37 (22), 4741.
- [64] Hentschel, M.; Utikal, T.; Giessen, H.; Lippitz, M. Quantitative Modeling of the Third Harmonic Emission Spectrum of Plasmonic Nanoantennas. *Nano Letters* **2012**, 12 (7), 3778–3782.
- [65] Metzger, B.; Hentschel, M.; Schumacher, T.; Lippitz, M.; Ye, X.; Murray, C. B.; Knabe, B.; Buse, K.; Giessen, H. Doubling the Efficiency of Third Harmonic Generation by Positioning ITO Nanocrystals into the Hot-Spot of Plasmonic Gap-Antennas. *Nano Letters* 2014, 14 (5), 2867–2872.
- [66] Butet, J.; Martin, O. J. F. Evaluation of the Nonlinear Response of Plasmonic Metasurfaces: Miller’s Rule, Nonlinear Effective Susceptibility Method, and Full-Wave Computation. *Journal of the Optical Society of America B* 2016, 33 (2), A8.
- [67] O’Brien, K.; Suchowski, H.; Rho, J.; Salandrino, A.; Kante, B.; Yin, X.; Zhang, X. Predicting Nonlinear Properties of Metamaterials from the Linear Response. *Nature Materials* 2015, 14, 379–383.
- [68] J. D. Jackson, Classical Electrodynamics 3rd edition, *John Wiley and Sons Inc.*, 1998, 392-394.
- [69] Roke, S.; Bonn, M.; Petukhov, A. V. Nonlinear Optical Scattering: The Concept of Effective Susceptibility. *Physical Review B* 2004, 70, 115106.
- [70] de Beer, A. G.; Roke, S. Nonlinear Mie Theory for Second-Harmonic and Sum-Frequency Scattering. *Physical Review B* 2009, 79, 155420.
- [71] Chi, Y.; Chen, G.; Jelezko, F.; Wu, E.; Zeng, H. Enhanced Photoluminescence of Single-Photon Emitters in Nanodiamonds on a Gold Film. *IEEE Photonics Technology Letters* 2011, 23 (6), 374–376.
- [72] Knittel, V.; Fischer, M. P.; de Roo, T.; Mecking, S.; Leitenstorfer, A.; Brida, D. Nonlinear Photoluminescence Spectrum of Single Gold Nanostructures. *ACS Nano* 2015, 9 (1), 894–900.
- [73] García-Vidal, F. J.; Martín-Moreno, L.; Moreno, E.; Kumar, L. K. S.; Gordon, R. Transmission of Light through a Single Rectangular Hole in a Real Metal. *Physical Review B* 2006, 74 (15), 153411.

-
- [74] Ruan, Z.; Fan, S. Superscattering of Light from Subwavelength Nanostructures. *Physical Review Letters* 2010, 105 (1), 013901.
- [75] Chen, S.; Jin, S.; Gordon, R. Super-Transmission from a Finite Subwavelength Arrangement of Slits in a Metal Film. *Optics Express* 2014, 22 (11), 13418.
- [76] Tribelsky, M. I.; Luk'yanchuk, B. S. Anomalous Light Scattering by Small Particles. *Physical Review Letters* 2006, 97 (26), 263902.
- [77] Bardhan, R.; Mukherjee, S.; Mirin, N. A.; Levit, S. D.; Nordlander, P.; Halas, N. J. Nanosphere-in-a-Nanoshell: A Simple Nanomaterial. *The Journal of Physical Chemistry C* 2010, 114 (16), 7378–7383.
- [78] Miroschnichenko, A. E. Non-Rayleigh Limit of the Lorenz-Mie Solution and Suppression of Scattering by Spheres of Negative Refractive Index. *Physical Review A* 2009, 80 (1), 013808.
- [79] Schuller, J. A.; Taubner, T.; Brongersma, M. L. Optical Antenna Thermal Emitters. *Nature Photonics* 2009, 3 (11), 658–661.
- [80] Aizpurua, J.; Hanarp, P.; Sutherland, D. S.; Käll, M.; Bryant, G. W.; García de Abajo, F. J. Optical Properties of Gold Nanorings. *Physical Review Letters* 2003, 90 (5), 057401.
- [81] Klein, M. W.; Wegener, M.; Feth, N.; Linden, S. Experiments on Second- and Third-Harmonic Generation from Magnetic Metamaterials. *Optics Express* 2007, 15 (8), 5238.
- [82] Kalhor, N.; Boden, S. A.; Mizuta, H. Sub-10nm Patterning by Focused He-Ion Beam Milling for Fabrication of Downscaled Graphene Nano Devices. *Microelectronic Engineering* 2014, 114, 70–77.
- [83] Chen, X.; Ciraci, C.; Smith, D. R.; Oh, S.-H. Nanogap-Enhanced Infrared Spectroscopy with Template-Stripped Wafer-Scale Arrays of Buried Plasmonic Cavities. *Nano Letters* 2015, 15 (1), 107–113.
- [84] Stosch, R.; Yaghobian, F.; Weimann, T.; Brown, R. J. C.; Milton, M. J. T.; Güttler, B. Lithographical Gap-Size Engineered Nanoarrays for Surface-Enhanced Raman Probing of Biomarkers. *Nanotechnology* 2011, 22 (10), 105303.
- [85] Zehtabi-Oskuie, A.; Zinck, A. A.; Gelfand, R. M.; Gordon, R. Template Stripped Double Nanohole in a Gold Film for Nano-Optical Tweezers. *Nanotechnology* 2014, 25 (49), 495301.

-
- [86] Savage, K. J.; Hawkeye, M. M.; Esteban, R.; Borisov, A. G.; Aizpurua, J.; Baumberg, J. J. *Nature* 2012, 491, 574-577.
- [87] Esteban, R.; Borisov, A. G.; Nordlander, P.; Aizpurua, J. *Nature Communications* 2012, 3, 825.
- [88] Bardeen, J. *Physical Review Letters* 1962, 4, 147.
- [89] Wang, W.; Lee, T.; Reed, M. A. *Physical Review B* 2003, 68, 035416.
- [90] Esteban, R.; Borisov, A. G.; Nordlander, P.; Aizpurua, J. Bridging Quantum and Classical Plasmonics with a Quantum-Corrected Model. *Nature Communications* 2012, 3, 825.
- [91] Ordal, M. A.; Bell, R. J.; Alexander Jr, R.; Long, L.; Querry, M. *Applied Optics* 1985, 24, 4493-4499.
- [92] Corcoran, B.; Monat, C.; Grillet, C.; Moss, D. J.; Eggleton, B. J.; White, T. P.; O’Faolain, L.; Krauss, T. F. Green Light Emission in Silicon through Slow-Light Enhanced Third-Harmonic Generation in Photonic-Crystal Waveguides. *Nature Photonics* 2009, 3 (4), 206–210.
- [93] Boyd, R. W.; Shi, Z.; De Leon, I. *Optics Communications* 2014, 74-79.
- [94] Johnson, P. B.; Christy, R. *Physical Review B* 1972, 12, 4370.
- [95] Hajisalem, G.; Nezami, M. S., Gordon R. Probing the quantum tunneling limit of plasmonic enhancement by third harmonic generation. *Nano letters* 2014, 14, 6651-6654.
- [96] Ciraci, C.; Hill, R. T.; Mock, J. J.; Urzhumov, Y.; Fernandez-Dominguez, A. I.; Maier, S. A.; Pendry, J. B.; Chilkoti, A.; Smith, D. R. Probing the Ultimate Limits of Plasmonic Enhancement. *Science* 2012, 337 (6098), 1072–1074.
- [97] Hajisalem, G.; Min, Q.; Gelfand, R.; Gordon, R. Effect of Surface Roughness on Self-Assembled Monolayer Plasmonic Ruler in Nonlocal Regime. *Optics Express* **2014**, 22 (8), 9604.
- [98] Seok, T. J.; Jamshidi, A.; Kim, M.; Dhuey, S.; Lakhani, A.; Choo, H.; Schuck, P. J.; Cabrini, S.; Schwartzberg, A. M.; Bokor, J.; Yablonovitch, E.; Wu, M. C. Radiation Engineering of Optical Antennas for Maximum Field Enhancement. *Nano Letters* 2011, 11 (7), 2606–2610.

-
- [99] Lassiter, J. B.; Chen, X.; Liu, X.; Ciracì, C.; Hoang, T. B.; Larouche, S.; Oh, S.-H.; Mikkelsen, M. H.; Smith, D. R. Third-Harmonic Generation Enhancement by Film-Coupled Plasmonic Stripe Resonators. *ACS Photonics* 2014, 1, 1212–1217.
- [100] Chen, X.; Ciracì, C.; Smith, D. R.; Oh, S.-H. Nanogap-Enhanced Infrared Spectroscopy with Template-Stripped Wafer-Scale Arrays of Buried Plasmonic Cavities. *Nano Letters* 2015, 15, 107–113.
- [101] Chen, X.; Park, H.-R.; Pelton, M.; Piao, X.; Lindquist, N. C.; Im, H.; Kim, Y. J.; Ahn, J. S.; Ahn, K. J.; Park, N.; Kim, D.-S.; Oh, S.-H. Atomic Layer Lithography of Wafer-Scale Nanogap Arrays for Extreme Confinement of Electromagnetic Waves. *Nature Communications* 2013, 4, 2361.
- [102] Park, H.-R.; Chen, X.; Nguyen, N.-C.; Peraire, J.; Oh, S.-H. Nanogap-Enhanced Terahertz Sensing of 1 nm Thick ($\lambda/10$) Dielectric Films. *ACS Photonics* 2015, 2, 417–424.
- [103] Lin, L.; Goh, X. M.; McGuinness, L. P.; Roberts, A. Plasmonic Lenses Formed by Two-Dimensional Nanometric Cross-Shaped Aperture Arrays for Fresnel-Region Focusing. *Nano Letters* 2010, 10 (5), 1936–1940.
- [104] Almeida, E.; Shalem, G.; Prior, Y. Subwavelength Nonlinear Phase Control and Anomalous Phase Matching in Plasmonic Metasurfaces. *Nature Communications* 2016, 7, 10367.